UNIVERSITY OF SOUTHAMPTON

FACULTY OF ENGINEERING, SCIENCE AND MATHEMATICS

School of Electronics and Computer Science

Effect of liquid nitrogen bubble dynamics on insulation performance for high temperature superconducting power apparatus

By

David John Swaffield

Thesis for the degree of Doctor of Philosophy

2005

UNIVERSITY OF SOUTHAMPTON

ABSTRACT

FACULTY OF ENGINEERING, SCIENCE AND MATHEMATICS
SCHOOL OF ELECTRONICS AND COMPUTER SCIENCE

Doctor of Philosophy

EFFECT OF LIQUID NITRGOEN BUBBLE DYNAMICS ON INSULATION PERFORMANCE FOR HIGH TEMPERATURE SUPERCONDUCTING POWER APPARATUS

by David John Swaffield

Progress toward operational designs of superconducting power apparatus has been aided by the advent of high temperature superconductors (HTS) and the availability of production quantities of HTS tapes. Prototype designs for HTS power apparatus, for example cables, terminations, current fault limiters, transformers and generators exist and many use liquid nitrogen as both coolant and dielectric. This study has sought to examine the effect of bubble dynamics caused by thermal and electrical induction on the performance of liquid nitrogen as an electrical insulation.

To achieve this aim a unique liquid nitrogen cryostat has been designed and manufactured with optical ports and a high voltage bushing. The cryostat is fitted with an integrated cryo-cooler which allows the temperature to be controlled across the liquid range of nitrogen and experimentation with applied pressures to 2 MPa. This has allowed an experimental investigation of bubble dynamics in liquid nitrogen in the presence of electric fields which is distinct in its examination of bubbles as they are thermally nucleated.

A comprehensive study of streamers and partial discharge behaviour within liquid nitrogen using point-plane electrode geometry for a range of applied 50 Hz voltages, temperatures and pressures has been completed. In order to do this a new technique to capture electrical partial discharge signals and images of density change streamers simultaneously has been developed and is described. φqn analysis has been employed to characterise the partial discharge and streamer activity in liquid nitrogen. Typical characteristics of density change streamers have been identified and theories of the physical mechanisms causing their formation are proposed.

Acknowledgements

I wish to express my thanks to all those who have supported me during the time I have been working on this thesis. I am particularly grateful to my supervisors Dr Paul Lewin, Dr George Chen and to our late colleague Professor Tony Davies whose professional advise and encouragement has been invaluable. I am confident I will continue to enjoy the benefits of the occasional "pep talk" from Dr Lewin in the future. Thank you to my colleagues of the Electrical Power Engineering research group whose comments and ideas have inspired and enlightened.

Special thanks to Mr Neil Palmer and our departed friend Mr Roland Caldecutt, two fine craftsmen whose knowledge and skill of manufacture have been pivotal to realising equipment I've gained so much enjoyment from designing and using. Thanks also to Mr Brian Rogers, Mr Mike Smith and Mr Steve Harrison for their continual assistance. I am thankful too for the friendship of my colleagues at the Tony Davies High Voltage Laboratory. I am very appreciative for the many discussions with Professor Carlo Beduz and Mr Mike Webb of the Institute of Cryogenics which aided me in the design of the experimental cryostat.

My gratitude is also extended to National Grid Transco, Pirelli Cables and EPSRC for the financial support of this project without which such a sophisticated experimental study would not have been possible. In particular thanks are due to Professor Steve Swingler.

A heartfelt thank you goes to my family and two close friends, Mr Adrian Robinson and Mr Graeme Williams for fun and friendship without which my spirits would have faded. In all things I give thanks to God and his son the Lord Jesus Christ who sustains me.

Contents

List of Figures

Chapter Two

Chapter Three

Chapter Four

Chapter Five

Chapter Six

Appendix A

List of Tables

Chapter Three

Chapter Four

Chapter Five

Nomenclature

Abbreviations

Symbol	**Meaning**
ac	Alternating current
AR	Anti-reflection
CHF	Critical heat flux
d.s.o.	Digital storage oscilloscope
dc	Direct current
DOF	Depth of field
EHD	Electrohydrodynamics
EPE	Electrical Power Engineering
FEA	Finite element analysis
FOV	Field of view
fps	Frames per second
HTS	High Temperature Superconducting
HV	High Voltage
IA	Inspection Authority
JF	Jointing factor
LAr	Liquid argon
LHe	Liquid helium
LN_2	Liquid nitrogen
LNe	Liquid neon
LTS	Low Temperature Superconducting
LXe	Liquid xenon
N_2	Dinitrogen
NDT	Non-destructive testing
OFHC	Oxygen Free High Conductivity
ONB	Onset of nucleate boiling
p.u.	Per unit
pd	Partial discharge
WD	Working distance
XLPE	Cross-linked polyethylene

Basic notation

Symbol	Meaning	Units
A	cross sectional area	m^2
a_0	Bohr radius (0.5292×10^{-10})	m
Ar	Archimedes number, Equation 4.11	
c	velocity of light in a vacuum (2.9979×10^8)	$m\ s^{-1}$
c_p	specific heat	$J\ kg^{-1}\ K^{-1}$
D	vector electric displacement	$C\ m^{-2}$
d	Spacing, distance	mm
D_B	bubble diameter	m
D_i	inner diameter	mm
D_o	outer diameter	mm
E	vector electric field strength	$V\ m^{-1}$
e	thickness	mm
E	electric stress	$kV\ mm^{-1}$
E	energy	eV or J
e_0	charge of an electron (1.602×10^{-19})	C
e_{cyl}	wall thickness	mm
E_F	Fermi energy	eV
E_{VAL}	valence energy band	eV
f	design stress	$N\ mm^{-2}$
f	frequency	Hz
F_d	dielectrophoretic force	N
F_V	electrohydrodynamic body force	$N\ m^{-3}$
g	acceleration due to gravity	$m\ s^{-2}$
h	Plank's constant (6.6262×10^{-34})	J s
h	heat transfer coefficient	$W\ m^{-2}K^{-1}$
H_c	critical magnetic field strength	$A\ m^{-1}$
I	Ionisation energy	eV
J	vector current density	$A\ m^{-2}$
Ja	Jakob number, Equation 4.9	
K	Boltzmann's constant (1.380×10^{-23})	$J\ K^{-1}$

k	thermal conductivity	$W\ m^{-1}K^{-1}$
k_L	liquid thermal conductivity	$W\ m^{-1}K^{-1}$
m	wetting coefficient	
n	number	
N_v	density number	
p	pressure	MPa
p_G	gas pressure of bubble	MPa
p_{Gmax}	maximum pressure of bubble gas	MPa
p_{sat}	saturation pressure	MPa
p_v	vapour pressure	MPa
p_∞	liquid pressure distant from bubble wall	MPa
P_+	polarisation energy	eV
Pr	Prandtl number, Equation 4.10	
$\dot{Q}$	rate of heat transfer	W
q	heat flux	$W\ m^{-2}$
q_f	free charge density	$C\ m^{-3}$
r	void radius, inner radius	mm
R	gas constant	$J\ kg^{-1}K^{-1}$
R	outer radius	mm
R_a	characteristic atomic or molecular radius	m
R_a	average roughness	µm
r_B	bubble radius	mm
r_I	radius of the interface	mm
r_L	radius of liquid surface	mm
$Rp_{0.2}$	0.2% yield strength	$N\ mm^{-2}$
S	stress	$N\ mm^{-2}$
t	time	s
T	temperature	K
T_{act}	activation temperature	K
T_G	temperature of bubble gas	K
T_{Gmax}	maximum temperature of bubble gas	K
T_I	interface temperature	K
T_L	liquid temperature	K

T_{sat}	saturation temperature	K
u	velocity	$m\ s^{-1}$
v	volume	m^3
V	voltage	V
V_0	apparent work function (of a liquid)	eV
V_e	Partial discharge extinction voltage	kV
V_i	Partial discharge inception voltage	kV
W	work function	eV
W_{off}	effective work function	eV
x	displacement	m
α	Townsend's first ionisation coefficient	
γ	ratio of specific heat of gas at a constant pressure to that at a constant volume	
ΔT_s	wall superheat	K
ε	permittivity ($\varepsilon = \varepsilon_0\ \varepsilon_r$).	$F\ m^{-1}$
ε_0	permittivity of free space (8.85×10^{-12})	$F\ m^{-1}$
ε_r	relative permittivity	
θ	static contact angle	degrees
λ	charge density	$C\ m^{-3}$
λ	wavelength	m
λ_{LV}	latent heat per unit mass: liquid to vapour	$kJ\ kg^{-1}$
μ	dynamic viscosity	$kg\ m^{-1}\ s^{-1}$
μ	coefficient of friction	
v	kinematic viscosity	$m^2\ s^{-1}$
ρ	density	$kg\ m^{-3}$
σ	electrical conductivity	$\Omega^{-1}\ m^{-1}$
σ	surface tension	$J\ mm^{-2}$
τ	charge relaxation time	s

Subscripts

Symbol	**Meaning**
d	dynamic
act	activation

B	bubble
BD	breakdown
G	gas
I	interface
L	liquid
max	maximum
min	minimum
S	solid
sat	saturation
V	vapour

Chapter One

Introduction

1.1 Superconductivity

In 1908 the Dutch physicist Heike Kamerlingh Onnes was the first to liquefy helium by utilising the Joule-Thompson effect to achieve temperatures of below 1 Kelvin. An achievement recognized in 1913 when he was awarded the Nobel Prize in Physics "for his investigations on the properties of matter at low temperatures which led, inter alia, to the production of liquid helium"[1]. In 1911 whilst studying the properties of materials at the temperatures achievable with liquefied helium, Onnes was the first to observe superconductivity when at 4.2 K he witnessed the resistance of solid mercury suddenly disappear.

Understanding of superconductors was further developed when in 1933 Meissner and Ochsenfeld discovered that superconductors reject an external magnetic field. This property of superconductors is known as the Meissner effect and is key property used in magnetic levitation devices such as the maglev train where the train is held 1-2 cm above the rail.

Current understanding of superconductivity is informed by two important theories. The Ginzburg-Landau theory (1950) which explains the macroscopic properties of

superconductors; it was later shown by Abrikosov to predict the division into what are known as Type I and Type II superconductors. Type I are superconductors that lose their superconducting behaviour when an external field of critical strength, H_C, is applied. Whereas, with the application of an external field of critical strength, H_{C1}, type II superconductors first go to an intermediate state where both superconducting and non-superconducting regions are present. All superconducting behaviour is then lost in a field at higher strength, H_{C2}. Abrikosov and Ginzburg were awarded the Nobel Prize in Physics 2003 for their work (Landau died in 1968). The second important theory is the BCS theory (1957) named after its formulators Bardeen, Cooper and Scheiffer who won the 1972 Nobel Prize for proposing "Cooper Pairs" to describe how superconductivity operates on the microscopic scale.

In the decades following Onnes discovery that mercury, lead and many other elemental metals displayed superconductivity other metallic alloys have been developed that have higher critical temperatures up to 25 K, where critical temperature is the temperature below which a material becomes superconducting. These metals require the use of liquid helium as a coolant. A breakthrough came with the development of ceramic superconductors. In 1986 IBM researchers Muller and Bednorz made ceramic compound of lanthanum, barium, copper and oxygen that superconducted at 35 K. The next year, groups working at the University of Houston and the University of Alabama headed by Chu substituted yttrium for lanthanum and made a compound (YBCO) superconduct at 92 K. At atmospheric pressure liquid nitrogen has a boiling point of 77.3 K and a melting point of 63.1 K. YBCO is within the range where liquid nitrogen (LN_2) can be used as coolant, hence the term high temperature superconductor (HTS) being applied to materials displaying a critical temperature above the normal boiling point of LN_2. Since the first high temperature superconductor a hundred or so have been formulated with a peak critical temperature in 1993 of 133 K by Schilling and colleagues who developed a mercury, barium, calcium, copper oxide (HgBaCaCuO) ceramic.

1.2 Technological exploitation

Since the discovery of superconductivity its technological exploitation has been of great interest. The discovery of high temperature superconductivity has made its use in applications more economically viable. Superconductivity has found application

in many areas including; MRI (Magnetic Resonance Imaging), magnetic levitation, magnets for particle accelerators, sensitive magnetic measurement using SQUIDs (Superconducting Quantum Interference Devices), electric motors and power generation and transmission apparatus.

1.2.1 Potential benefits and power applications

Implementation of superconductors becomes simpler at the comparatively high temperatures required for HTS ceramics and allows the use of cheaper liquid nitrogen as a coolant. HTS ceramics are inherently more temperature stable than low temperature superconductor (LTS) material; a higher specific heat makes it less sensitive to transient temperature fluctuation [2]. Superconducting power apparatus offer advantages over conventional equipment, these are; reduced ohmic losses, increased power density and lower operating voltages.

The use of high temperature superconductors for a range of applications in the generation and transmission of electrical power has been proposed. Work to exploit the potential benefits of HTS has already been reported with prototype or commercial design of generators [3], transformers [2, 4], current limiters [5, 6], transmission cables, joints and terminations [7-10].

1.2.2 Design considerations

In order for superconductive power apparatus to compete against conventional conductor technologies there are issues to be addressed that include: Engineering constraint, economics, environmental impact and reliability. Superconducting cables offer higher power density, this is attractive especially where there are size constraints placed on the design of a cable system. For example, where extensive power cable ducting is already installed and the retrofit of superconducting cables would offer an increase in the available power rating. Where there is no overriding engineering constraint, the economic advantage of superconducting transmission cables will have to be satisfied. The economics of superconducting cable system installation has been studied and most discussion centres on the savings from reduced ohmic losses outweighing the costs of the cryogenic installation and continual refrigeration of the cable. Conclusions present minimum required current ratings and lengths for the superconducting cables to compete with conventional

designs [11]. In relation to the environment, LN_2 cooled cable is considered to have less environmental impact than cross-linked polyethylene (XLPE) or oil-filled paper cables. This is because nitrogen (N_2) gas accounts for 78% of the atmosphere and so any loss from an LN_2 leak will return through evaporation to the atmosphere as gas. However, both cable-oil and XLPE are not readily broken down in the environment.

If such devices are to be exploited commercially, a key factor will be confidence in the reliability of designs. This is an essential requirement for utility operators. Many superconductor equipment designs utilise liquid nitrogen both as the conductor coolant and dielectric. Characterisation of the dielectric properties of liquid nitrogen is therefore essential to the design process if reliable operation of power equipment in a power network is to be achieved. The research presented in this thesis is an extension of a completed design study of a cable termination for cryogenic/superconducting to ambient/conventional conductor.

1.2.3 Study motivation

This project has sought to address issues related to the development of high voltage cables and terminations. Terminations in particular exhibit many of the complexities facing engineers involved in a design process to implement HTS technology.

HTS cable terminations have to transmit high currents across an ambient to cryogenic temperature transition. The design of such equipment must do this with the requirements of good thermal efficiency in addition to high current flow and controlled electric stress. For a termination, the conflicting requirements of high electrical conduction and low thermal conductivity mean that at maximum continuous rating and under fault conditions there will be significant thermal input into the low temperature region. In a HTS termination two breakdown scenarios can be anticipated, voltage breakdown across an insulating surface (surface flashover) and the breakdown in the bulk of the dielectric fluid (liquid nitrogen away from solid surfaces). In both cases many parameters influence the process, one of which is the presence of bubbles. Therefore pre-breakdown characterisation of liquid nitrogen and the influence of N_2 bubbles is a growing area of interest.

1.3 Experimental design

This study has centred on the influence of nitrogen vapour within the bulk liquid dielectric with applied electric fields. The presence of N_2 bubbles in the liquid dielectric causes local electric stress enhancement and a region of dielectrically weaker gas. Vapour may be trapped in microcavities on surfaces during filling, be generated by heating or initiate from discharges with applied high electric stress. As prototype devices for many power transmission elements are currently being designed, this study has been timely in addressing the complex area of pre-breakdown phenomena in liquid nitrogen.

To study the influence of vapour in liquid nitrogen with applied electric fields a unique liquid nitrogen cryostat has been designed and manufactured (Chapter 3). The cryostat is of tubular design with stainless steel inner and outer vessels. The cryostat allows liquid nitrogen to be held at temperatures down to 63 K to less than a degree by means of a single-stage helium expander cryo-cooler integrated into the cryostat vacuum inter-space, between the inner and outer jackets. For optical measurements the cryostat has four optical ports, the outer windows are BK7 optical grade glass the inner vessel windows are sapphire. Sapphire was chosen for its excellent mechanical properties at cryogenic temperatures. The inner vessel is pressure rated to 2 MPa. The cryostat is fitted with a high voltage bushing rated up to 80 kV ac and partial discharge (pd) free up to 50 kV ac.

Around the central apparatus of the cryostat a stroboscopic backlit imaging system has been developed to allow high temporal and spatial resolution measurements of pre-breakdown phenomena. This system consists of a high speed digital camera with microscope lens and a 20 W copper vapour laser allowing frame rates up to fifty thousand frames per second. The copper-vapour laser provides very short light pulses of 30ns and with a repetition rate and power required to light subjects imaged at frame rates up to fifty thousand frames per second. The short pulses effectively determine the shutter speed of the system and virtually eliminate the motion blur that would otherwise result from the movement of density change streamers and bubble surface oscillations during their surface detachment or "pinch-off". A technique for

synchronised recording of pre-breakdown density change streamer images and electrical discharge data has been developed.

1.4 Experimental study

This thesis examines several pre-breakdown phenomena. Firstly thermally induced bubble nucleation is examined. Boiling is known to be a complex phenomenon influenced by many parameters including; surface finish, material, heat input, liquid temperature, hydrostatic pressure, applied voltage and electrode geometry. The approach presented has been used to examine the bubble life cycle from inception, through growth and to detachment from the surface (Chapter 4). For this samples were developed with heat sources embedded into plane electrodes and artificial cavities manufactured into the top surface. In theory this allows the generation of thermal bubble nucleation at a single point in a uniform electric field. Initial results showed dependence between characteristic parameters of departure frequency, departure volume and aspect ratio. However, experiments revealed that the re-entrant cavity permitted nucleation from multiple sites within it, which then coalesce to grow a single bubble. Thus a proportion of the bubbles observed nucleated and detached below the visible level of the entrance of the cavity. Additional experiments sought to constrain the nucleation to a smaller re-entrant cavity mouth. These studies revealed that the process of bubble nucleation and boiling is difficult to model. Little fundamental study of bubble dynamics had been previously performed in liquid nitrogen and the problem is further complicated by the presence of an applied electric field.

A new technique for time-correlated measurement of apparent charge and images of partial discharge activity has been developed (Chapter 5). A point-plane arrangement with a solid insulation barrier to prevent total breakdown has been employed to simulate the condition of a strongly divergent electric field. Such an arrangement has been used to electrically initiate partial discharges and density change streamers. The electrical discharges and density change streamer growth has been studied and φ q n plots used to characterise partial discharge (pd) activity across the liquid temperature range for nitrogen at atmospheric pressure, hydrostatic pressure up to 0.2 MPa and a range of applied voltages up to 28.5 kV ac (Chapter 6). Optical recordings characterise the difference between positive and negative streamer

shapes and density change streamer behaviour under alternating current (ac) conditions. Discussion of the results of these experiments considers theories for the physical processes governing density change streamer initiation and propagation into the bulk liquid.

This thesis concludes with a review of the progress made into the several complex phenomena studied, namely; boiling, dielectrophoresis and pre-breakdown streamer propagation. Avenues for further study are then outlined and discussed (Chapter 7).

Chapter Two

Literature review

2.1 Introduction

The resurgence of interest in superconducting power apparatus with the advent of HTS has led to a renewed interest in cryogenic electrical engineering. Liquid nitrogen is readily available from the atmosphere and is therefore cheap to produce. LN_2 has a liquid range of 66.05 - 77.36 K, at atmospheric pressure, this makes it ideally suited for HTS equipment. Cryogenic cooling of the superconducting material is necessary and both concept designs and prototypes are using liquid nitrogen as the combined coolant and dielectric liquid. Understanding the dielectric properties of liquid nitrogen is therefore essential to an informed design process.

The breakdown strength of liquid nitrogen under some conditions is measured to be as good as mineral oils at room temperature; however the liquid range of nitrogen is much smaller, only 14.31 K at atmospheric pressure. Breakdown strength is observed to be greatly influenced by the formation of bubbles. The increased possibility for bubble production and the effect this has on liquid nitrogen dielectric performance in cryogen dielectrics is of significant interest to electrical engineering in the design of cryogenic power apparatus.

The behaviour of bubbles has been studied with interest in many fields including; heat transfer, cryogenics, cavitation, acoustics and dielectrics. A significant body of work exists and some of the theory relevant to cryogenic dielectrics, bubble nucleation and dynamics is reviewed here. This is followed by a discussion of electrical properties and breakdown characterisation of liquid nitrogen and the influence of bubbles on electrical performance.

2.2 Pool boiling

Boiling takes place at the solid-liquid boundary and involves a complex set of phenomena. A liquid boils when the temperature of the adjacent surface exceeds the saturation temperature, T_{sat}, of the liquid.

There are two main subdivisions within the study of boiling. Free boiling of a liquid where there is no forced flow or agitation of the liquid. This is known as pool boiling as the concept is of a quiescent 'pool' of liquid. The alternative situation is of a liquid forced over a heated surface; this condition is termed forced convection or flow boiling. Both situations can be envisaged in future superconducting power equipment. However this project only concerns itself with thermally induced bubbles in pool boiling and the influence that an electric field has upon the bubble dynamics and dielectric properties. This allows much simpler experimentation and analysis and provides a basis for further study as required.

The rate of heat loss from a thermally conducting surface is limited if it is only by conduction. Neither is convection sufficient to achieve high levels of heat flux. The onset of vapour bubble production however has a dramatic effect and high levels of heat flux become possible. Rapid growth and detachment of bubbles causes a vigorous stirring adjacent to the heated surface and is also important for improving heat transfer rates by the transfer of latent heat.

2.2.1 Boiling curve

Boiling characteristics for a given liquid are normally presented as a logarithmic plot of heat flux (q), against the wall superheat (ΔT_s). Boiling curves can be obtained experimentally in two ways, with either a temperature controlled or heat flux-controlled experiment. An example of a temperature controlled experiment curve for

a smooth surface is shown in Figure 2.1. With reference to Figure 2.1, the heat-flux controlled curve is shown by the irreversible dashed lines d-d' and e-e'. The boiling curve allows the analysis of boiling to be formalised into distinct regimes of pool boiling. The gradient of the curve represents, h ($W\ m^{-2}\ K^{-1}$), the heat transfer coefficient. Where,

$$h = \frac{q}{\Delta T_s} \tag{2.1}$$

2.2.2 Natural convection

Boiling begins when the liquid temperature at the solid wall exceeds that of the bulk liquid. When the excess temperature of the liquid at the wall is small, before the onset of bubble nucleation, the liquid is superheated and rises, the fluid motion governed by the principles of free or 'natural' convection. In free convection fluid motion is induced by buoyancy forces arising from the density variations. These are in turn generated by the temperature variations within the fluid and adjacent surfaces.

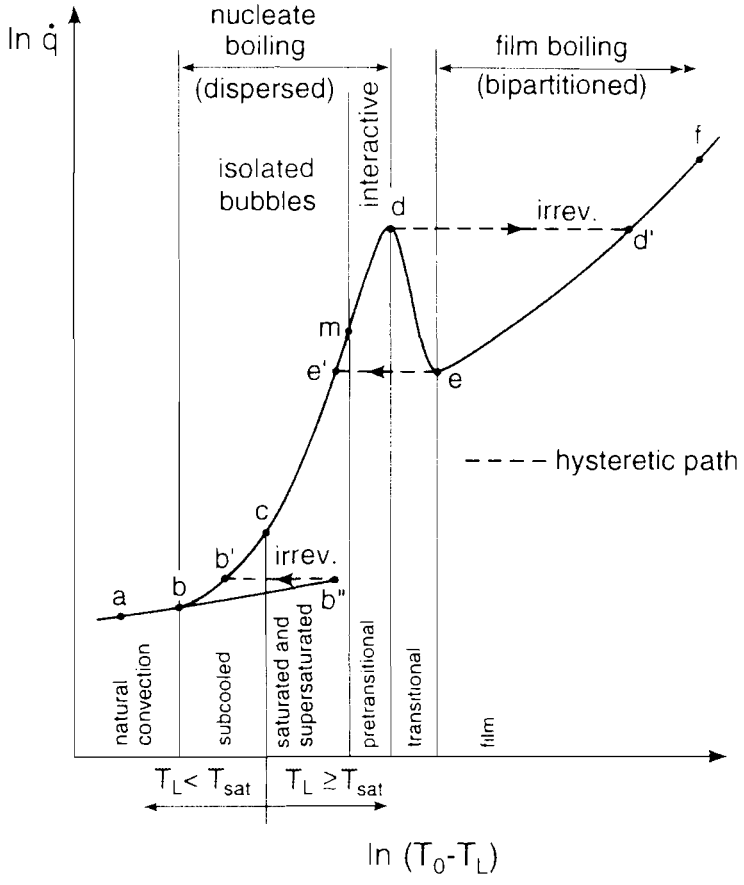

Figure 2.1, Boiling curve [12] The pool boiling curve, solid line: temperature controlled, dashed line: heat flux controlled.

2.2.3 Nucleate boiling

Bubbles can be generated thermally and in order for a bulk liquid to change phase by boiling, the liquid at the interface has to be superheated to beyond the critical temperature. Before homogeneous boiling is achieved heterogeneous boiling will occur with individual bubbles forming at preferential nucleation sites. This regime is termed nucleate boiling.

2.2.4 Saturated, supersaturated and pre-transitional boiling

If the temperature of the liquid is raised further boiling moves into the saturated region. Where the liquid temperature, T_L, is greater than the saturation temperature, T_{sat}, this region of boiling is characterised by repetitive nucleation and bubbles breaking the surface before they are condensed. In the saturated boiling mode the bubbles form columns which do not interact with other sites.

At any single site nucleation occurs with a rapid growth of the bubble. This growth rate is reduced as evaporative cooling of the substrate beneath the superheated layer occurs. The reduced growth rate results in the temperature of the substrate rising. When buoyancy forces overcome the surface tension retaining forces, the bubble pinches-off and rises. The surface re-floods and a slow rise in substrate temperature occurs. The process at this point repeats and after a delay period there is nucleation of a new bubble. The result is plumes of bubbles from nucleation sites.

Convection boiling is not capable of producing very high levels of heat flux but as nucleate boiling and then saturated boiling take over the production of bubbles causes vigorous stirring and latent heat transfer continues to increase the heat flux attainable. As the temperature of the liquid continues to rise the frequency of bubbles increases as does the number of active nucleation sites. The spacing between active nucleation sites reduces until the bubbles and plumes from different sites begin to interact and coalesce.

Bubble plumes enhance natural convection by producing updrafts in the bubble column and return paths between them. However a new model is needed when

bubbles begin to interact even before lift-off. Increasing the temperature further causes larger coalesced bubbles to repeat more frequently and heat flux rises further. The larger bubbles now produced by interaction eventually become separated from the surface by a macrolayer of superheated liquid. Heat transfer continues by two methods; firstly evaporation at the large vapour boundary into the bubbles, and secondly high frequency bubble jets punch through the layer into the large vapour bubbles.

Ebullition continues to be important even in this region of the boiling curve, its effect reducing as the macrolayer thins. The macrolayer thins as it evaporates into the vapour bubble, and the bubble jets have less effect. The macrolayer then thickens again after bubble lift-off and the effect again increases. The macrolayer will vary in thickness across the surface and will be continually changing over time.

2.2.5 Film boiling

The film boiling regime is characterised by the heated surface being covered with a continuous film of vapour. In this regime heat must be transferred by conduction, convection or radiation through the vapour film to cause evaporation at the liquid vapour interface. Film boiling displays hysteresis and once established it remains stable even at heat fluxes below the critical level. Again with reference to Figure 2.1, this allows the boiling curve to trace the path to e, the minimum heat flux or Leidenfrost temperature, at this point nucleate boiling is resumed.

2.2.6 Transitional boiling

The transitional boiling regime is only seen when the temperature of the substrate is used to control the boiling behaviour. With reference to Figure 2.1, if heat flux is used to control the boiling then when point critical heat flux (point d) is exceeded the boiling jumps irreversibly into the film boiling regime (path d-d'). The critical heat flux is also known as burnout, as the large increase of temperature to point d' may exceed the melting point of the substrate material or heater. The transitional regime is characterised by the formation of a large number of dry areas on the substrate surface. These dry patches are then re-flooded as the vapour moves away from the surface and vigorous bubble formation occurs. The increased area covered by dry

patches reduces the heat transfer and hence the shape of the boiling curve, where heat flux decreases as the superheat increases.

2.2.7 Homogeneous bubble nucleation

For completeness, it is worth mentioning homogeneous nucleation. When the saturated liquid temperature is greater than the critical point the liquid and vapour phases become indistinct. At temperatures slightly below this level a small increase in local temperature will result in spontaneous generation of vapour embryos within the bulk of the liquid. This will occur homogeneously if a liquid is depressurised below the activation pressure.

2.3 Boiling in liquid nitrogen

A significant volume of research has been undertaken into the boiling phenomena of liquid nitrogen. The assumption that theory applicable to room temperature liquids is applicable to cryogens has been disputed by some authors [13-15], who believe that cryogens should be treated separately; as a group of liquids having distinct thermal properties. There are boiling data for a wide range of geometries including; plates [16, 17], wire [18, 19], inside tubes (both vertical and horizontal and in bundles) [20] and outside cylinders (both vertical and horizontal) [21, 22]. A range of surface materials have also been investigated, including metals; stainless steel, copper, nickel and ceramics. There is also a body of work concentrated on coatings and coated surfaces for improving the heat flux [23, 24].

2.3.1 Pool boiling

It has been found that nucleate boiling data can vary widely depending on surface orientation, material, surface roughness coating and history. For this reason any boiling curve is specific to these parameters. A review of boiling curve data is provided by Brentari and Smith [25].

A study of boiling liquid nitrogen on horizontal plate surfaces [16] observed hysteresis of incipient boiling levels. It is reported that artificial cavities could significantly affect heat transfer by natural convection. Surface roughness, surface material and artificial cavities were all found to affect nucleate boiling coefficients on a mirror finished surface. Nucleate boiling heat flux was found to be dependant

on the number of nucleate boiling sites. Interpretation of these results requires consideration of the nucleation and conditions for growth of bubbles within a liquid by heat transfer.

2.4 Thermally induced bubble nucleation

This section reviews the theory related to bubbles and conditions for nucleation and growth on surfaces.

2.4.1 Laplace pressure

In equilibrium the internal pressure of a spherical bubble within the bulk of a liquid phase is equal to the external pressure and the pressure due to surface tension. Consider a bubble of radius, r_B, as shown in Figure 2.2.

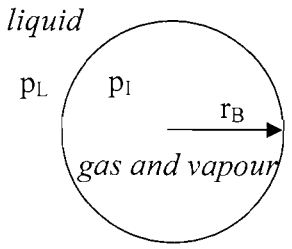

Figure 2.2, The pressure of a static gas/vapour bubble in a liquid.

The internal pressure of the bubble, p_I, is made up of the contribution of the pressure of gas, p_G, and of vapour, p_V,. Thus;

$$p_I = p_G + p_V \tag{2.2}$$

At rest the internal pressure is greater than the pressure of the liquid immediately outside, this is due to the surface tension. Taking p_L as the liquid pressure at the bubble wall acting radially inwards, and p_σ as the surface tension pressure acting radially inwards then in order to balance pressures;

$$p_I = p_L + p_\sigma \tag{2.3}$$

The excess pressure internal to the bubble acting radially outwards to balance p_σ the surface tension pressure is also known as the Laplace pressure. The Laplace pressure is given by;

$$p_\sigma = \frac{2\sigma}{r_B} \tag{2.4}$$

This may be intuitively understood by considering a bubble cut vertically in half. The force, F, pushing the two halves apart is the pressure multiplied by the area as seen by pressure acting normal to the cut, a circle.

$$F = p_\sigma \pi r_B^2 \tag{2.5}$$

This equals the force, F, holding the bubble together, where the surface tension force per unit length, σ, acts along a hoop with an infinitely thin line, the circumference of a circle.

$$F = \sigma 2\pi r_B \tag{2.6}$$

Equating and rearranging (2.5) and (2.6) leads to the expression for Laplace pressure, (2.4).

2.4.2 Spherical bubble shape

It is commonly observed that bubbles tend to be spherical or spheroid in shape. An example of departure from a true sphere is used in section 2.4.7 when considering the growth of bubbles in a thermal gradient. The tendency for bubbles to be spherical is due to surface tension. It follows, considering Figure 2.3, that if the bubble has a distorted shape with radii r_1 and r_2 at different locations on the bubble surface, then the force at the smaller radius r_2 will be greater than that at r_1 and pull the shape towards a sphere.

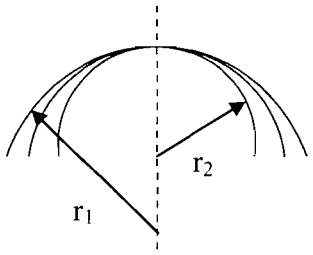

Figure 2.3, Schematic representation of the radii of distorted bubble surfaces.

The relationship between pressure and surface tension is defined as;

$$p_\sigma = \sigma\left(\frac{1}{r_1} + \frac{1}{r_2}\right) \tag{2.7}$$

From (2.7) the contribution to overall pressure is greater for the smaller radius, r_2, consequently if a bubble has a non-uniform curvature (i.e. it is non-spherical) then there is a local surface tension, which will tend to return the surface to a spherical shape. When a bubble is returned towards a sphere by surface tensions there will be overshoot and oscillations due to the liquid's inertia. The extent of this will be a function of the fluid properties and the size of the bubble [26].

2.4.3 Thermally induced bubble nucleation

Boiling will not spontaneously start in the bulk of a stagnant liquid. This is demonstrated by considering the mechanical equilibrium of a small vapour bubble, radius r_b. The condition for equilibrium is;

$$p_V = p_L + \left(\frac{2\sigma_{LV}}{r_B}\right) \tag{2.8}$$

The condition for the bubble to grow is therefore;

$$p_V > p_L + \left(\frac{2\sigma_{LV}}{r_B}\right) \tag{2.9}$$

Since the definition for saturation temperature is that p_v equals p_L, (2.8) and (2.9) can not be satisfied and the theorised embryonic bubble would collapse. So for the liquid to boil there must be nucleation sites of pre-existing vapour or gas regions which in order to nucleate have a radius r_B to satisfy (2.9). In order for nucleation to occur at these nucleation sites it is necessary to increase p_v above p_L (boiling) or decrease p_L below p_v (cavitation). Pre-existent regions of vapour can take the form of free gas bubbles suspended in the liquid, important in flowing systems. However, the concern here is only with "pool" boiling where the concept is of a quiescent pool of boiling liquid.

The activation pressure required for the embryonic gas-vapour bubble to grow can be estimated from the conditions for spherical bubbles at equilibrium within bulk liquid, (2.8). The Clapeyron Equation relates the liquid superheat to the pressure for a phase change [27];

$$\frac{p_V - p_L}{(T_w - T_{sat})} = \frac{\lambda_{LV}}{T_{sat}(v_V - v_L)} \tag{2.10}$$

Where λ_{LV} is latent heat per unit mass, T_W is wall temperature (K), v_V and v_L are vapour and liquid volume (m^2) respectively. In the case of a phase change from liquid to vapour and v_V is much larger than v_L and so v_L is neglected. Furthermore v_v is replaced by the ideal gas law. With these assumptions combining and rearranging (2.8), (2.10) allows an estimate of the activation temperature;

$$T_{act} - T_{sat} = \frac{2RT_{sat}^2}{\lambda_{LV} p_{sat}} \left(\frac{\sigma_{LV}}{r_B} \right) \tag{2.11}$$

Where p_{sat} is saturation pressure and R is the ideal gas constant. Note that the ideal gas law is more accurate at low pressures and so this approximation will be better at the triple point than the critical point. Equations 2.10 and 2.11 define the bubble activation isobar and isotherm, respectively. From these equations it can be seen that at a given pressure p_{sat}, activation superheat is proportional to σ_{LV}/r_B. This is found to be a monotonically decreasing function of σ_{LV} [12]. The result is that higher

wetting liquids (i.e. with lower σ_{LV}) require higher superheats than poorly wetting liquids. Superheat required for nucleation is proportional to microcavity size, therefore greater surface roughness will reduce superheat required to activate nucleate boiling in a liquid. T_{act} is dependent on cavity size and since there is a random distribution of cavity sizes on a surface, for any temperature above T_{act}, for the largest cavity (first activated), there will be more than one site on the surface becoming active.

2.4.4 Bubble initiation, nucleation sites and surface wetting

There are many microcavities even on smooth surfaces the diameters governed by surface finish and can be measured as average roughness (R_a), it has been estimated that microcavities of 0.1-10 μm in diameter are randomly distributed in densities as high as 10^8 cm^{-2} [12]. These sites will trap gas before boiling and especially during flooding of the surface.

As a substrate is heated, vapour is released from the solution. The pockets of vapour swell and can be seen protruding above the surface before the onset of boiling. It has been noted experimentally that the chemical composition of the liquid, substrate and the surface condition of the substrate will all influence the threshold temperature required to induce the onset of boiling. This can be understood by examining conditions for gas regions to be trapped within the nucleation microcavities.

Surface wetting can be defined by considering a liquid drop on a horizontal substrate in static equilibrium (Figure 2.4).

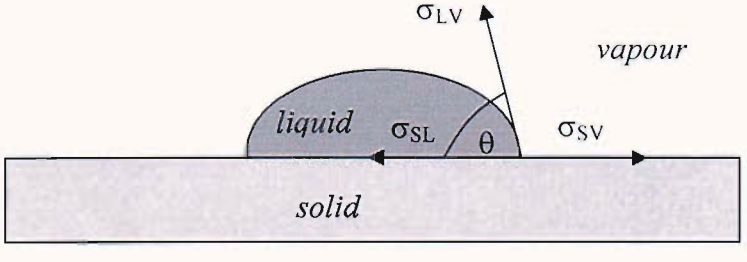

Figure 2.4, Surface tensions acting at the junction of vapour, liquid drop and solid substrate.

For static equilibrium all forces must sum to zero. Therefore resolving horizontal forces;

$$\sigma_{LV}\cos\theta + \sigma_{SL} - \sigma_{SV} = 0 \tag{2.12}$$

where θ is the static contact angle (degrees) and σ_{SL} is termed the wetting or adhesion tension (J mm^{-2}). From (2.12) the wetting coefficient, m, can be defined as;

$$m = \cos\theta = \frac{\sigma_{SV} - \sigma_{SL}}{\sigma_{LV}} \tag{2.13}$$

Figure 2.5 and Figure 2.6 show gas trapped in conical and re-entrant cavities on a substrate surface, where the scale is greatly exaggerated for clarity. For an easily wetting surface θ is small and σ_{LV} is also small. For a poorly wetting surface θ and σ_{LV} are not small. It is worth noting that the easily wetting surface will result in a smaller trapped gas bubble than the poorly wetting surface. The easily wetted surface results in gas pockets with a concave liquid surface, as viewed from the gas pocket. The poorly wetting surface results in a convex liquid surface, as seen in Figures 2.5 and 2.6. It can be shown using (2.8) that the concave surface of the easily wetting surface results in a higher pressure of trapped gas than the poorly wetting surface.

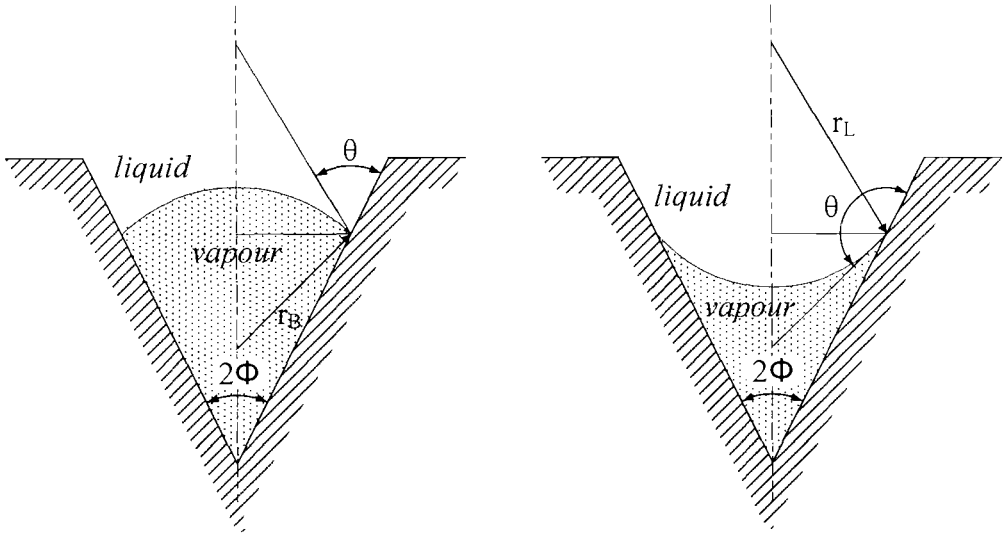

a) b)

Figure 2.5, Vapour cavity trapped in a conical cavity;
easily wetted, b) poorly wetted

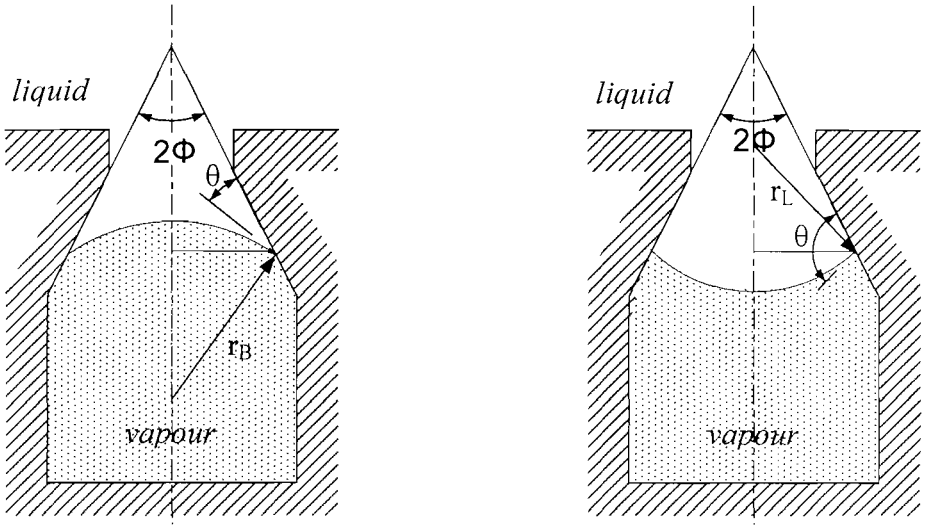

Figure 2.6, Vapour cavity trapped in a re-entrant cavity;
a) easily wetted, b) poorly wetted

For liquid nitrogen it has been estimated that the dynamic receding contact angle is 20° [28], but it has been suggested that as a group cryogenic liquids have a static contact angle less than 10° [29, 30], these values vary with the material and surface condition. These are comparatively small contact angles and it can be anticipated therefore that liquid nitrogen will easily wet surfaces and cavities.

2.4.5 Henry's law

Henry's law implies that for equilibrium conditions, the concentration of gas in solution will be proportional to the partial pressure of the adjacent gas phase at a given temperature.

$$p = kC \tag{2.14}$$

where C is concentration and k is the Henry's law constant (mol $kg^{-1}MPa^{-1}$) which is specific to the liquid and vapour. The excess Laplace pressure of the gas in the bubble causes the concentration of the gas in the liquid at the bubble wall to exceed that far from the bubble. As a result this concentration gradient will tend to dissolve

the bubble. The bubble size thus reduces and as r_B reduces, the Laplace pressure becomes greater increasing the drive for the bubble to dissolve.

Bubbles will tend to become smaller for liquids with; smaller surface tension, increasing gas density, and decreasing liquid viscosity. This also results therefore in reduced bubble size for elevated pressures and temperatures, providing that evaporation is minimal [31].

2.4.6 Bubble growth

Once the activation superheat is achieved bubble growth will occur. Figure 2.7 shows the vapour-liquid interface contact line as it travels up the cavity. Evaporation at the bubble surface maintains the concave interface.

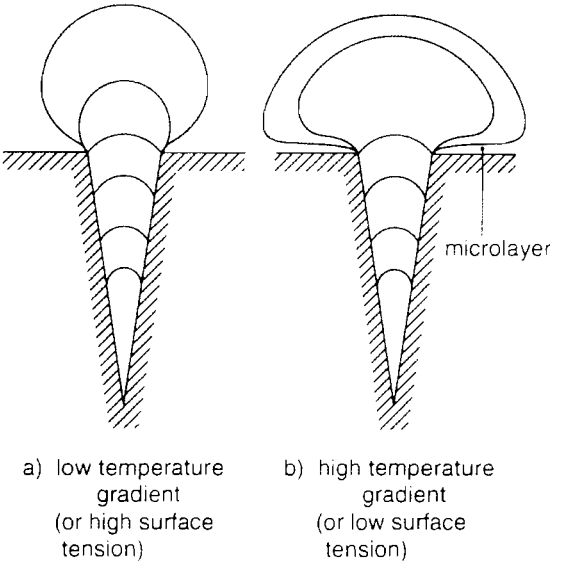

Figure 2.7, Diagrammatic representation of vapour bubble growth within and beyond a microcavity [12].

Figure 2.7 shows the case for low heat flux and a small temperature gradient normal to the substrate surface, with relatively slow growth rate. The bubble tends to grow spherically, surface tension and buoyancy striking a quasi-stable balance. For the case with high heat flux the high substrate temperature and liquid temperature gradient reduce the period of growth and viscous and inertial effects become more prominent. As depicted in Figure 2.7 b) the bubble base spreads close to the substrate surface creating a fluid microlayer the overall shape of the bubble forming

more like a hemisphere. For the case with low heat flux the growth rate is low and decreases as the bubble grows, for the high heat flux the growth rate is higher and remains constant.

2.4.7 Bubble detachment and subcooled boiling

If the temperature of the surface rises above T_{act} the liquid moves into the region of nucleate boiling where isolated bubbles are formed on the surface of the solid surface. It is has been suggested that the growth of the protruding or detached bubble can be described by the interface equation [12];

$$\rho_v \lambda_{LV} \frac{dr_I}{dt} = k_L \left(\frac{\partial T}{\partial r} \right)_I = h(T_L - T_I) \qquad (2.15)$$

Note it is assumed that the vapour temperature is uniform since it is created at T_I.

Equation 2.15 may also be used to describe how a bubble interface will shrink if the bulk liquid is below the saturation temperature. Following detachment it describes how the vapour bubbles rise and condense in the subcooled liquid. This mode is called subcooled boiling where the interface temperature, T_I, is greater than T_{sat} which is greater than T_L. This condensation can occur before a bubble is detached from the surface if the bubble is large enough to protrude beyond the superheated layer adjacent to the substrate. During this condensation latent heat is given up to the liquid raising its temperature towards T_{sat}.

The bubble will detach when the buoyancy forces exceed the restraining force of the surface tension. During this pinch-off process not all the vapour is taken by the bubble, some is left as a pocket in the nucleation site to begin the process again. The creation and detachment of a bubble causes a local cooling at the nucleation site sufficient to delay the creation of the next bubble; this is more pronounced for highly wetting liquids [12].

2.5 Free bubble modelling and Rayleigh collapse

If a bubble is considered detached from a surface it may be termed a free bubble. In the early 1900s Lord Rayleigh pioneered work on cavitation and bubble collapse of

free bubbles providing a foundation for work on bubble cavitation. Although theoretical treatment of free bubbles is highly idealised it leads to some instructive results.

2.5.1 Collapse of an empty cavity

As a first approximation, consider the case for a liquid with a spherical void radius r_m. The assumptions are that the void will always be a sphere and that the liquid is incompressible. By equating the hydrostatic work done by the pressure of the liquid (p_∞) to the kinetic energy of the liquid the following relationship is derived;

$$\dot{r}^2 = \frac{2p_\infty}{3\rho}\left(\frac{r_m^3}{r^3} - 1\right) \tag{2.16}$$

The negative root of this expression is taken to find the wall velocity since the bubble collapses inwards. Thus time for collapse, t, can be found;

$$t = \int_{r_m}^{r=0} \frac{dr}{\dot{r}} \approx 0.915 r_m \sqrt{\frac{\rho}{p_\infty}} \tag{2.17}$$

However the assumption of incompressibility is invalid as the wall velocity approaches the speed of sound, which always occurs in this model, from (2.16). Therefore it is necessary to consider the case for gas within the cavity [32].

2.5.1.1 Collapse of gas cavity

The gas causes the bubble to oscillate between r_{max} and r_{min} and with no damping r_m equals r_{max}. The assumption is made that the process is adiabatic, i.e. that no heat flows into or out from the gas. The following relationships can be derived by consideration of the energy of compressed gas and potential and kinetic energy of the liquid;

$$p_G\left(\frac{r_m}{r_{min}}\right)^{3(\gamma-1)} = p_\infty(\gamma - 1) \tag{2.18}$$

where p_G is the pressure of the bubble gas, and γ is the ratio of specific heat of gas at a constant pressure to that at a constant volume. This yields the maximum gas pressure;

$$p_{G\max} = p_G\left(\frac{r_m}{r_{min}}\right)^{3\gamma} \approx p_G\left(\frac{p_\infty(\gamma-1)}{p_G}\right)^{\frac{\gamma}{\gamma-1}} \tag{2.19}$$

where p_{Gmax} is the maximum pressure of the bubble gas. The corresponding temperature expressions are;

$$\frac{T_{G\max}}{T_G} = \left(\frac{r_m}{r_{min}}\right)^{3(\gamma-1)} \tag{2.20}$$

where T_m is the temperature of the bubble gas and T_{max} is the maximum temperature of the bubble gas, Equation 2.20 then leads to;

$$T_{G\max} \approx \left(\frac{p_\infty(\gamma-1)}{p_G}\right)T_m \tag{2.21}$$

2.5.1.2 Collapse of a vapour cavity

To complete the picture of Rayleigh-like collapse the case for vapour cavity is considered. In some models, the assumption is that the vapour in a cavity can condense quickly enough to keep the vapour pressure and temperature constant throughout a collapse [33]. The Rayleigh model has also been extended to account for latent heat [34]. Using the example of water it can be demonstrated that at different liquid temperatures different factors dominate. For example, at 15 °C there is no vapour decrease, but at 100 °C there is a 50% pressure decrease. Thus thermal rather than inertial factors dominate. The properties of the liquid and its state, temperature and pressure, affect the behaviour of the bubbles within it [34].

2.5.2 Free bubble modelling in liquid nitrogen

Modelling of free bubbles has been applied to liquid nitrogen. A favourite approach to achieve the idealised spherical free-bubble is the laser-induced bubble. In this

method a laser is focused to a very small spot within liquid nitrogen and the local heat produces a near-spherical bubble. This method was first performed by Golubnitchii et al in 1979, however it is only relatively recently that images of the bubble motion have been captured to study bubble dynamics [35].

Sato, Sun, Odagawa, Maeno and Honma [36] succeeded in capturing images at 50000 frames a second with a high speed camera (Imacon 790) and simultaneously measuring the pressure waves in the liquid. Both the Rayleigh-Plesset (incompressible liquid) and the Keller-Herring (compressible liquid) models have been applied. It was shown that the compressible solution provides a more damped bubble oscillation. The models fitted well for the first oscillation with correct choice of evaporation/condensation coefficient (0 to 1, adiabatic to isothermal respectively), this demonstrates the importance of thermal effects with phase change, specifically with respect to liquid nitrogen. The measured response and models parted past the first collapse and re-expansion; it is suggested due to an initially ellipsoid bubble. This study examined bubble motion at atmospheric pressure and an over-pressure of 98 kPa [36].

More spherical bubbles have been achieved by Tomita, Tsubota, Nagane and Annaka [37, 38]. These studies were performed for atmospheric and 147.1 kPa over-pressure. The important results of this study were to show that the Rayleigh solution agreed well with observation of the bubble during the growth stage, thus demonstrating that the inertial effects dominate during growth. The model then departs and shows that the thermal effects are prominent in collapse, in agreement with other research [36]. Taylor instability was also observed on the bubble surface; the bubble surface becomes less uniform and more rippled with each collapse and expansion. Taylor instability occurs where an initial perturbation, grows in magnitude because it is energetically favourable, these instabilities are common wherever a fluid acts on another of different density. Here the bubble vapour acts on the liquid phase.

2.6 Electric characterisation of nitrogen

The electrical characterisation of nitrogen in the gas and liquid phase has been widely studied. This section reviews breakdown data and highlights relevant theory and results when considering vapour bubble initiated breakdown in liquid.

2.6.1 Electrical parameters

An exact measurement of resistivity of liquid nitrogen has not been found, however it exceeds 10^{16} Ohms per metre [39]. A practical value for permittivity of liquid nitrogen at its boiling point (77.36 K) is 1.43-1.44 [14, 37]. A review of a range of dielectric loss measurements is shown in Figure 2.8. The losses have been found to vary with time and so can not be considered an intrinsic property of the liquid. Possible suggestions for the variance in measured results include; liquid impurities, electrode condition and space-charge effects near the electrode surfaces [40].

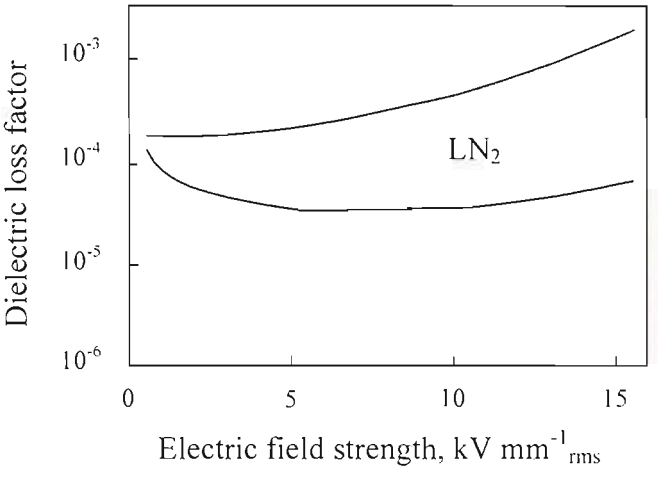

Figure 2.8, Range of experimentally measured dielectric loss versus electric stress at 50 Hz ac near boiling temperature [41]

2.6.2 Gaseous nitrogen breakdown

Bubbles induced by thermal and or electrical means in liquid nitrogen will contain nitrogen gas. Nitrogen gas follows the Paschen curve for breakdown and this is found to be independent of gas temperature. The Paschen curve for nitrogen, Figure 2.9, can therefore be considered representative up to fields of a few 10^7 V m^{-1}, at any temperature. Gas breakdown is known to be dependant on pressure and electrode gap spacing; breakdown voltage is therefore plotted against the product of density

number and electrode spacing, Nv.d. It is noticed that as for all Paschen curves there is a definite minimum density spacing number below which no breakdown will occur. This effect is due to there being too few electrons between the electrodes to collect sufficient energy for avalanche breakdown. Moving along the curve from the minimum density spacing number to the right, the breakdown level decreases as the number of energy collecting electrons increases.

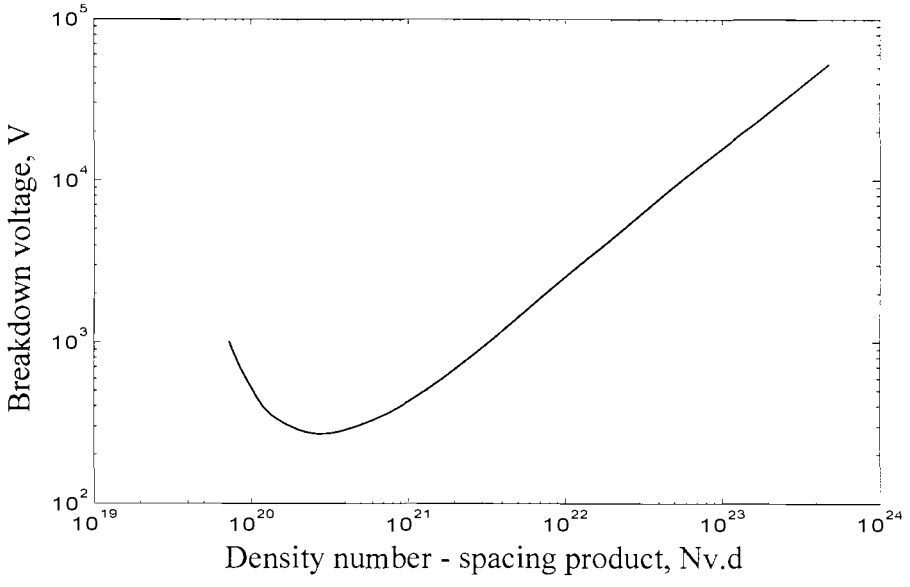

Figure 2.9, Paschen curve for nitrogen [40]

Another feature of Paschen curves is the minimum breakdown level. This occurs for the spacing number where the mean free path of the electrons accelerated by the electric field is largest relative to the magnitude of the electric field strength accelerating the electrons across the electrode spacing. Further increase in the density spacing number, either by increasing pressure or widening the electrode spacing, reduces the mean free path of the electrons relative to the accelerating electric field strength and a greater voltage is necessary to cause breakdown.

2.6.3 Liquid nitrogen breakdown

Characterisation of the dielectric performance of LN_2 is critical to its successful deployment within high voltage apparatus designs. A significant effort to study performance issues associated with the employment of cryogenic liquids has been undertaken. The breakdown process in liquids is perhaps less well understood than

in gases and even solids [42]. Liquid nitrogen displays many complex breakdown phenomena.

There have been several reviews by Gerhold considering the issues pertinent for the application of liquid nitrogen as a dielectric in HTS high voltage equipment [39-41, 43]. Breakdown phenomena in liquid nitrogen are well researched and there are many published works for different geometries, electrode materials, pressures and spacing. However, most published data are for small electrode spacings up to a few millimetres. No systematic studies on temperature against breakdown values have been published, but the liquid range is narrow and little effect might be anticipated. The validity of this assumption remains an open question.

Some of the parameters known to adversely affect breakdown performance of liquid nitrogen include; bubbles, contaminants, electrode material, electrode surface conditions, geometries of the electric field and type of stress (ac, dc, impulse) [39]. Breakdown voltage will be reduced by bubbles and conducting particulate causing local electric stress enhancement. Liquid nitrogen displays a "weak-link" breakdown mechanism, this is witnessed by statistical scatter, area and volume effects [44-46]. Thus fluid volume, flow rate and heat input will also affect the design of effective insulation systems. Bubbles within the liquid phase may occur by thermal heating, electrical induction or be trapped during filling and surface wetting. Electrical induction of bubble nucleation and pre-breakdown theory is discussed in more detail in Chapter 5.

Liquid nitrogen has a high dielectric strength that is comparable to some mineral oils when tested under suitable conditions [40]. The effect of pressure on breakdown data is shown in Figure 2.10 for 50 Hz ac breakdown. DC values are comparable to the ac peak values although there is a large scatter in results such as these up to 25% [39].

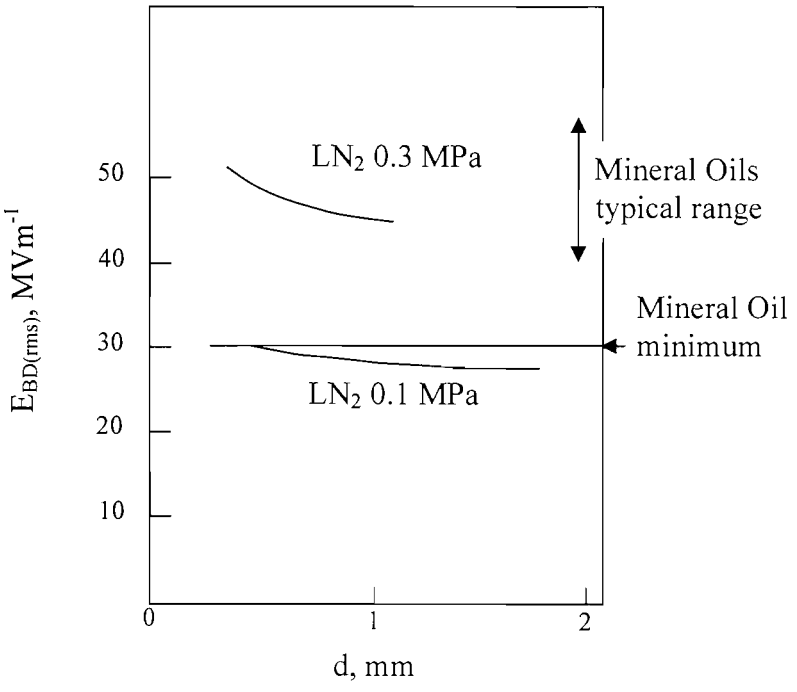

Figure 2.10, Mean ac breakdown field strengths against spacing (LN_2 data: 50Hz, 62.5mm spheres) [39, 47]

The most accepted explanation of breakdown mechanism in liquid nitrogen is that of breakdown initiated from vapour bubbles on the electrode surfaces. Bubbles are formed as a result of electrical energy input at high stress points. Electrons emitted at high stress points transfer their energy to the liquid molecules to excite them to the vapour state. The idea that a high electric stress is produced at an electrode causing an electron avalanche and vapour production is supported by pre-breakdown studies of which there have been a significant number for liquid nitrogen [48-56].

Cathode electrode emission causing bubble formation and growth in liquid nitrogen has been reported by Denat, Jomni, Aitken and Bonifaci [14, 53]. This research studied bubble formation on the tip of needles under a highly divergent field geometry for impulse-dc experiments and tip radii of 1-10 μm. In these experiments, it was found that to produce a bubble due to local energy input, the tip electric stress had to exceed 1.1 MV mm^{-1}. It was proposed that this level of stress can occur on conductors locally due to electrode aspirates or conductive particles. When the tip was of negative polarity there are current pulses of 10 ns duration, each current pulse being due to electron avalanches. Each current pulse caused the growth of a bubble at the tip which grew and then collapsed and rebounded. The behaviour was

complicated by the possibility of further pulses into the vapour phase of the bubble when a bubble was already active. It was found that the discharge into bubbles was eliminated at pressures above 1.6 MPa.

Their research detected only one rebound for bubbles in liquid nitrogen [53]. Maximum bubble radius was found to decrease with increasing pressure as expected. Experiments were carried out to 6 MPa and a dramatic decrease in maximum bubble radius was seen up to 2.5 MPa above which bubble radius did not significantly increase. From this it can be concluded that the dielectric strength of liquid nitrogen is adversely effected by bubbles whether thermally or electrically induced and one possible way to minimise the degrading of dielectric performance due to bubble nucleation is to increase applied pressure.

2.7 Thermal bubble breakdown

It has been stated that liquid nitrogen at 77 K can have a dielectric performance to equal room temperature oils [41]. However LN_2 has a latent heat of 199 kJ kg^{-1} and a very narrow liquid range of 14.31 K, as compared to 330 K for oils; thus bubble generation can occur more readily where there is a heat input. Heating may occur in HTS equipment which undergoes quench, for example in HTS fault current limiter coils [57] which in addition to bubble nucleation also results in a high-voltage drop across the coil layer. Also HTS equipment designs such as transformers, cables and terminations have the requirement to transport energy from ambient to cryogenic temperatures. The competing requirements of good electrical conduction and low thermal conduction mean that even at continuous rated current there will be significant heat input into the cryogenic region.

In the application of high temperature superconductors, designs that propose the use of liquid nitrogen both as the coolant and a liquid dielectric must address the concern that thermal bubble generation will have a detrimental effect on the dielectric performance. This issue has been considered by a few researchers. A vapour bubble within liquid and in the presence of a non-uniform field is subject to dielectrophoretic force. This force arises due to the lower relative permittivity of the vapour to the liquid. With moderate heat input discrete bubbles may form, with

increased heat injection a phenomena known as vapour locking may occur. With very high heating a transition to film boiling may ensue.

The main contributor to research into thermal bubble initiated breakdown is Hara who with various co-authors has published several papers in this area [15, 58-63]. This research began with a parallel rod-plane electrode system having a heat source mounted on the earthed rod electrode. With liquid nitrogen at around 77 K and at 0.1 MPa a dc voltage was ramped at 1 kV s^{-1}, gaps of 1.2 and 2.6 mm were used. It was found that for low heater powers no bubbles were detected until breakdown. Therefore in this region the breakdown develops through the liquid. Breakdown levels in this mode were found to be around 29 kV mm^{-1}. Increasing heater power caused discrete bubbles to occur. In this region as the voltage was applied bubble nucleation was retarded until it suddenly become a spheroid bubble fixed to the earth rod electrode. Further increasing the voltage caused the bubble to form a cone shape stretching out from the fixed heater location towards the plane electrode. Breakdown in this region is through a composite of liquid and vapour phases. For higher heater powers marked by bubbles coalescing as voltage increases there becomes a point when the bubble suddenly forms a vapour column bridging the gap. In this mode breakdown occurs through the vapour column and correlates well with breakdown levels expected by the Paschen curve. So called "vapour locking" occurred at a voltage almost independent of heater power and always lower than breakdown voltage [58].

This work has been extended to vertical and horizontal parallel plates. Voltage-time characteristics of the phenomena have also been investigated [59]. It was found that it takes a finite time for vapour locking to occur, this was measured to be 1ms, for the experimental conditions under study, so that vapour locking is not seen for impulse waveforms even if the peak is much higher than the breakdown level. It was found that ac voltages could, however, cause vapour locking.

Three mechanisms of breakdown were identified, dependent on the rate of ramped voltage. With a fast rising edge of the order of 10 kV μs^{-1} no bubble deformation occurs. Breakdown could occur through bubble and liquid composite. With a medium ramped voltage of the order of 10 kV ms^{-1} a large bubble is elongated in

which a discharge is triggered. With a slower ramped voltage of the order of 0.1 kV ms^{-1} boiling turns from nucleate to film at an earlier stage and the fixed bubble grows to bridge the gap as a vapour column before breakdown. This reduces the heat transfer to the liquid [15] and has implications for superconducting systems where hotspots result in an increase in the local electric field, further reducing the effectiveness of the insulation system.

This work has been extended to the application of HTS coaxial coils [63, 64], and has included the examination of pressurising and sub-cooling effects on breakdown and partial discharge (pd) under boiling regimes for different heater powers. It was found that at lower heater powers, the pressurising and sub-cooling effect was very effective at suppressing bubble generation and raising the inception voltage of pd activity. As anticipated, bubbles that were generated liquefied more rapidly in the pressurised system. As pressure was increased the charge associated with the pd increases with the inception voltage, the number of pd events reduces and activity retards in phase. The solid parts of the insulation system were found to be damaged by pd activity upon examination after experimental completion. Importantly, it was found that at elevated pressures, up to 0.25 MPa, breakdown could occur without prior observation of pd activity.

2.8 Summary

This chapter has considered the properties of liquid nitrogen as a cryogenic coolant and a dielectric fluid. Liquid nitrogen is ideally suited to HTS applications by its liquid temperature range and chemical inertness. Bubbles may occur due to heat input, or high electric stress.

The issue of bubble nucleation due to thermal induction has been considered and pool boiling theory and conditions affecting bubble nucleation have been reviewed. Published research on bubbles in liquids has been approached from several angles; latent heat transfer and boiling, cavitation and acoustics, laser induced and electrical breakdown. Boiling phenomena and the life-cycle of bubbles i.e. nucleation sites, initiation, growth and detachment have been considered. Models of free bubbles in bulk liquid have also been discussed. Although theoretical treatment of free bubbles is highly idealised it has lead to some instructive results. It has been concluded from

laser induced bubbles in LN_2 that inertial effects dominate the growth of the bubble and that thermal effects dominate collapse. Taylor instability has also been observed, where the bubble surface becomes less uniform with every collapse and re-expansion.

Considerable data exist to characterise the electrical performance of nitrogen and breakdown data exist for both gaseous and liquid nitrogen. Liquid nitrogen breakdown data have been published in abundance for a range of pressures and geometries. It has been demonstrated that liquid nitrogen displays area and volume effects. The breakdown data are influenced by bubbles, contaminants, electrode material, electrode surface conditions, geometries of the electric field and type of stress (ac, dc, impulse). Insulation system performance will therefore be dependant on flow rate, volume and heat input.

The mechanisms of electrical breakdown in liquid nitrogen are complex and are still being studied. The most accepted theory is that the application of an electric field leads to initiation of breakdown from vapour bubbles due to electrical energy input in the form of electron avalanche. Partial discharge studies in many dielectric liquids have been performed. Electrically induced vapour generation from pre-breakdown discharge has been observed and this continues to be an area of active research.

It has been found that electrical fields influence the behaviour of bubbles and transition between boiling modes. Much progress has been made in the last two decades by Hara and colleagues who have shown that the rate of application of applied stress influences the growth of vapour bubbles and channels within liquid nitrogen and has a significant effect on the mechanism leading to breakdown with the appearance of vapour locking. This area is not fully developed and a systematic study of the effects of a range of temperatures, pressures and field geometries for liquid nitrogen has not yet been undertaken.

Chapter Three

Cryostat design

3.1 Introduction

The study of the dielectric properties of LN_2 for application in HTSC cables requires the optical observation of bubble nucleation and dynamics, measurement of pre-breakdown phenomena and partial discharge accomplished with experimentation of realistic cable and termination geometries. To accomplish this, a unique cryostat has been designed and manufactured to enable optical and electrical measurement of pre-breakdown phenomena in liquid nitrogen. The cryostat allows characterisation of potential failure mechanisms of liquid nitrogen as a dielectric fluid for a range of pressures, temperatures, heat inputs and applied electric stresses. The cryostat is the central apparatus in the experimental arrangements used in the research presented in this thesis. The design, manufacture and certification process were completed before experimental work began.

Initially a comprehensive review of current experimental research in this field was undertaken and the cryostat designs employed were evaluated. There are broadly two groups of test vessel used, the division broadly following the two areas of interest; bubble dynamics, and pre-discharge phenomena. For studies of bubble dynamics, including area and volume effect studies, larger vessel capacity is a

primary design driver [44, 63]. This in turn influences the upper limit on pressure, as the larger areas of the vessel walls carry larger mechanical loads. Where high pressures for studies on pre-breakdown phenomena are desired, small test chambers are used [53]. Vessels designed for either role are sometimes conduction cooled, however the most favoured approach to maintain temperature is sacrificial pool boiling, either in an outer jacket or in a cooling loop around the inner vessel [52, 53, 63]. Drawing a vacuum on the liquid nitrogen outer jacket can then be used to reduce the temperature of the liquid; and by conduction the temperature of the liquid within the inner test vessel is reduced into the sub-cooled region.

The effects under investigation involve fast motions and an imaging system capable of image capture of high speed events has been specified and assembled for use with the cryostat.

3.2 Initial specifications

The specifications for the cryostat and associated apparatus were established before the design process began, these requirements are summarized below. The cryostat designed is for the study of bubble dynamics studies in addition to pre-breakdown phenomena. This necessitates a large vessel accommodating samples with embedded heat sources. A large vessel volume allows a greater size of sample that can be accommodated. This is desirable for the testing of "realistic" size test pieces and geometries with consideration of superconducting cables and termination designs. Reported designs cite single phase core diameters of a conventional dielectric HTSC cable being around 60 mm; with three core assembly of 128 mm and outer pipe diameter of 192 mm [9, 11, 65]. The size of the test chamber, the inner vessel of the cryostat, was therefore specified so that the cryostat could accommodate test pieces of this size. The limiting factors to large vessels are mechanical strength to hold the pressure, and thermal radiation. Typical cryostat designs employ a long thin design to reduce permitted thermal radiation at the top plate from heating the liquid nitrogen below. A larger ratio of diameter to length would mean that this feature of the design would be less effective.

A larger vessel size has implications for the pressure rating as the larger surfaces will carry greater mechanical loads. A pressure range 0-2 MPa was specified considering

possible operating conditions for future superconducting cables; LN_2 entry pressures of 2 MPa and exit pressures of 1 MPa have been quoted [11, 65, 66]. The pressure rating in turn influences the choice of material and thickness, this extends to all parts of the inner pressure vessel including the optical ports, plumbing and electrical fittings.

The liquid phase of nitrogen at 1 atmosphere (0.1 MPa) of pressure is between 63.05 K and 77.36 K. In a vacuum of 0.01 MPa the boiling point decreases to approximately 63 K, and at 2 MPa this is raised to around 116 K. HTS cable and terminations are designed to operate with LN_2 at between 65 K to 95 K [9, 67-69]. The cryostat would therefore have to be capable of achieving temperatures down to 60 K, whist supplying the thermal losses of the system. The cryostat was designed with the aim of minimising the heat loss from radiation, conduction and convection. To characterise behaviour of nitrogen over the liquid range as a function of temperature correctly, temperature sensing to resolve to one degree or better was specified.

One of the main sources of data for this project is the images of bubble life-cycle and dynamics under different conditions, with and without electric fields or discharges. The apparatus design must allow good imaging of the bubbles and investigation of their behaviour. Based on published work it was anticipated at the design stage that a CCD camera with a greater than 2000 frames per second (fps), frame rate would be required [15, 70] to operate in conjunction with suitable light sources and optics.

To study the effect of electric fields of varying configuration and strengths on bubble lifecycle, shape and pre-breakdown phenomena requires the design of a suitable high voltage (HV) bushing. A 132 kV bushing was specified, since it is a commonly used operating line voltage in transmission networks. This allows realistic cable voltages of 132 kV line or 76.2 kV phase to be applied across test samples.

At a pressure of 2 MPa the local temperature to produce a bubble must exceed 116 K. It is necessary therefore, that samples, with embedded heat sources, are capable of supplying the energy required. These heat sources have to be designed into the desired sample geometry.

3.3 Design overview

The cryostat described was designed and manufactured by the Electrical Power Engineering Research Group (EPE) with advice from the Institute of Cryogenics at the University of Southampton. The final design allows steady state control of temperature in the sample chamber down to 63.5 K and can be held constant to within 0.3 K. The large test chamber allows relatively large samples to be accommodated within a space 280 mm in diameter by 250 mm in height. The vessel is certified for working pressures up to 2 MPa. Voltages up to 76.2 kV can be applied via a filled epoxy bushing. A range of lighting and imaging configurations are possible via four optical ports at strategic positions around the vessel circumference.

A schematic diagram of the cryostat design is shown in Figure 3.1. The cryostat is a two wall concentric cylinder construction with a vacuum and super-insulation inter-space between the inner pressure vessel (1) and the outer jacket (2). The two main vessels, flanges and top plate (3) are all constructed of 316L grade stainless steel. Sapphire windows (4) utilising indium seals complete the inner pressure vessel and BK7 optical grade glass windows (5) with rubber o-rings are used to finish the outer vacuum jacket. A helium-expander cryo-cooler (6) is integrated into the vacuum inter-space to cool the cryostat inner vessel. A copper thermal lead-through (7) is incorporated into the bottom of the inner vessel and connected to the helium expander by a copper flexible coupling (8) to allow for thermal contraction of the inner vessel.

A custom made Voltalit, filled epoxy resin bushing (9) cast by Pirelli allows voltages up to 76.2 kV to be applied. The bushing is earth screened along its length within the test chamber by semi-conducting paint and terminated (10) at the bottom end below the level of the liquid nitrogen. The top of the bushing is terminated outside the vessel with paper tape insulation and a Voltalit encased stress relief cone within a gas chamber containing sulphur-hexafluoride gas (11). Two corona shields allow shielded connection of a high voltage supply (12).

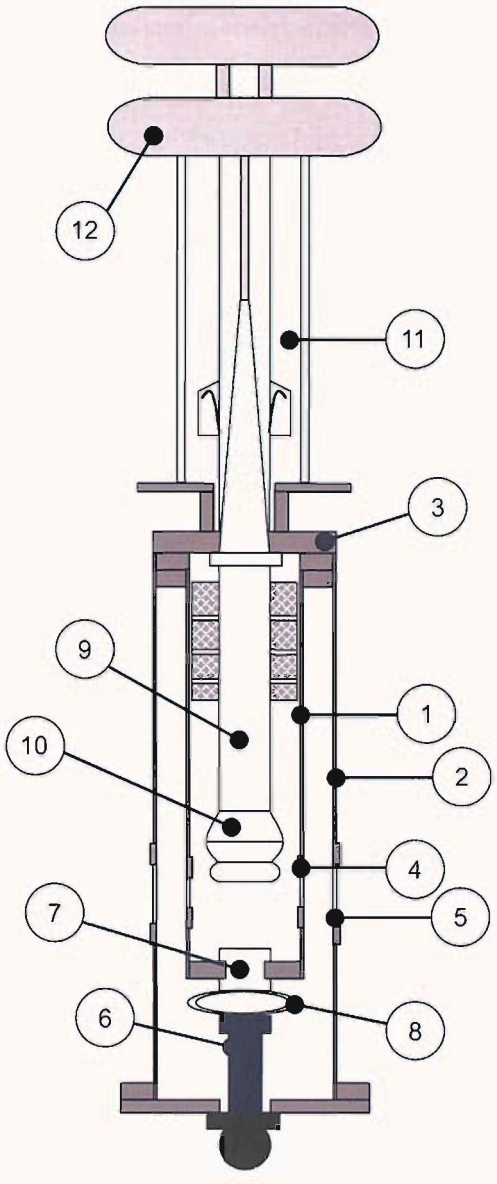

Figure 3.1, Schematic diagram of the cryostat

3.4 Temperature control

Many cryostats designed for experimentation in liquid nitrogen achieve sub-cooled temperatures by means of a sacrificial pool boiling liquid nitrogen jacket or continuous-flow cooling loop within the vacuum inter-space between the inner vessel and outer jacket [52, 53, 63]. This design utilises a Helium filled cryo-cooler supplied by Leybold Vacuum UK Ltd fitted into the vacuum inter-space and coupled to the inner vessel. This allows sub-cooling of the liquid nitrogen down to 63.5 K without the need for refilling as with sacrificial cooling systems. This effectively

prevents the generation of bubbles and density fluctuations that adversely affect both the optical measurement and the experimental conditions for the sample under test.

The cryo-cooler system consists of the coldhead (model, RGS120T) and the helium compressor pack (model, coolpak 6000), connected with flexible insulated hoses, Figure 3.2. These are all supplied as a complete system by Leybold Vacuum UK Ltd. The coldhead is a single-stage helium piston-expander, capable of 120W cooling power at 77 K. The cold-head is connected to a copper block, which forms part of the bottom plate of the inner pressure vessel to provide a thermal feed-through to the LN_2. The coldhead of the cryo-cooler is coupled to the inner vessel via a flexible coupler, Figure 3.3, and the cryo-cooler bottom flange seals with the cryostat outer body to form the outer vacuum jacket. The flexible coupler is manufactured from multiple sheets of thin copper. The copper sheets were cut, folded and soldered at each end to oxygen-free-high-conductivity copper (OFHC) plate. The flexible coupler is capable of transmitting the heat from the vessel to the cryo-cooler coldhead, whilst allowing the inner vessel movement for thermal contraction.

Figure 3.2, Leybold coldhead RGS120T

Figure 3.4 shows the curve of cooling capacity for the RGS120T cold head and coolpak 6000 compressor as well as the curve for thermal conductance of the flexible

coupling. The flexible coupling thermal conductance is calculated using the equation for heat transfer for a perfectly insulated conducting bar. i.e.

$$\dot{Q} = -kA\frac{dT}{dx} \tag{3.1}$$

Where $\dot{Q}$ is rate of heat transfer (W), k is the thermal conductivity ($W.m^{-1}K^{-1}$), A is the cross sectional area of the conductor (m^2), T is temperature (K) and x is displacement (m) along the bar in the direction of the temperature gradient; the negative sign indicates the temperature gradient increases in the opposite direction to increasing x. Thermal conductivity values for copper range between 385 and 401 $W.m^{-1}K^{-1}$. The lower value of 385 $W.m^{-1}K^{-1}$ was used to provide a conservative estimate of conductivity through the flexible coupler. Sixty flexible copper sheets were used, these are 150mm wide, 0.3mm thick and have an average length of 220mm. Thus the heat power per degree temperature difference along the coupler can be calculated as;

$$\frac{\dot{Q}}{dT} = \frac{-kA}{dx} = \frac{-385\times0.015\times0.0003\times60}{0.022} = -4.725\ WK^{-1} \tag{3.2}$$

Plotting this curve along with the cooling curve (Figure 3.4) shows that if the top face of the copper coupler is to be maintained at 65 K the maximum thermal losses into the vessel that can be supplied by the cooling system is 85 W.

Figure 3.3, Flexible copper coupling

The RGS 120T coldhead is connected by flexible high pressure gas lines to a coolpak 6000. The cryostat is cooled by means of the Gifford-McMahon cycle. High pressure Helium (up to 2.1 MPa) is fed from the coolpak to the coldhead. The piston within the coldhead expands the gas, absorbing heat transmitted by the flexible copper coupler from the cryostat inner vessel. This relatively hotter Helium is then returned to the coolpak, re-compressed and passes through gas purifiers and a water cooled heat exchanger. Then the Helium is again pumped out to the coldhead. This cycle necessitates the use of an external water cooling loop. During steady operation at 77 K this process requires cooling power of 6 kW. During initial cool-down, however, the required power starts at 8.2 kW with the coldhead at room temperature.

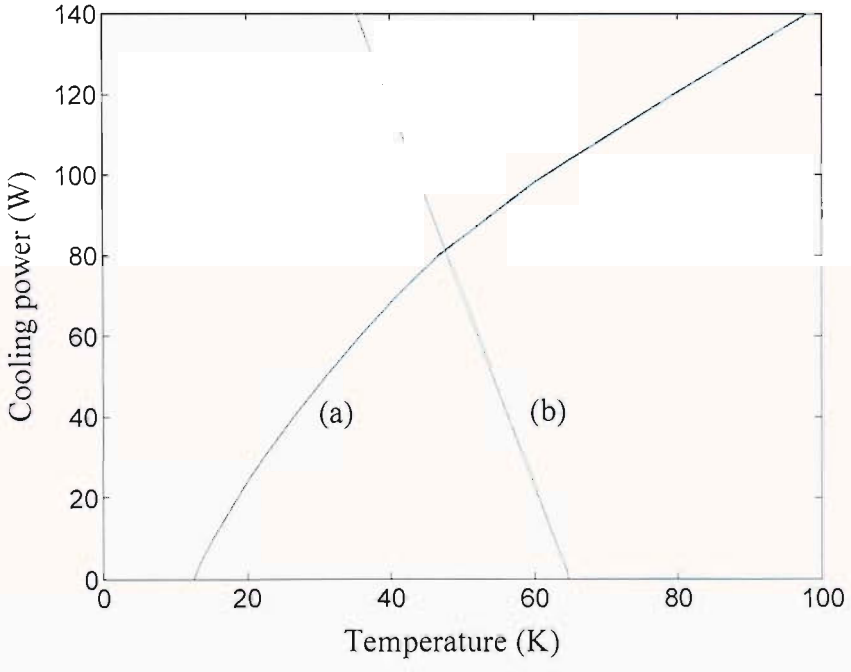

Figure 3.4, (a) Cooling capacity curve for the coldhead RGS120T with coolpak 6000 and (b) thermal conductance of the coupler

An 11 kW water-chiller with a forced air cooled radiator is employed to cool the water fed around the coolpak heat exchanger. On the return circuit the heated water pumped from the coolpak heat exchanger is first piped to a cooling loop attached to the top end of the cryostat outer vessel before reaching the water chiller. The cryostat top cooling-loop consists of three parallel 6 mm diameter copper pipe loops located around the circumference of the outer jacket just below the level of the top-

plate, Figure 3.5. In this position, heat generated by the coolpak conducts into the stainless steel top flanges. This arrangement maintains the temperature of the main PTFE o-rings sealing between the two vessels, near room temperature. This ensures the integrity of the seal between the inner pressure vessel and the vacuum inter-space, and at the top-plate between the inner pressure vessel and atmosphere.

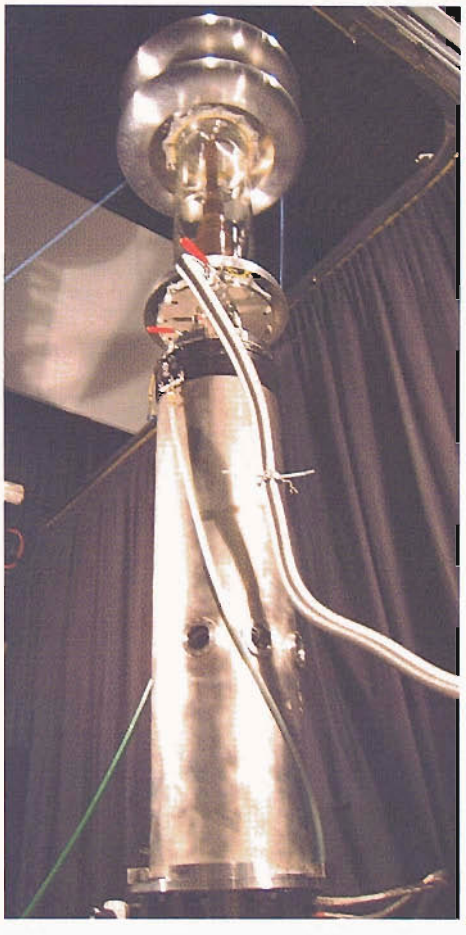

Figure 3.5, Cryostat with bushing

The vessel is insulated with multiple layers of super-insulation (aluminised plastic film) wrapped around and secured to the inner vessel within the vacuum inter-space. This common technique provides multiple radiation reflecting barriers. Using a turbo-molecular pump the pressure in the inter-space is reduced to below 10^{-5} Torr minimising convection heating of the inner vessel. Additional insulation to minimise convection cooling of the top plate is provided by buffets located on the inner surface of the top plate and supported by the high voltage bushing. The buffets are cut from marine grade expanded foam sheet with provision for top plate couplings and are

capable of withstanding the rated pressure of the vessel. An aperture sufficient to allow significant gas flow has been provided around the pressure relief valve port.

The temperature in the vessel is controlled by continuously running the cyro-cooler, thereby supplying cooling sufficient to match any heat leaking into the vessel. Additional cooling power is balanced by two 100 W electric cartridge heaters mounted within the top of the flexible thermal coupling and controlled to maintain equilibrium at the desired temperature. The heaters are used as the control elements due to their shorter thermal time constant, compared with that of the cryo-cooler allowing more stable control of the vessel temperature. The control loop is closed by temperature feedback using a pt100 platinum resistance thermistor capable of resolving temperature to within 0.3 K. This thermistor is also mounted within the top of the flexible thermal coupling. A three term controller is employed to control the ratio of on to off time for the heaters. Stable temperature control in the range 63.5-116 K is achieved in the cryostat. This corresponds to the liquid phase of nitrogen between atmospheric pressure and 2 MPa (Figure 3.6). There is no minimum temperature interlock and the operator must take care not to reduce the temperature below the saturation curve as this will cause solidification of the nitrogen at any given pressure.

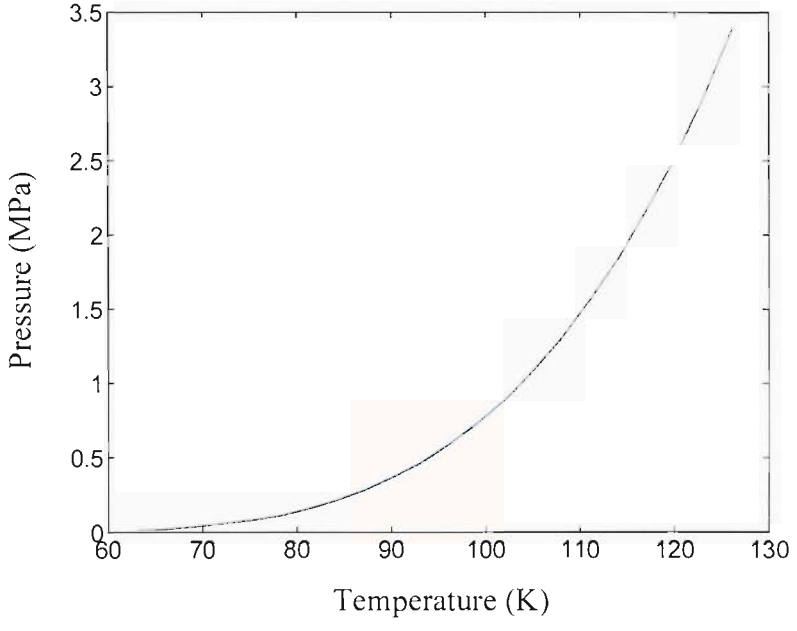

Figure 3.6, Nitrogen saturation curve [71]

3.5 Pressure vessel

In published designs for liquid nitrogen cooled superconducting cables, the liquid nitrogen employed as coolant and dielectric is pressurised to 2 MPa at the inlet; with the pressure dropping across the cable length to predicted exit pressures of 1 MPa [11, 65, 66, 72]. In order to characterise bubble dynamics and pre-discharge phenomena under conditions applicable to power apparatus, the vessel is designed for experimental pressures up to 2 MPa. The product of the pressure and volumetric capacity is greater than 50 bar-litres, therefore the vessel must be certified in line with PD5500:2000, the British standard for unfired fusion welded pressure vessels.

When working to PD5500 the designer must select which category the pressure vessel will be designed to, this determines the tolerable mechanical stresses in the load bearing materials and the level and type of required manufacturing inspection and testing. Category three was selected because although the design stresses have to be kept lower, no non-destructive testing (NDT) is required, only visual examinations and checks are performed, reducing the manufacture time and cost.

The next step in the design and manufacture of a pressure vessel to PD5500 was to design the vessel within limits determined by the relevant sections of the standard. The completed design was submitted for checking and approval by the designated Inspection Authority (IA). The IA for this vessel was Zurich Insurance. The IA is responsible for design approval, weld procedure approval, compliance checks, final weld examination, and witnessing of intermediate and final hydrostatic pressure tests.

The cryostat design was approved by the IA prior to manufacture. The cryostat materials were authenticated by the IA against the supplied material certificates. Weld procedures were confirmed by the IA and pre-weld tac-up alignment and dimensional checks were made and final visual weld inspection performed. The completed vessel was hydrostatically tested at two stages. First it was tested with stainless steel blanking plates over holes provided for fittings. The final hydrostatic test was performed with all final fittings in place. The vessel was tested at 3 MPa for

30 minutes, this test was witnessed by the IA who approved the vessel for experimental use.

3.5.1 Vessel design

The cryostat inner pressure vessel is designed with a working pressure of 2.2 MPa. This is the difference between the operating pressure of 2.1 MPa and full vacuum of the inter-space. The operational pressure for the design is 0.1 MPa greater than the desired experimental pressure to allow a margin for the pressure safety valve to operate in. A safety relief valve set to operate at 2.2 MPa is fixed to the vessel top-plate and will operate if the vessel is over-pressurised erroneously, preventing the vessel from exceeding its safe working limit.

The pressure vessel is formed of a tube, with two flat ends all manufactured from 316L stainless steel and four sapphire windows. 316 stainless steel is a common cryogenic engineering austenitic steel grade, 'L' designates antimagnetic specified to reduce effects from the currents passed in experimental use. The tube selected has an inner diameter of 300 mm and a wall thickness of 3 mm. Calculation of the tube wall thickness needed to withstand the pressure requires knowledge of the steel properties. The tube was manufactured in Sweden to a standard grade SS2343-23, with a minimum ultimate tensile strength of R_m of 510 MPa and yield strength (1% proof stress) $R_{1.0}$ of 250 MPa. Under category three for this material the design stress is not permitted to exceed 120 Nmm^{-2} provided the yield stress is greater than 230 Nmm^{-2}. The minimum thickness for pressure loading was calculated using;

$$e = \frac{p \times D_i}{2f - p} = \frac{2.2 \times 300}{(2 \times 120) - 2.2} = 2.775\text{mm} \qquad (3.3)$$

Where e is the wall thickness (mm), p is pressure (MPa) and D_i is the vessel inner diameter (mm); f is the design stress taken from PD5500 for stainless steel 316 grade S33/53. Using thick wall tube theory it is also possible to calculate a theoretical pressure for non-elastic deformation of the pressurised tube using the value for the 0.2% yield stress, $R_{0.2}$.

$$p = \frac{e \times 2 \times R_{0.2} \times JF}{D_o} = \frac{3 \times 2 \times 220 \times 0.85}{306} = 3.6667 MPa \qquad (3.4)$$

Where JF is the joining factor for a robot welded seam and D_0 is the tube outer diameter (mm). Given this result and the operating pressure, 3 MPa was chosen as a suitable hydrostatic test pressure for certification of the vessel.

The provision for connection of the HV bushing and other fitting to the top plate necessitated a flat end plate design for the top plate. A flat end plate was chosen for the bottom of the vessel in preference to a domed end to gain the greatest volume, required to accommodate large samples. The flat end was also simpler to manufacture and allows ease of connection of the cyro-cooler into the bottom of the inner vessel. To connect the flexible coupler from the cryo-cooler a copper thermal feed-through was machined to fit a hole in the stainless steel bottom plate. The size of this vessel with an internal diameter of 300 mm and the additional requirement that it does not deflect substantially, led to the use of a 30 mm thick end plate. Full calculation of plate thicknesses is shown in Appendix A, Section A.1 and A.2.

The copper thermal feed-through was sealed to form the inner pressure vessel by using a common cryogenic engineering technique namely a knife edge profile seal. The bottom face of the copper is cut into by the stainless steel profile when it is clamped so that the differential thermal contraction of the copper and stainless steel components assists in maintaining the seal when cooled to 63.5 K. It was noted that adequate pretension of the bolts is needed to make a sufficient impression in the copper to seal well and maintain the integrity of the seal when cooled. It proved difficult to calculate the torque to be applied because copper deforms under the applied pressure. Trial and error led to the tightening of bolts to 15 Nm. Sixteen evenly spaced hexagon top bolts were used in the stainless steel clamping ring and were tightened evenly using a criss-cross pattern. These bolts have been retightened after each cooling-heating cycle and it was found that no more tightening was required after the first five cycles. The vessel has been thermally cycled over 40 times and the integrity of this seal has been maintained.

Fittings for services including vacuum, electrical feed-throughs and gas connections have been carefully selected to operate at the vessels working pressure safely. The section of vacuum line attached to the vessel will see 2.0 MPa in service. Vacuum products are only rated to 0.5 MPa if at all. Size NW 40 vacuum fittings are used between the turbo-molecular pump and the vessel, the large bore providing higher pumping rates. For this reason a 1½" (38.1mm) bore ¼ turn ball tap capable of taking 2.0 MPa is used at the vessel top plate. A special adapter has been turned to couple the vacuum to the screw thread pipe fitting of the ball valve. Two Hansen couplings are fitted to the top plate allowing connection of gas lines for vessel pressurisation.

Two electrical feed-throughs for signals into the vacuum jacket are made via a vacuum fitting cross-piece at the bottom plate. One feed-through is for signals; the other has a higher current rating for the temperature control cartridge heaters. Two further, marine grade electrical feed-throughs capable of withstanding the operational pressure have been fitted to the top plate. One is a signal feed-through; the other has a higher current rating to allow supply to heat sources that may be used within samples.

3.5.2 Optical ports

Optical ports are placed at four locations 0, 45, 90 and 180 degrees around the vessel circumference at 169 mm above the bottom plate. The outer windows are borosilicate crown glass (BK7) optical grade glass with high homogeneity, low bubble content and excellent transmittance in the visible light range (Figure 3.7). The inner windows are manufactured from sapphire. Anti-reflection (AR) coating has been applied to both sides of the inner BK7 and outer sapphire windows. AR coatings are selected based on the light wavelength of interest, the angle of incidence and the damage threshold which is very important for use with lasers. The AR coating selected for the BK7 is an industry standard HEBBAR coating for visible light reducing the reflectance to below 0.5 % in the range of interest. The BK7 windows are 6 mm thick 75 mm diameter with 65 mm of viewable area. These windows form part of the outer guard vacuum jacket and are sealed with a stainless steel clamping ring, rubber o-ring and groove.

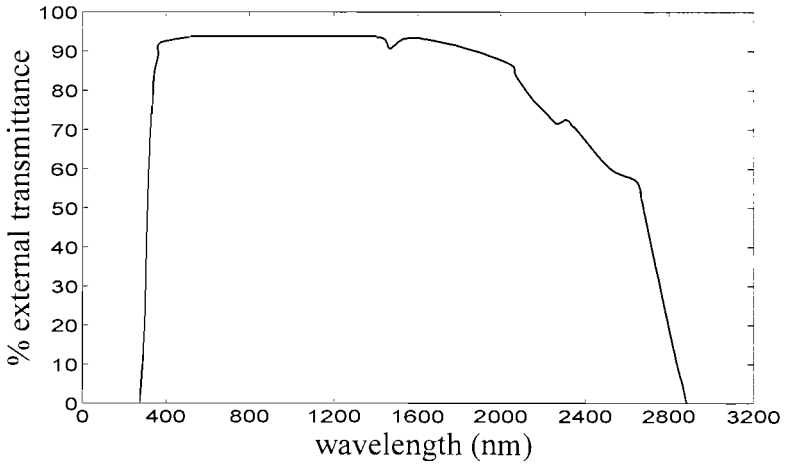

Figure 3.7, Transmittance of BK7 windows

Sapphire was chosen for the inner windows since these form part of the pressure vessel. Sapphire has good mechanical and optical properties (Figure 3.8) and is mechanically stable in the liquid nitrogen range.

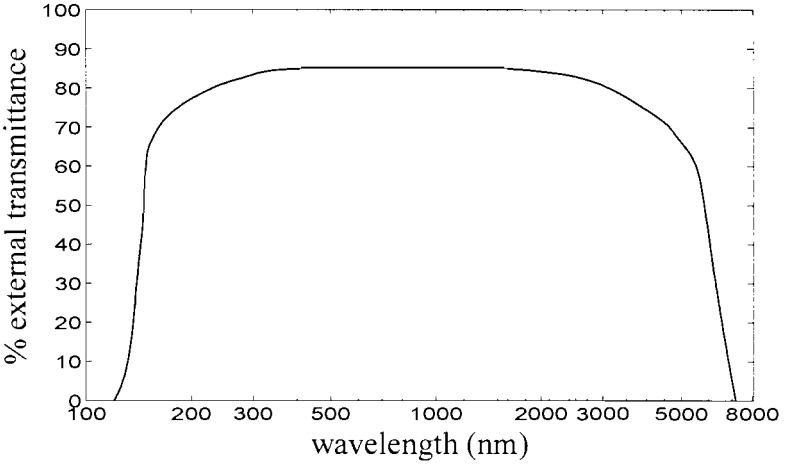

Figure 3.8, Transmittance of sapphire windows

Experimental burst pressure data published by the cut sapphire supplier, Agate Products Ltd, allows calculation of the window thickness required for safe working at the specified operating pressure. With a safety factor of four, a window with a total diameter of 50 mm and viewable area after clamping of 40 mm diameter requires a window thickness of 4 mm. These windows are sealed using indium wire in a partially trapped configuration (for a further example of this approach see [73]).

3.5.3 Top-plate bolting

Thirty-two A4 stainless steel M12 bolts are used to hold the top-plate to the top flanges and form the pressure vessel. These are of sufficient strength to withstand the force applied to the top plate in service and maintain the pressure seal. In addition to perform this function they have to be correctly pre-tightened to a calculated torque related to the bolt pre-tensioning. The torque applied to the thirty-two M12 bolts is calculated using guidelines published by a German bolt manufacturer which relate to the VDI2230 standard. This method accounts for operator error when tightening, torque wrench precision, lubrication in addition to preload applied to the bolt. The final preload torque is calculated to 95 Nm which includes a safety factor of 2.4; details of this calculation are given in Appendix A, Section A.3.

The M6-25mm A2 stainless bolts used to support the inner vessel when the top-plate is removed have a preload torque calculated by the same method. The number of bolts used was chosen to ensure good sealing between the flange and top-plate faces and so that the torque required does not exceeded the maximum of the bolts. These were initially torque set to 8 Nm; this was calculated to be more than sufficient to carry the inner vessel full of water as was the case during the pressure test, estimated at 130kg.

3.6 High voltage bushing

The HV bushing design is in effect a modification of two existing Pirelli termination designs placed back to back. The outside diameter of the bushing was set at 80 mm as with the existing design and mould. By consideration of the electrical design requirements the outside diameter of the conductor was chosen to be 30 mm. The optimum ratio of the inner and outer diameters is governed by the equation for maximum electric stress between conductors of a coaxial system, the maximum stress neglecting space charge effects occurring on the inner conductor surface;

$$E = \frac{V}{r \times \ln\left(\frac{R}{r}\right)} \tag{3.5}$$

where, E is electric stress (kV/mm), V is voltage (V), R is the outer conductor radius (mm) and r is the inner conductor radius (mm). It can be shown therefore that the optimum ratio for minimum electric stress occurs when the natural logarithm of the ratio of outer radius, R, to inner radius, r, is equal to one, i.e.

$$\text{when } \frac{R}{r} = \frac{1}{e} \tag{3.6}$$

With the outer semi-conductor paint radius set at 40 mm the optimum inner radius is 14.7 mm, a diameter of 29.43 mm the inner conductor has therefore been made from 30 mm diameter Aluminium tube.

The existing Voltalit termination designs utilized are rated for 132 kV line / 76.2 kV phase. However, using the diameters of the conductor and the outer diameter of the Voltalit theoretical maximum voltages can be calculated using design data from test results of Voltalit [74]. For full lightning impulse tests (1.2/50 μs waveform) the minimum failure stress for Voltalit at both 77 K and 300 K was measured as 109 kV mm^{-1}. These tests were performed for uniform field gap arrangements, but they can be used to provide an indication of expected performance within a coaxial system. Therefore the estimated voltage for failure within the coaxial bushing for impulse voltages can be estimated using Equation 3.5. In this case,

$$V = 109 \times 15 \ln\left(\frac{40}{15}\right) = 1.603 \text{ MV} \tag{3.7}$$

Tests were performed on samples of the same configuration under applied ac stress, ramped to failure. Under ac stress the Voltalit performed worst at 300 K. Taking a gap of 25 mm minimum breakdown voltage was recorded as 27.7 kV mm^{-1}. Failure of the bushing under ac stress can therefore again be estimated using Equation 3.5.

$$V = 27.7 \times 15 \ln\left(\frac{40}{15}\right) = 407 \text{ kV} \tag{3.8}$$

By taking the minimum breakdown values for these calculations these results indicate the approximate outside limits that the bushing will withstand, up to

approximately 1.6 MV for impulse voltages and up to 407 kV for ac voltages. These are only approximate values due to small data sets and no account has been taken of area and volume effects. These values are useful however in providing confidence that the bushing will withstand voltages up to the operating voltage of 80 kV, significantly below the limit set by the above calculation.

The high voltage bushing is clamped to the top-plate with a stainless steel clamping ring. The bushing extends down from the top-plate and is terminated below the level of the liquid nitrogen. Voltalit, a fused silica filled epoxy, was selected as the material of choice for the bushing due to its electrical strength, and its ability to withstand cryogenic operation as well as a temperature differential between liquid nitrogen and ambient temperature along its length. The bushing conductor is a thin wall aluminium tube to minimise thermal conduction; this is acceptable electrically as there is no requirement to carry significant current. Aluminium was selected as it has the closest matching thermal contraction to Voltalit [74]. Welded sections of solid aluminium rod are used to cap either end of the conductor to ensure the bushing withstands the vessel operating pressure. The Voltalit bushing is electrically screened within the test chamber using a coating of semi-conducting paint which is earthed. This allows helium to be used to pressurise the vessel without the dielectrically weak gas being electrically stressed. The earth screen is terminated within the dielectrically strong liquid nitrogen by a stress relieving profile formed by winding conducting tape onto wound crepe papers built into the desired profile. This arrangement is over wound with wire to secure it firmly and carry any capacitive current that may be seen in normal operation.

The top of the bushing is terminated in a chamber filled with sulphur hexafluoride, a gas with high electrical withstand. The tapered top of the Voltalit comes through the top plate and paper tapes were built up around the tapered section until parallel to allow positioning of a Voltalit encased electric stress relieving cone. Paper tapes were applied to the conductor with decreasing diameter as far as the top of the sulphur hexafluoride gas chamber. A glass column forms the sulphur hexafluoride gas chamber providing electrical insulation between the cryostat top plate and applied high voltage. The very top is fitted with two corona shields to allow the connection in air of applied voltages up to the rated voltage. This bushing and

termination arrangement has been electrically tested and rated for operation up to 80 kV, and shown to be partial discharge free up to 50 kV.

3.7 Imaging system

To record images of the bubble shape and dynamics, a suitable camera, optics and light source have been selected to permit the relatively fast events to be captured for off-line signal processing and analysis. Initial trials were performed to image bubble nucleation and dynamics using a digital Kodak 4540 CCD camera capable of a highest frame rate of 40,500 fps. This demonstrated that in order to capture thermal bubble nucleation and pinch-off a camera frame rate in excess of 5000 fps would be required. In addition initial trials demonstrated the requirement for a fast shutter speed to avoid motion blur on images due to the very fast motion of the bubble surface oscillation. This issue becomes more critical with the faster motion of the vapour bubbles produced from discharge events in liquid nitrogen density change streamers.

The requirement for a very fast shutter speed has the consequence that a light source with high intensity is necessary to illuminate the subject sufficiently. Selection of a light source capable of stroboscopic firing means that the light source can also be used to control the effective shutter speed of image capture. To perform this function with sufficient light intensity a class four LS20-50 copper vapour laser was chosen, this was supplied by Oxford Lasers Ltd. The laser can fire stroboscopically at repetition rates up to 50 kHz. This copper-vapour laser is unique, supplying 20W of power with light pulses of a 25-30 ns pulse width. In addition this laser is capable of pulse on demand, allowing master-slave synchronisation with a camera. The sequence of operation when coupled to the camera involves the camera shutter opening, the laser firing a pulse of light illuminating the subject under study for a nominal 30 ns and then the camera shutter closing. This virtually eliminates motion blur on images of bubbles during nucleation and pinch-off. Crisp edges of density change streamers can also been seen, although the fast motion of resulting bubbles means that even with this pulse time some motion blur results. The laser has a fibre optic connection to a light diffuser lens allowing the light output to be positioned at any of the optical ports and angled with ease. The wavelengths of this laser are

510.6 nm, green, and 578.2 nm, yellow, both in the visible and suitable for use with the window selections for the cryostat optical ports.

The camera selected is an HG100K supplied by Lake Image Systems Ltd. The HG100K has a CMOS sensor array of 1504 by 1128 pixels at maximum resolution. The maximum frame rate of this camera is 100,000 fps. Selectable rates and resolutions are shown in Table 3.1.

Table 3.1, Frame rates and resolutions of the HG100K Camera

Frames per second	**4:3**	**1:1**	**3:1**
≤1,000	1504x1128	1120x1120	1504x584
2,000	1056x792	896x896	1504x488
3,000	832x632	704x704	1312x432
5,000	640x480	544x544	992x328
10,000	416x320	352x352	672x216
20,000	256x192	224x224	416x136
30,000	192x152	160x160	320x104
50,000	96x72	96x96	192x64
100,000	32x24		64x24

Digital image capture was chosen over photographic film cameras to allow off-line signal processing. This has provided the ability to automate the extraction of dimensional and velocity data from sequences of recorded bubble nucleation events.

Two lenses have been selected covering two ranges of magnification and working distance. The first a Nikon Micro-Nikkor 55 mm provides working distances from 250 mm to infinity and corresponding magnification from 0.5x to 0.1x respectively. This lens has an internal iris with f-stop settings from f/2.8 to f/32 allowing the illumination intensity to be controlled with ease at the lens.

The second lens is a Questar QM100 long distance microscope lens designed for working distances between 150 mm and 355 mm. This working distance covers the full width of the cryostat inner vessel accounting for the 50 mm radial vacuum gap between the inner sapphire and outer BK7 windows. The QM100 has a focus knob on the back plate and this provides greater precision the closer the working distance. Magnification can be selected by the choice of configuration, the number of extension tubes between the lens and the camera mount, and can be further increased

by use of an additional 2x Barlow lens. The magnifying negative Barlow lens is placed directly behind the QM100 lens; this is coupled to the camera by sufficient extension tubes to give the desired field of view (FOV) and magnification. Increasing the combined length of the extension tubes will result in greater magnification. Changing the working distance can also be used as a means to adjust magnification.

The QM100 is distinguished from other lenses by its magnification at large working distances and its low diffraction, i.e. there is minimal distortion from the centre to the edge of the camera sensor. The QM100 has no internal iris and provides excellent magnification at the expense of a shallow depth of field. For illustration; with a 16.9 mm camera sensor and a working distance of 250 mm it is possible to achieve magnifications between 0.9x to 3.0x, with corresponding FOV of 1.8 and 0.57 mm respectively, the depth of view is approximately 100 μm. In contrast the use of the Micro-Nikkor 55mm lens is limited not by its FOV, but by the dimensions and angle of view afforded by the cryostat optical ports.

3.8 Summary

A liquid nitrogen cryostat to facilitate characterisation of nitrogen as a liquid dielectric has been designed, manufactured and safety tested. The designed cryostat allows experimental investigation into conditions causing bubble nucleation as well as the study of bubble dynamics, pre-breakdown and breakdown phenomena in liquid nitrogen with applied electric fields. The design brief was for a cryostat to facilitate study of the behaviour of nitrogen across the temperature range for the liquid state, for variable pressure and with samples electrically stressed with applied voltages representative of power apparatus prototypes in development. The initial brief was met by careful design to allow temperature control in the cryostat to within ±1 K for liquid nitrogen at temperatures between 64 and 125 K. Temperature is maintained without sacrificial loss of liquid nitrogen by incorporating a cryo-cooler into the guard vacuum jacket between inner and outer vessels. The inner vessel has been designed to allow operation at elevated pressures up to 2 MPa, the cryostat has been certified for this working pressure following design, manufacture and testing to national pressure vessel standards. In addition a high voltage bushing to operate at cryogenic temperature and elevated pressure has been designed and fitted, supplying

voltages up to 80 kVrms. This arrangement is pd free for applied voltages up to 50 kVrms. Optical ports incorporated into the vessel at strategic locations around the circumference permit the use of lighting and imaging techniques for the study of dielectric phenomena in liquid nitrogen. For this purpose a digital camera, lenses and laser light source have been assembled to capture images of high speed events up to frame rates of 50,000 fps. The digital image capture provides optical measurements that can be extracted by signal processing techniques facilitating the study of bubble dynamics and pre-discharge phenomena.

Chapter Four

Thermally induced bubbles in a uniform electric field

4.1 Introduction

It is well known that the application of electric fields to fluids can have effect on the heat transfer both in single-phase and two-phase systems [75]. This results from what is termed electrohydrodynamic effects (EHD). It has been shown that the application of an applied electric field has an effect on the heat transfer characteristics of boiling for polar and non-polar liquids; and heat flux enhancement by EHD in pool boiling has been studied [75-81]. This is characterised by a shift in the boiling curve resulting in greater heat fluxes at lower wall superheats; an increase in the critical heat flux (CHF) and a reduction in the onset of nucleate boiling (ONB) with an associated disappearance or smaller hysteresis at the point of the ONB [82].

Experimental studies have shown that with the application of an electric field, for the non-polar fluid of liquid nitrogen, there is a delay in the ONB and higher CHF for heat flux controlled experiments [83, 84]. Hence the generation of bubbles in applied electric fields is of interest to further the understanding of

electrohydrodynamic effects in operation during the nucleate boiling regime and also the possible effect on the use of liquid nitrogen as a dielectric fluid.

Typically, researchers studying the dynamics of lone bubbles in the presence of electric fields have studied bubbles emanating from a single site by piping gas into the liquid at a known volumetric flow rate. This approach has the advantage of producing a gas bubble with a known volumetric growth rate and without the additional complications of thermal convection as is the case for thermally generated nucleate boiling. However applying findings to a real boiling scenario may prove difficult due to the influence of these factors in application.

The liquid nitrogen cryostat described in Chapter 3 has been used to conduct experiments to investigate the dynamics of thermally generated bubbles within an electric field. Bubbles have been thermally generated by embedding heat sources in electrodes. The study used a high speed camera to image the bubbles during growth and pinch-off. In addition to characterising the bubble nucleation frequency, signal processing has been employed to extract dimensional data from the bubbles at the point of departure allowing calculation of the bubble volume and aspect ratio. For the experiments described an electrode has been constructed with an embedded heat source and a re-entrant cavity. The sample arrangement, experimental apparatus and image processing are detailed in the following sections. Experimental observations and quantitative results are then presented and discussed.

4.2 Electrohydrodynamic theory

The enhancement of heat transfer is due to the action of electrohydrodynamic forces acting within the volume of the fluid. The forces acting within a dielectric fluid are given by the theoretical equation;

$$Fv = q_f E - \frac{1}{2}E^2\nabla\varepsilon + \frac{1}{2}E^2\nabla\left(\rho\frac{\partial\varepsilon}{\partial\rho}E^2\right) \qquad (4.1)$$

Where q_f is the free charge density, E is the electric field strength, ε is permittivity and ρ is density. This equation arises from the consideration of the energy of a dielectric fluid undergoing deformation and was first proposed by Korteweg and

developed by Helmholtz [85]. The first term of this equation arises due to free charges present within the fluid, these charges experience a force in an externally applied field, the Coulomb force of electrostatic attraction; this is also called electrophoresis where is refers to the force acting on a charged body within a fluid. The second term is the dielectrophoretic force, this occurs with the appearance of polarisation of fluid molecules with the application of the electric field and due to the non-uniformity of the applied electric field. The third term is the electrostrictive force, a deformation of the fluid arising as a result of the gradient in the fluid density, and the permittivity change with a change in density, and due to non-uniformity of the electric field.

In two-phase systems such as the case for nucleate boiling the dielectrophoretic force occurs predominantly at the bubble wall, the liquid-vapour interface where there is a large gradient in the permittivity. Dielectrophoretic force is defined by Pohl [86] as "the motion of matter caused by polarization effects in a non-uniform electric field". Any dipole induced by the application of the external field will be aligned with the field. The dipole in a non-uniform field will experience a difference in the electrostatic attraction of one end and the repulsion at the other end, thus a net force will arise. This is true for a dielectric body in a fluid with a different permittivity to that of the fluid. The dielectric with the greater permittivity will be attracted to the region of highest field strength, positive dielectrophoresis. The dielectric with the lower permittivity will be attracted to the region of lower electric field strength, negative dielectrophoresis. It is clear from this understanding that the direction of travel will remain the same if the direction of the field is reversed.

For the case of a gas bubble within a liquid the gas will have a lower permittivity than the liquid and dielectrophoretic forces will act on the bubble wall. The resulting stress will act towards the regions of lowest electrical field strength. Bubble motion and deformation in a field will in addition to electrostatic forces be dependant on the growth rate of the bubble and on the governing momentum and energy equations of the fluid and resulting fluid-flow.

Electrophoretic force is distinct from dielectrophoretic force as it acts on charged particles. The action of electrophoretic force may therefore be experimentally

distinguished from dielectrophoretic action for motion within ac fields since the direction of motion will be dependant on the direction of the applied field. Electrophoresis can occur within uniform fields, for dielectrophoresis to occur there must be a field divergence. However in the case of a two-phase system the shape of the bubbles present within the fluid may have a significant influence on the divergence of the local electric field even within a uniform electrode system, leading to dielectrophoretic forces.

The third term of Equation 4.1 is the electrostrictive force, Stratton defines electrictriction as "the elastic deformation of a dielectric under the forces exerted by an electrostatic force" [85]. For the bubble in the dielectric liquid it acts at the liquid-vapour interface, the bubble wall, as a pressure acting radially inward. This electrostrictive term can be simplified for the case of liquids and gases for which the Clausius-Mossotti law is a good approximation;

$$\rho\frac{\partial\varepsilon}{\partial\rho}=\frac{\varepsilon_0(\varepsilon_r-1)(\varepsilon_r+2)}{3} \tag{4.2}$$

Where ε_0 is the permittivity of free space, ε_r is relative permittivity of the liquid, and the relative permittivity of the gas is assumed to equal 1. Substituting Equation 4.2 into Equation 4.1 leads to;

$$Fv=q_fE-\frac{1}{2}E^2\nabla\varepsilon+\frac{1}{6}E^2\nabla\left(\varepsilon_0(\varepsilon_r-1)(\varepsilon_r+2)E^2\right) \tag{4.3}$$

Heating a fluid causes thermal gradients and resulting gradient in the dielectric permittivity which will result in the action of dielectrophoretic and electrostrictive forces as discussed. It is seen from Equation 4.3 that electrophoretic force will only act if there are free charges within the volume of the dielectric fluid. Thermal gradients within the fluid will however cause gradients in the electrical conductivity of a fluid and this will result in build-up of free charge within the volume which can then be acted on by the external field. Experimental workers have used the concept of the fluids charge relaxation time to asses the significance of this effect.

By considering that there can be no permanent distribution of free charge in a fluid where the conductivity is non-zero and using the simplified model for conduction of ohms law for a homogeneous media. Such that the relations between **D** and **E** and **J** and **E** are linear; it is possible to show that for an electrostatic system this leads to an expression for charge density at any instant in time, λ [85];

$$\lambda = \lambda_0 e^{-\frac{\sigma}{\varepsilon}t} \tag{4.4}$$

Where λ_0 is initial charge density and σ is electrical conductivity. This provides the charge relaxation time, τ, a characteristic constant of the fluid;

$$\tau = \frac{\varepsilon}{\sigma} \tag{4.5}$$

This is the time it takes for the charge at a point in the fluid to decay to 1/e of its initial value.

Despite the simplicity of this approach it has been found to be useful to interpret experimentally obtained results. It has been seen that for single-phase systems the electrophoretic force becomes significant if the relaxation time is of the same order or less than the time for the fluid to transverse the electric field [87]. For two-phase systems the electrophoretic force is important where the relaxation time is of the same order or less than the period of the characteristic dynamic time of a process, t_d. For example the period of the imposed electric field [80], the oscillations of a bubble interface [81], or the detachment period of bubbles [88]. Thus a liquid can be considered as a perfect insulator if the dynamic time of a process is less than the charge relaxation time ($t_d < \tau$) or conducting if it is greater ($t_d > \tau$). In the case of a bubble, for the insulating liquid there will be no appearance of charge on the liquid-vapour interface and the field will be distributed throughout the liquid and vapour. For the conducting liquid the total voltage drop will occur at the interface where the free charges occur.

4.3 Bubble growth dynamics

The first experiment was designed to examine the growth dynamics of thermally induced bubble nucleation. Conventionally it is understood that bubble nucleation will occur from active cavities, i.e. cavities which have trapped vapour during filling, or due to previous bubble nucleation. It is also anticipated from theoretical considerations that as the heat flux increases, once an initial site becomes active, bubble nucleation will occur from more than one site on a heated surface. In order to control the location of the nucleation site an artificial cavity has been used. This ensures the heated surface has a preferential location for nucleation, and this site has been placed within the centre of an applied near-uniform electric field. Controlling the nucleation site also makes the use of a high magnification lens practicable.

4.3.1 Heated electrode construction

For the initial experiment a circular plane electrode was designed, Figure 4.1. The electrode has a 28 mm diameter flat top surface and a rounded edge periphery with a radius of 3 mm. The electrode is made from two stainless steel parts. Stainless steel is used as it is mechanically stable over the temperature range of operation and will not suffer significant corrosion, minimising variability from one experiment to another. The electrode incorporates a 150 W cartridge heater located under the top surface and beneath an artificial cavity. The heater is a sliding fit into a copper sleeve for greater thermal conduction from the full length of the heater to the top face. The end of the copper sleeve is soldered to the back of the stainless steel face which has been machined to a thickness of 0.5 mm. With the cartridge heater mounted into the copper with thermal conducting paste the two stainless steel parts are joined. The join is 10mm from the top surface and is soldered around the outside along a V-shape resulting from chamfered edges machined on the two parts coming together. Eccobond 286 a thermally insulating resin, with thermal conductivity of 1.0 W m^{-1} K^{-1} and linear thermal expansion coefficient of $36x10^{-6}$ K^{-1}, is injected to fill the open space in the back of the electrode reducing conduction in any direction but toward the artificial cavity.

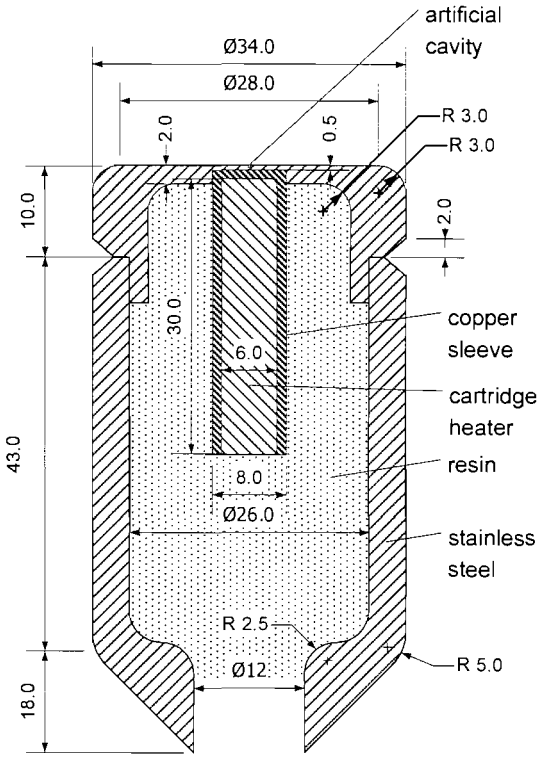

Figure 4.1, Cross section of electrode with embedded cartridge heater

The artificial cavity is re-entrant and was achieved by first drilling a 250 μm diameter blind hole into the centre of the top face. The edge of the drilled hole was swaged in toward the cavity to partially close the hole near the top face by pressing with a ball bearing, resulting in a 200 μm diameter opening. The top face and body of the electrode were polished to a mirror finish to remove any defects that might perform as bubble nucleation sites. The effect is to create a preferential nucleation site that becomes active before others on the electrode surface. This allowed the study of nucleation occurring at a single designed location, eliminating difficulties with bubbles from other nucleation sites directly interfering or blocking the view of the nucleating bubbles under study.

4.3.2 Experimental arrangement

The electrode described was mounted within the cryostat as part of the sample arrangement shown in Figure 4.2. With reference to Figure 4.2, the arrangement consists of a high voltage electrode (1) made from stainless steel with a diameter of 120 mm, suspended from the high voltage conductor of the voltalit bushing (2). Below this with a parallel 30 mm gap is positioned the bottom stainless steel earth

electrode with incorporated heat source and artificial cavity (3), attached to the fill line of the cryostat (4). Both electrodes have surfaces polished to a mirror finish to provide a near uniform field on the centre line. The edges are radiused to reduce electric field edge effects.

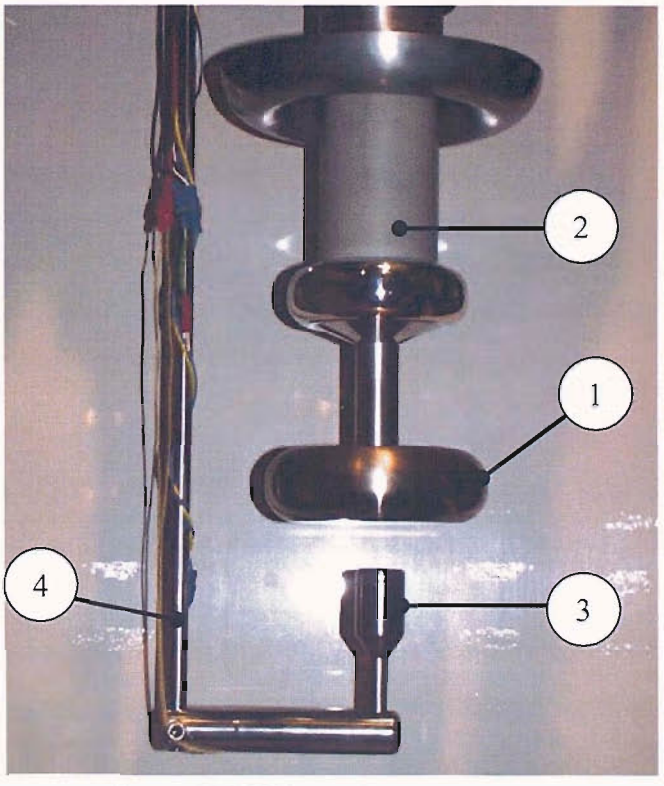

Figure 4.2, Electrode arrangement

Special care is taken in the mounting of the sample, all surfaces of the mounting arm are polished to eliminate other bubble nucleation sites that will interfere with the imaging; or cause convection currents around the bubble of interest.

4.3.3 Electric field plotting

The electrode geometry described has been modelled using a finite element analysis (FEA) package to plot the equipotentials of an applied electric field, Figure 4.3 and Figure 4.4 show typical results obtained.

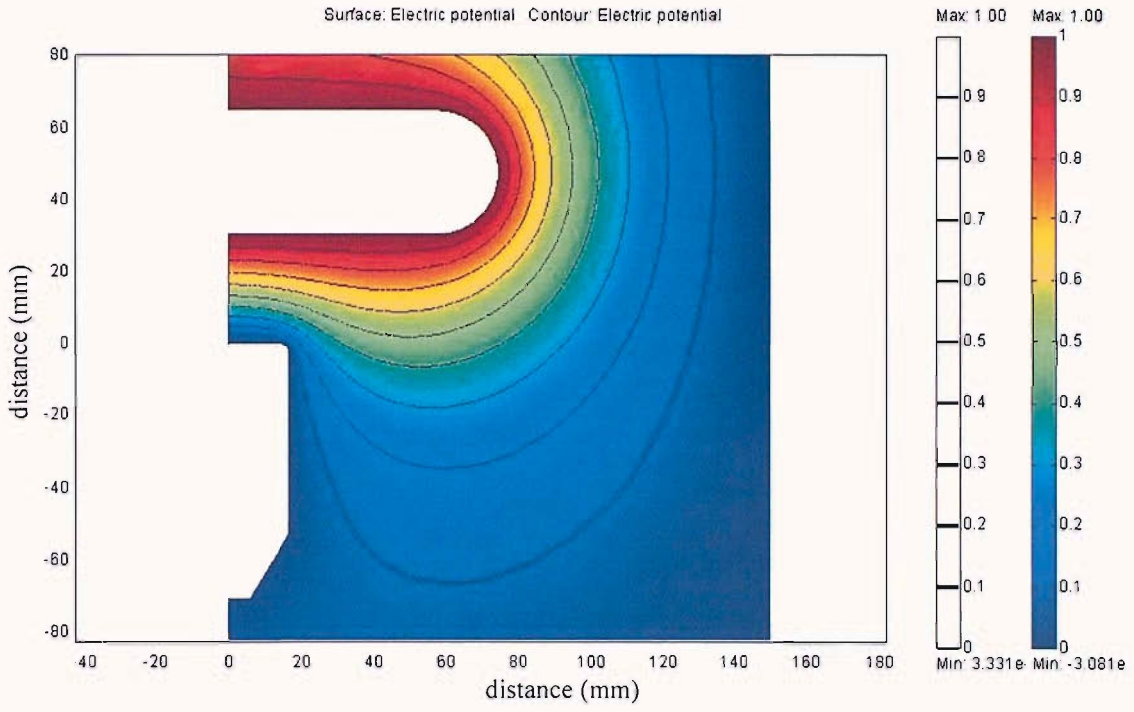

Figure 4.3, Axi-symmetric surface plot, continuous plot of potentials, with 10 equipotential contour steps, per unit values

To minimise computational effort the FEA model is built to take account of the symmetry of the electrode arrangement. A simple two-dimensional slice is taken through the centre line of the electrodes arrangement and half is drawn into the FEA package. The details of the axis for 360 degree axi-symmetric rotation are programmed into the model before solving. An inner refined meshed zone is constructed inside a larger coarsely meshed zone which extends to the earthed cryostat wall. This ensures the model resolves the local field sufficiently in the regions of interest, i.e. between the electrode surfaces, and does not distort the field at the edge of the modelled region. For the axi-symmetric model of plots Figure 4.3 and Figure 4.4, the axis of symmetry is the left hand edge. A potential of 1 per unit (p.u.) has been applied as a boundary condition on the top HV electrode, and 0 p.u. on the bottom grounded electrode. The surface colours of Figure 4.3 represent a continuous gradient between 0 and 1 p.u. Thus potential can be found at any location by multiplying the p.u. result by the magnitude of the voltage applied to the HV electrode. Figure 4.4 shows a close-up view of the electrode gap equipotentials and electric field strength.

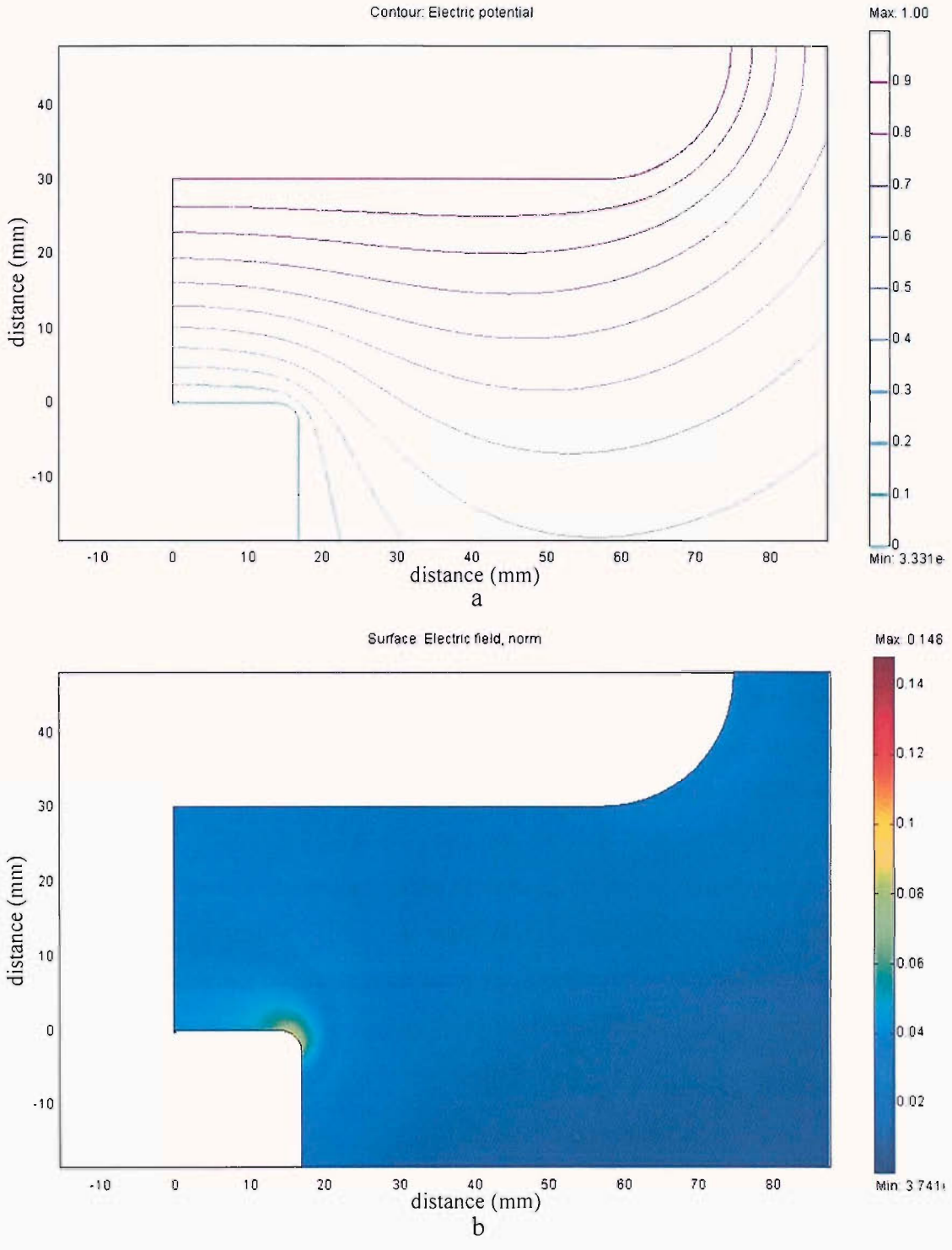

Figure 4.4, Axi-symmetric plots close-up of the electrode gap; a) 10 equipotential contours, b) electric field strength (p.u. mm^{-1})

The maximum electric field strength on the outer corner edge of the bottom electrode is 0.071 p.u. mm^{-1}, located at coordinates x = 17, y = 0, Figure 4.4(b).

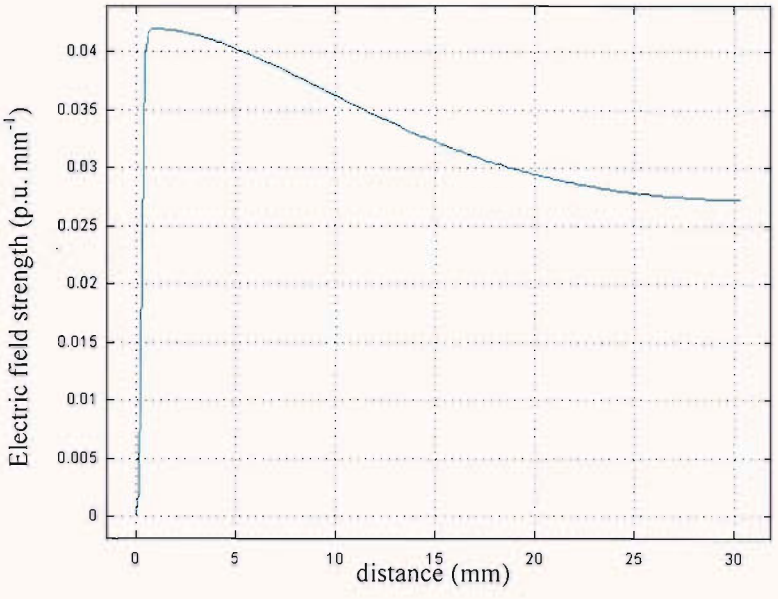

Figure 4.5, Electric field strength along the central axis, bottom to top.

Figure 4.5 details the electric field strength along the central axis of the electrode gap; between electrodes and running from the bottom of the cavity, in the bottom earthed electrode, and up into the gap to the HV electrode. It is seen that once out of the cavity the field strength across the electrode gap, varies from 0.042 p.u. mm^{-1} to 0.027 p.u. mm^{-1}. Figure 4.4(b) also shows that the field does not vary appreciably off the centre line until the corner of the bottom electrode, where the stress is raised by the corner edge profile. Thus it is concluded that the field within the central region of the electrode gap is near uniform for a homogeneous media within the gap, i.e. before the application of a thermal field producing density or permittivity gradients by convection and bubble nucleation.

The lower heated electrode has a diameter of 34 mm, significantly larger than the cavity size and the bubbles resulting from heating the cavity are typically less than 2 mm in diameter. Thus it may be initially assumed that the influence of edge effect, seen in Figure 4.4(b), is not directly effecting the bubble nucleation and growth occurring within the electric field profile on the central axis of the electrodes.

The cavity hole has a modelled diameter of 250 μm the same as the drilled hole before pressing. There is a difficulty with FEA modelling of the electric field strength at sharp edges such as the right angle at the top lip of the cavity mouth. In

this region the mesh would require refinement to approach infinitely small inter-node steps around the corner to calculate the field strength at this point correctly. The calculated value at this point is therefore a function of the mesh refinement at this location rather than the sharp edge drawn. This is not without use however since the true profile is in reality only an approximation to the drawing. As discussed the real sample edge is further rolled into the cavity to create a re-entrant cavity. As seen later in this Chapter the bubble will itself modify the field becoming the region of interest above the cavity mouth.

4.3.4 Bubble dynamics studies: experimental method

The sample arrangement was placed within the cryostat which was then evacuated to below 10^{-4} Torr, to remove any water vapour, prior to filling with commercial grade oxygen free LN_2. The test chamber containing the sample electrodes and liquid nitrogen are then sub-cooled to suppress boiling. The liquid nitrogen temperature was held at 76.6±0.5 K for the measurements made during this experiment.

With the sample situated in the centre of the cryostat the nucleating bubbles were backlit with a spot lamp and digital images captured on a digital camera through the optical port in line with, but on the opposite side of the cryostat. An iris closed to a diameter of approximately 2 mm diameter was placed between the lamp and the optical port to provide a more "point source" like illumination of the bubble being imaged, this reduces penumbra around the object when imaged. A simple spot lamp gave sufficiently clear images for these initial results. Little motion blur was recorded due to the slow bubble lift-off. It was therefore possible to extract data by digital image processing techniques for the parameters under investigation.

The embedded heat source in the bottom electrode was set to provide a measured input power, for the positive dc results for example 268.8 mW was selected. At this power nucleating bubbles in the sub-cooled liquid rise from the cavity and reach the top electrode and coalesce before rolling up around the edge of the HV electrode without condensing back to the liquid state. Using the QM100 microscope lens sequences of magnified images of nucleating bubbles were captured for multiple nucleation events including bubble detachment. The camera used for initial results was a Kodak4540. This was used to collect a full resolution image of 256 by 256

pixels at 4500 fps. Sequences of a maximum of 3072 images were captured equal to 683 μs of real time. The resolution and magnification of the images has been calibrated using a resolution test target. The pixel width of known line pairs per millimetre allow the spatial resolution of images captured with the same magnification and focus to be found. With the pixel and frame size calibrated it follows that the imaged bubble dimensions can be calculated. For the following tests the magnification and resolution is held constant. The 256 by 256 pixel frame size is 1.6 mm by 1.6 mm and the corresponding pixel size is 6.25 μm by 6.25 μm.

4.3.5 Image processing

An image of a bubble taken with this experimental method is shown in Figure 4.6(a) below. This image, with ice particulate on the electrode surface, has been selected to demonstrate the applied filtering technique. Image processing has been developed to gain height, width and volume data from these images. The first stage is to distinguish which parts of the raw image are bubble and what is the electrode or background shadows. This is achieved by thresholding. The original image is in 256 level greyscale, a threshold level of greyscale, for this example the value of 80, is selected and every pixel above this value is converted to white and everything below to black. To do this successfully a histogram of greyscale levels in the original image can be plotted to indicate where the threshold should be set. The output is then checked against the original to ensure no dimensional information is lost, i.e. that the white shadow of the bubble in the binary image is of the same size and shape as the original. With experimentation and consideration of the greyscale histogram a threshold value can be set to successfully divide the bubble from its background. The result can be displayed as a black and white image with the bubble in white on a black background, Figure 4.6(b).

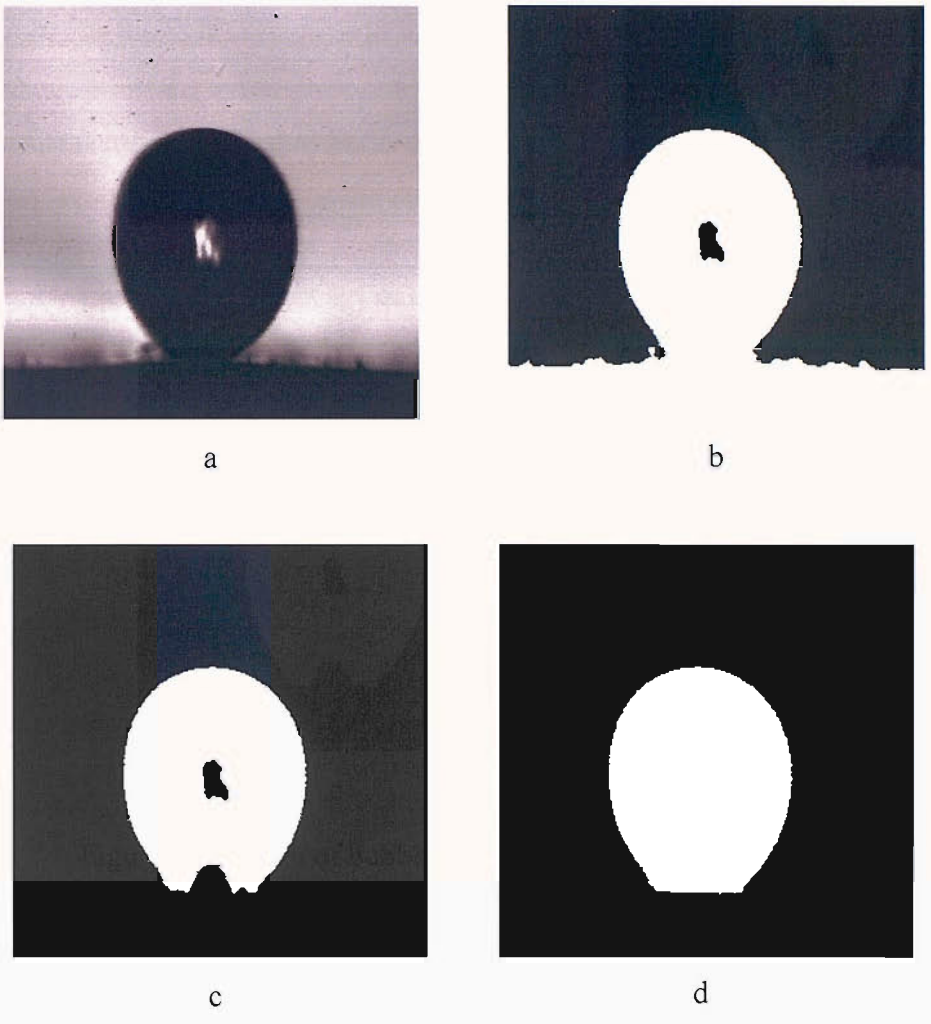

Figure 4.6, Image of bubble at point of detachment a) original, b) binary conversion by thresholding, c) threshold minus dirt, d) output image for calculation

Following binary conversion the next task is to remove the base electrode and any particles present on the optics. Successive images will have particles on them in the same place and the electrode will not move appreciably from one image to the next this observation is used to recognise these stationary features. A program reads in a sequence of images with the bubble in different locations to that in the original image, e.g. images as the bubble lifts away from the surface and moves up through the frame. An accumulator space is built from the sequence, the accumulator scores a point for every white pixel. As the images are read the places in the picture where there is repeated activity, i.e. particles or a stationary object, accumulates in value. The areas that score highly in the accumulator space are particulate or the electrode at the base of the image. Subtracting these areas from the threshold image of the

original, results in a cleaner image as shown in Figure 4.6(c). At this stage the image still contains the light reflection in the centre of the bubble and the filter has removed the "shadow" of the subsequent nucleating bubble in the sequence which has also been mistakenly classified as particulate by the accumulator space filter. These regions are simply filled since the desired shape is known to be flat bottomed and this results in the output image of Figure 4.6(d).

4.3.6 Positive dc results

The embedded heat source in the bottom electrode was set to provide a measured input power of 268.8 mW and a positive dc voltage was used as the working parameter. Positive dc voltage was applied to the high voltage electrode at the following levels; 0, 20, 40, 60 and 80 kV dc. The shape of the bubbles within the liquid nitrogen gap is near spherical for no applied voltage. For applied dc voltage it is observed that the bubble elongates in the direction of the applied field, Figure 4.7. The bubble also achieves a greater volume before detachment.

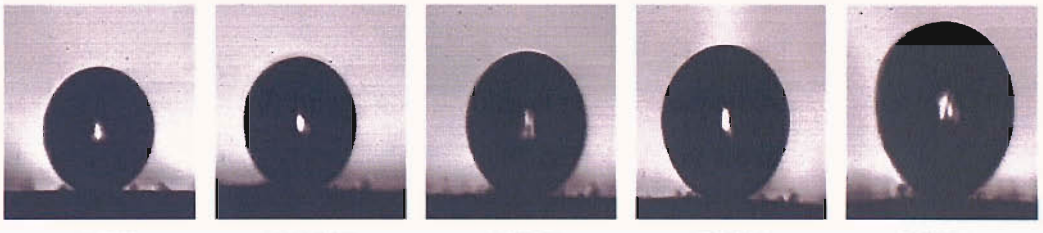

0kV 20kV 40kV 60kV 80kV

Figure 4.7, Images of bubbles at point of departure, captured at 4500fps, frame size is 1.6 mm by 1.6 mm

From the output images obtained using the experiment and using the data extraction techniques described it was possible to obtain cross sectional area, volume and aspect ratio data. Cross sectional area is found as the sum of white pixels and the greatest string of horizontal and vertical pixels yields width and height respectively. It has been assumed that the bubble is symmetric about its central vertical axis. This allowed volume to be calculated as the sum of circular disks of diameter equal to the width of the bubble for every pixel level, from the top to the bottom of the bubble image.

It can be seen from Figure 4.8 that as the applied voltage is increased the bubble departure frequency reduces with a near linear relationship and that bubble volume increases as a second order polynomial function of the applied voltage. In addition the aspect ratio, the ratio of height to width increases with increasing applied voltage. It can be concluded that an increasing applied voltage causes the elongation of bubbles in the direction of the applied field. The applied field causes the bubble to remain attached to the electrode for a longer period. Since the heater power is constant this allows more time for the bubble to accumulate vapour by evaporation, resulting as seen in Figure 4.8(b) in the larger volume per bubble at the time of detachment.

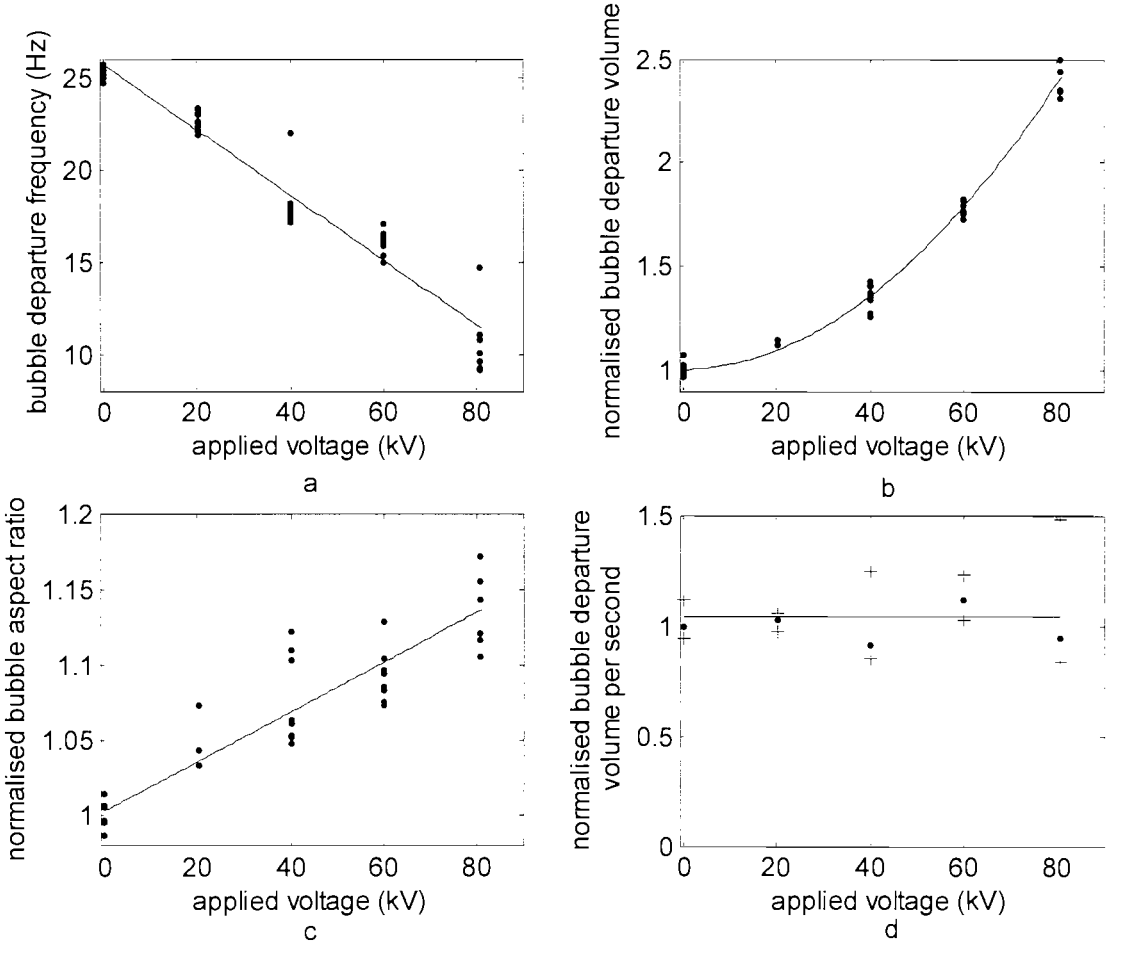

Figure 4.8, Plots of bubble detachment data against applied positive dc voltage, a) bubble departure frequency, b) normalised departure volume, c) normalised bubble aspect ratio, d) normalised volume per second

Figure 4.8(d) is a plot of the normalised product of volume and bubble departure frequency, the crosses marked represent the data range limits and are wider at 40 kV

and 80 kV due to the larger spread in frequency data for these voltages, the potential causes of this spread in the data are discussed later. The limits are narrower at 20 kV where limited volume data was obtained due to difficulty in data extraction. It can be concluded that overall the volume of vapour carried away by the bubbles per unit time appears to remain reasonably constant.

4.3.7 AC results

In an ac field at 50 Hz for the same electrode geometry, bubbles have been nucleated with the heater set at 272 mW. The bubble was found to oscillate in phase with the applied electric field at 100 Hz. The bubble was elongated for each half cycle, both positive and negative polarity, returning to near spherical as the voltage reduced through the zero crossing points of the waveform. This oscillation was clearly seen for the applied voltages with peaks of 85.02 kV, 70.94 kV, 56.68 kV and 42.79 kV, below this, i.e. at levels of 28.52 kV, 14.14 kV and 0kV it was difficult to observe any discernable deflections and so the frequency of oscillation has not been measured for these voltage levels. It is plain from the oscillations seen at higher voltage levels that there is a force being applied to the bubble that causes it to elongate in the direction of and due to the applied electric field.

The bubble departure frequency at zero applied volts differs from the experimental result recorded for the dc case. This is due to a variation of the bulk liquid temperature at the surface of the heated electrode, this being greater for the ac case. This leads to larger relative departure volume and lower departure frequency. It has been observed that the ac results contain greater variation in bubble departure period and therefore departure volume due to the 100 Hz mechanical oscillations which are not synchronised to the bubble detachment frequency. Results have therefore been collected as a mean period for several bubble detachments and are plotted in Figure 4.9. Data set size ranges from 7 to 12 periods. Even with the variability in the data it is apparent from Figure 4.9(a) that there is a trend for the bubble departure frequency to reduce with an increase in the applied potential. This in turn leads to a reduction in the normalised volume of vapour generated per second Figure 4.9(c).

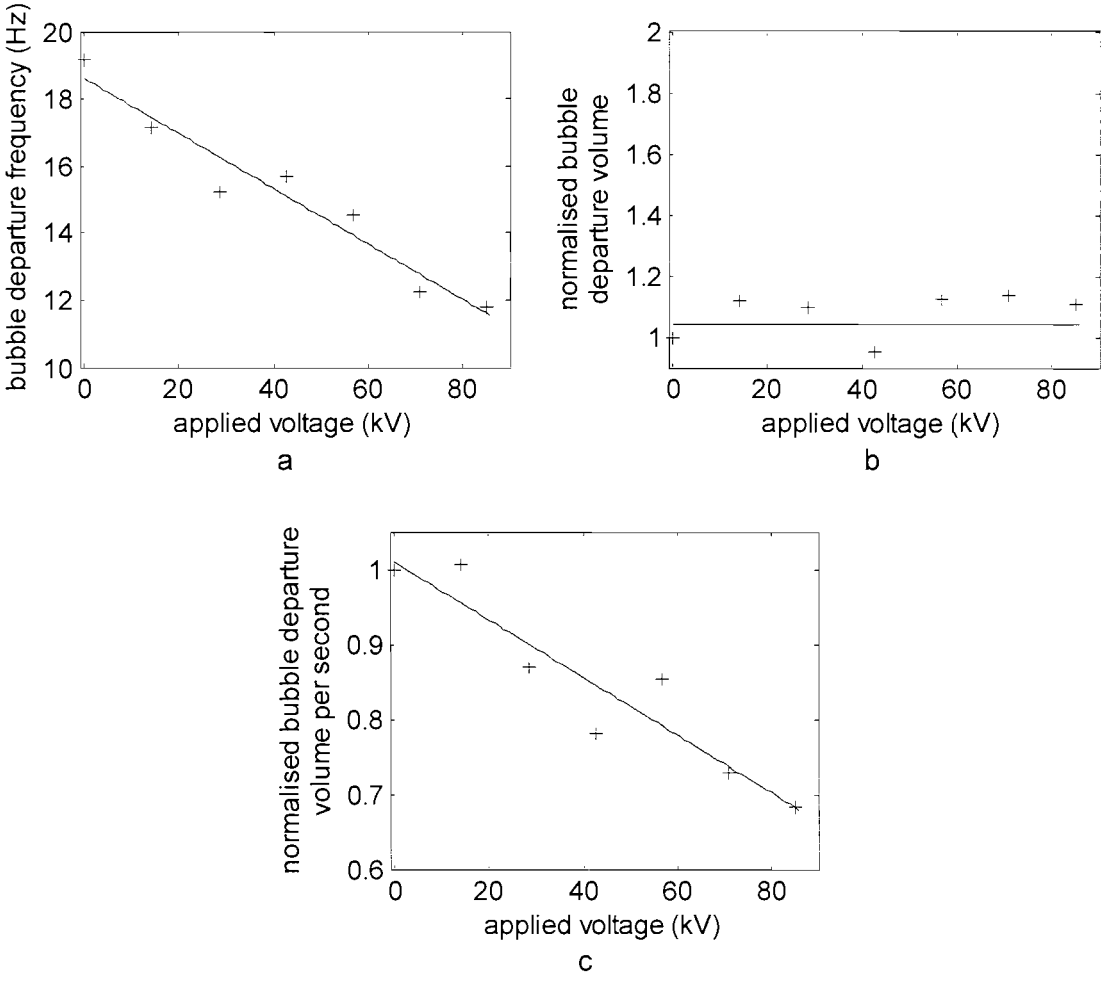

Figure 4.9, Plots of bubble detachment data against peak applied ac voltage,
a) bubble departure frequency, b) normalised departure volume,
c) normalised volume per second

4.3.8 Discussion – EHD forces

When compared to the results presented by other authors the distinctiveness of this experiment is highlighted. Kweon, Kim, Cho and Kang [89] investigated the electric field effects on bubbles in an isothermal system of piped gas into room temperature refrigerant, cyclohexane (C_6H_{12}). The motivation of this study was to examine the response of vapour/liquid interfaces within electric fields without the additional complications of a thermal field; and to demonstrate that the electric field has significant influence in the enhancement of boiling heat transfer. In this experiment the normalised departure volume of bubbles showed a small increase to an increase in electric field strength for the near-uniform field case. The increase in electric field strength was achieved by increasing voltages at various stages up to 24 kV for four

electrode spacings of 46, 32, 21 and 16 mm. It is difficult to obtain values from the plotted graph results presented, due to the scale, but approximate values have been obtained see Table 4.1. By assuming equivalence between the two experiments in electric field strength for a uniform gap without a bubble present (i.e. dividing the voltage by the electrode spacing) comparisons are made possible, Table 4.1. Both experiments show an increase in the normalised bubble volume with an increase in electric field strength. The response of normalised departure volume to the electric field strength for the dc experiment in LN_2 of this study is markedly greater than for that of the isothermal case in cyclohexane reported.

Table 4.1, Comparison of normalised volume results

Electric field strength ($kV\ mm^{-1}$)	Normalised departure volume in C_6H_{12} ref.[89]	Normalised departure volume in LN_2 [Figure 4.8]
1.143	1.04	1.26
1.5	1.06	1.44

The effect of applying an electric field on the bubble size by thermal nucleation has also been studied by those examining the electrohydrodynamics (EHD) effect on boiling. It has been widely reported that an increase in the electric field strength will result in a decrease in size and volume of bubbles departing a heated surface [77-79, 82]. However it should be noted that an important distinction must be drawn between the case of boiling in uniform and non-uniform fields, most studies to date have been performed in non-uniform fields. Indeed in the same study of piped air into cyclohexane mentioned it has been shown that for the case of the single bubble placed now in a non-uniform field, volume decreases with the application of the electric field [89].

Another distinction that may be significant is that between the case for single bubbles produced at a single nucleation site and the case where there are multiple nucleation sites in the nucleate boiling regime. As discussed in Chapter Two the occurrence of multiple sites would normally occur with any increase in heat flux after the onset of nucleate boiling (ONB). This can be controlled, limiting nucleation to a single site by careful design of the experimental sample. By providing a preferential site as in the experimental arrangement of this study a single thermal bubble nucleation site

can be achieved. With no applied electric field columns of bubbles from different sites on a heated surface will begin to interact with each other as heat flux is increased, and above the critical heat flux (CHF) film boiling will occur. Experimental results from studies of boiling on plate surfaces in an electric field show that the electric field significantly influences the Rayleigh-Taylor instability of the bubble and adjacent fluid columns. This behaviour in electric fields has been theoretically understood by considering the influence of the electric field on the surface wave model for pool boiling from plate surfaces originally proposed by Zuber [80, 81, 90].

Theoretical analyses have focused on the effect of the electric field on single bubbles, believing that the behaviour of the single bubble influences the heat transfer process [77, 78, 82, 89, 91-93]. In a theoretical study to model the dielectrophoretic force on the departure shape and size of bubbles in uniform fields it was predicted that the electric field would cause a decrease in bubble departure size with increasing electric field strength [91]. The model assumes that the tip radius at the top of the bubble can be used to obtain an estimate of the dielectrophoretic force acting on the top surface of the bubble. To do this the force resulting on a spherical bubble model is calculated for the equivalent radius and this result is then applied to the case of the bubble elongated in the electric field to provide a new aspect ratio, which is increased due to the force acting on the top surface. Assuming as this model does, the electric field does not effect the surface tension or the contact angle of the bubble at the solid wall; the bubble is elongated in the direction of the field. From this a new bubble wall shape can be calculated and the size at pinch-off calculated. The elongation of the shape in the field direction, normal to the wall, causes the bubble to pinch-off earlier than without the applied field, resulting in smaller volumes than for the no applied field case.

This model suffers from the difficulty that the assumptions that the surface tension and the contact angle will remain constant can be challenged. It is known that the surface tension will change with the application of the electric field. This is clear from electrocapillary theory; where for example liquid is drawn up between two electrodes by the application of a potential difference between them. This is known to be a result of the electrostriction effect. Challenging this assumption also makes

the second, that of no change to the contact angle untenable. Indeed it has been shown that even without the action of electrostriction the contact angle will change as a bubble on a wall is elongated in the direction of the applied field. This also leads to the result of a change in the surface tension since the contact radius becomes larger [92].

In a recent study by Cho, Kang, Kweon and Kim a numerical approach was taken to solve the shape of the bubble growth in an electric field [92]. This model shows some improvement over the analytical one. In the analytical model of Cheng and Chaddock the bubble shape is calculated before consideration of the influence of EHD, in the numerical model it is calculated with respect to the influence of EHD effects. The numerical model is limited to shape calculated for a fixed volume and predictions for aspect ratio and contact angle were in better agreement with experimental results obtained for an air bubble in cyclohexane than the analytical model of Cheng and Chaddock.

Both the analytical model of Cheng and Chaddock and the numerical model of Cho, Kang, Kweon and Kim assume a static situation. The models are for the condition of a static bubble in an infinite liquid medium. This might be more suited to the analysis of the bubbles of piped gas of a known volume pressed into a liquid phase from a syringe. However this model may not be very appropriate for the dynamic processes involved in boiling in liquid nitrogen since it does not account for the non-isothermal condition of continuous volumetric bubble growth by evaporation throughout the duration of a bubble growth. This may be significant for liquids with low latent heat of vaporisation and where all heat transfer is occurring at a single nucleation site. In addition if the conditions for the bubble to be pressed toward the heated wall occur then this will increase evaporation at this location.

Ogata and Yabe [77, 78] also examined the behaviour of nucleate boiling on surfaces, both experimentally and theoretically. Experiments were conducted for approximately coaxial electric fields. The working fluids in these experiments were ethanol (C_2H_5OH), R-11 (Trichlorofluoromethane), R-11 with ethanol, R-113 (Trichlorotrifluoroethane) and R-113 with ethanol. Experimentally it was observed that in all fluids except R-11, bubbles elongated in the direction of the applied field

and horizontal motion of bubbles across surfaces occurred. To understand this behaviour the electric potential distribution was analysed for the case of a spherical bubble and the deformed bubble dimensions achieved experimentally. Calculation of the resultant Maxwell and electrostriction forces caused by an applied electric field on a single bubble showed that the force normal to the wall pushes the bubble onto the surface, but there is a larger force applied tangential to the plate. This calculated tangential force is thought to explain the vigorous movement of bubbles across the surface, stirring and breaking-up bubbles, as seen experimentally. In turn this is thought to result in a smaller departure size for bubbles and suppression of transition to film boiling, increasing the CHF. The lack of effect that singles out the result for R-11 is due to the significantly greater charge relaxation of 1.3 s compared to the other fluids charge relaxation times ranging between 1.9×10^{-3} for ethanol up to 9.8×10^{-1} for R-113. Thus this result confirms the importance of the charge relaxation time of the liquid on heat transfer processes noted in previous work [80-82, 94, 95].

It has been found that the charge relaxation time and the period of the process variables change the effective behaviour of the fluid as conducting or insulating. This has implications for the EHD effects that can be in operation within the dielectric system. As discussed, process variables that will determine the importance of the relaxation time of fluids in EHD enhanced boiling can include the period of the applied field [80], oscillations of the vapour-liquid interface [81], time of bubbles between electrodes i.e. the detachment period of bubbles [88] and time of flight within an electrical field.

Kweon and Kim experimented with R-113 boiling from a thin wire in a highly non-uniform electric field. R-113 has a charge relaxation time of about 10 s and a bubble departure period of the order of 10 ms. They observed a marked increase in average departure frequency and decrease in bubble diameter for an increasing applied electric field. The contribution to the force acting on the bubble was assigned to dielectrophoretic force as the relatively large relaxation time of the working fluid means that there will be no contribution from electrophoresis (Coulomb force) [93].

The experimental results of this study are distinct in providing results for the case of thermal nucleation from a single site in uniform electric fields. For the case of liquid nitrogen as the working fluid the relaxation time (τ) is estimated greater than 34 hours. It is difficult to know accurately as this value is obtained using;

$$\tau = \frac{\varepsilon}{\sigma} \tag{4.5}$$

The value of conductivity for LN_2 is estimated to be greater than 10^{-16} S m^{-1} [39] and LN_2 has a measured relative permittivity of 1.44 [14, 39]. Although the charge relaxation time is estimated it is certainly anticipated to be large relative to other dielectric fluids [40]. It should also be noted that impurities such as ice will influence the conduction between electrodes in liquid nitrogen [96].

From Figures 4.8 and 4.9 it can be seen that for these experiments the frequency of bubble departure occurs between 10-27 Hz, i.e. always with a period less than 0.037 s. This time is therefore much shorter than the charge relaxation time and this means that the liquid can be treated as highly insulating for the speed of the events under study, bubble generation and nucleation. The electric field is therefore distributed within the liquid and the vapour. The implication of this result is that there is not sufficient time for free charge to build up on the bubble wall; i.e. there is no electrophoresis (Coulombic force) and the contribution from the first term of Equation 4.1 is not significant.

It is therefore necessary to explain the nature of the force acting on the bubble when an electric field is applied. The ac result shows an oscillation of the bubble at 100 Hz indicating that the force is acting for both of the half cycles of the applied 50 Hz sinusoid voltage. This indicates that the force acts in the same direction irrespective of the polarity of the applied field and leads to the conclusion that it is in fact dielectrophoretic and or electrostrictive in nature [86]. Dielectrophoretic action the second term of Equation 4.1, will act on the polarised charges of the molecules due to the gradient of permittivity. There must a region of higher electric stress for one end of the induced dipole to be attracted with greater force than the other end is repulsed. For the bubble growing on a wall by thermal nucleation in plane-plane

electrode arrangement, the region of highest electrical stress is the region around the bubble itself, Figure 4.10. To provide an appreciation of the electric field around a gas nitrogen bubble within liquid nitrogen and originating from the cavity a simple FEA model has been constructed Figure 4.10. The surface colours indicate the magnitude of electric stress, the contours represent 30 divisions in the electric stress magnitude. A potential of 1 p.u. is applied between the electrodes for this plot. The axis of symmetry is the left hand edge, i.e. x = 0.

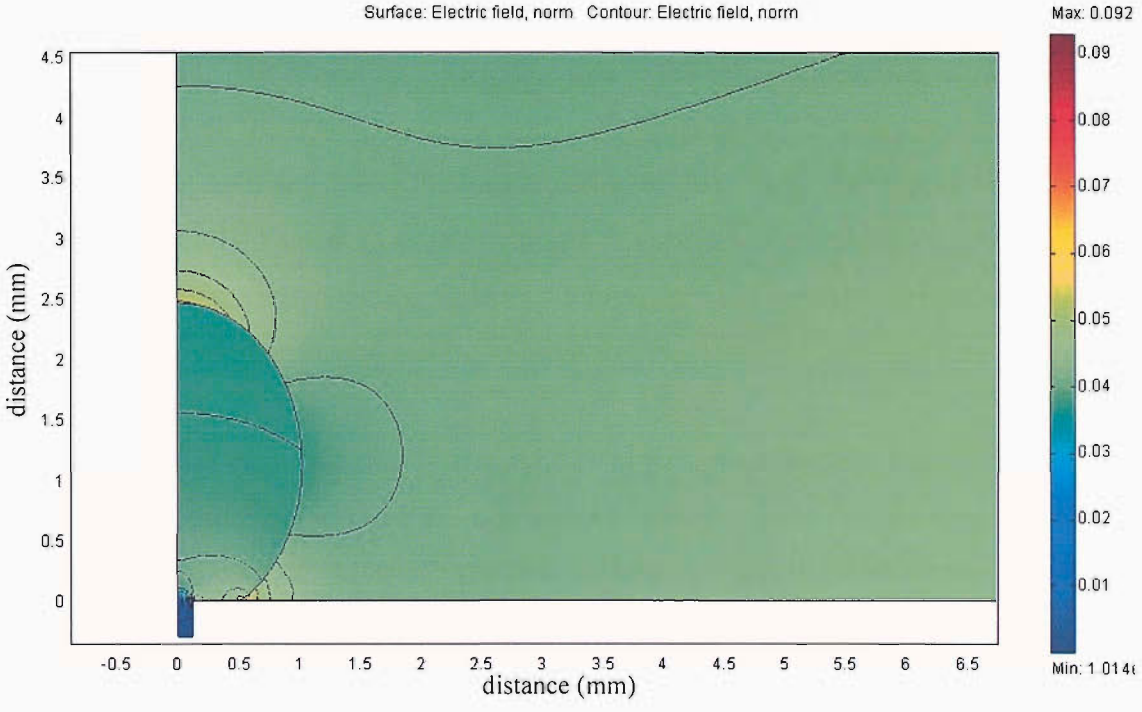

Figure 4.10, Electric field strength (p.u. mm^{-1}) plot of nitrogen gas bubble growing from the cavity (bottom left) in the bottom electrode.

The bubble modelled is that from a dc experiment and is simplified to an ellipse with a major radius of 1.331 mm and a minor radius of 1.025 mm centred 1.441 mm above the bottom electrodes surface. The assumptions of the model are the simplification to a perfect ellipse and no "neck" arising due to surface tension at the electrode surface. Despite these simplifications this model serves to highlight the regions of highest stress for a gas bubble on the bottom electrode surface. In Figure 4.10 the high electric stress is at the top of the bubble and giving rise to the force elongating the bubble in line with the applied field is clearly seen. There is also an electric field gradient acting downward on the bottom half of the bubble

holding it to the electrode surface. In addition electrostriction, the third term Equation 4.1, will occur due to the gradient of the permittivity and that of the electric field. The direction of electric field gradient and resulting force along the liquid-vapour interface acts from the horizontal centreline up toward the bubble tip and down toward the plane electrode. The electrostriction acts as a pressure along the liquid/vapour interface.

Thus the applied field causes a force elongating the bubble in the direction and holding the bubble to the cavity mouth on the heated wall. This analysis fits with the data obtained. The aspect ratio increases due to the elongating action of the forces. The forces hold the bubble to the heated wall which has a fixed heat transfer rate, thus volume increases due to the longer period of departure. The longer period can be attributed to the need for greater volume of vapour to form within the bubble to overcome the greater retaining forces by buoyancy. The increased retaining forces being dielectrophoretic and electrostrictive forces.

With regard to the effect this electrostatic field has on the boiling process, Figure 4.8(d) and Figure 4.9(c) show the normalised vapour volume of departing bubbles generated per second. Although the heat transfer rate was not directly measured these plots would suggest that the heat transfer by latent heat is reduced and that due to the lower frequency of bubble departure less stirring effect will occur. Both of these effects will reduce the heat transfer rate for a given wall superheat, pushing the boiling curve towards the right.

4.3.9 Negative dc and randomised run order results

With ac results demonstrating a force applied due to the electric field for both half cycles results for negative dc fields were investigated, Figure 4.11. With the relationship between the frequency, volume and aspect ratio established, results for frequency have been taken as an expedient method to indicate rapidly the nature of behaviour. These results are shown in Figure 4.11 and demonstrate similar trends for frequency with applied electric field strength. This experimental run uses the same sample as before however the inter-electrode spacing was halved to 15 mm. Comparable electric field strengths with the previous figures are therefore achieved for half the applied dc voltage. To ensure there was no conditioning of the system

two complete voltage sweeps were performed. First starting with a negative polarity -40 kV measurement for frequency and then progressing up to 0 kV and then further up with positive polarity to +40 kV. 0 kV measurements were also taken at the start and finish of the run. The second run was performed with a randomised order of potentials, switching in the following sequence; 0, -30, -10, 7.5, 20, -7.5, 40, 5 25, -15, 0, 15, 2.5, 35, 10, -20, -25, -35, -2.5, 30, -40, 0 kV.

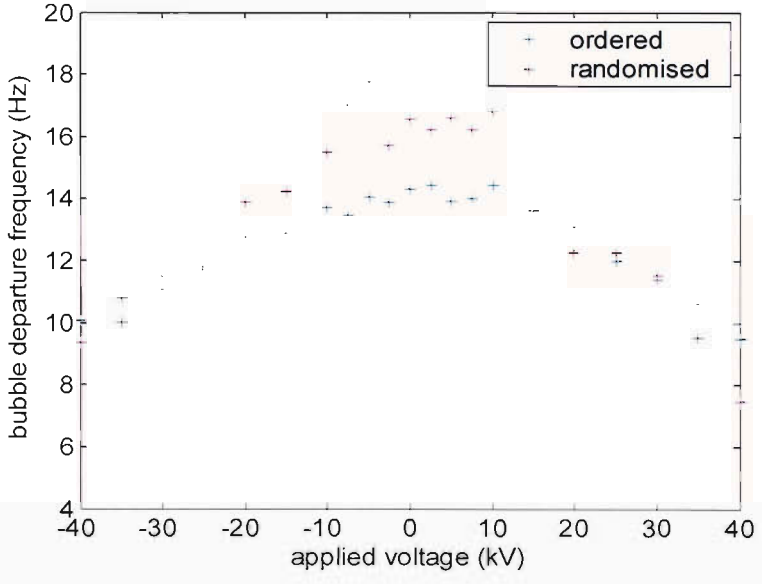

Figure 4.11, Mean bubble departure frequency against applied dc voltage, positive and negative polarity, swept and randomised order

The two runs were performed on successive days and the same heater power of 272 mW was used. Image sequences were recorded at 1000 fps. The temperature for the ordered run was 72.9 ± 0.5 K, the randomised 72.4 ± 0.5 K.

4.3.10 Discussion – nucleation stability

It is noted that although the trend for reducing frequency with increasing applied dc field strength matches with the results of the previous positive dc run, the frequency for zero applied potential has shifted. This can be attributed to variations in the bulk temperature and wall superheat, for which the bubble detachment frequency is sensitive, as is clear from the analysis of Malenkov [97]. The lower bulk liquid temperatures of these results required a higher wall superheat (ΔT_S) for nucleation to

initiate; this causes a lower departure frequency. In Malenkov's model the frequency of bubble departure for the case of no applied field is calculated by consideration of the bubble departure velocity.

$$f = \frac{1}{\pi D_B}\left(1 + \frac{q}{\rho_V \lambda_{LV} u_B}\right) u_B \tag{4.6}$$

Where u_B is the departure velocity of the bubble, and D_B is its diameter.

$$u_B = \left[\frac{D_B g(\rho_L - \rho_V)}{2(\rho_L + \rho_V)} + \frac{2\sigma}{D_B(\rho_L + \rho_V)}\right]^{\frac{1}{2}} \tag{4.7}$$

The bubble departure diameter can in turn can be found from the equation formulated by Kutateladze and Grogonin [98].

$$D_B = 0.25\sqrt{\frac{\sigma}{g(\rho_L - \rho_V)}}\left[1 + \left(\frac{Ja}{Pr}\right)^2 \frac{1}{Ar}\right]^{\frac{1}{2}} \tag{4.8}$$

In addition to the Laplace surface tension coefficient, σ, the diameter is seen to depend on the dimensionless; Jakob number, Ja, Prandtl number, Pr and Archimedes number, Ar, where these dimensionless values are defined as;

$$Ja = \frac{\rho_L c_{pL} \Delta T_S}{\rho_V \lambda_{LV}} \tag{4.9}$$

$$Pr = \frac{\mu_L c_{pL}}{k_L} \tag{4.10}$$

$$Ar = \frac{g}{\nu_L}\left(\frac{\sigma}{\rho_L g}\right)^{\frac{3}{2}} \tag{4.11}$$

Figure 4.12 shows these theoretical relationships graphically, for the no field condition. Figure 4.12(a) shows a high degree of theoretical sensitivity in the frequency of bubble departure to small changes in the wall superheat. Whereas the diameter is proportional to wall superheat Figure 4.12(b). The sensitivity of bubble departure frequency is especially evident in the region of interest to these experimental results, wall superheats in the range 1 to 5 K.

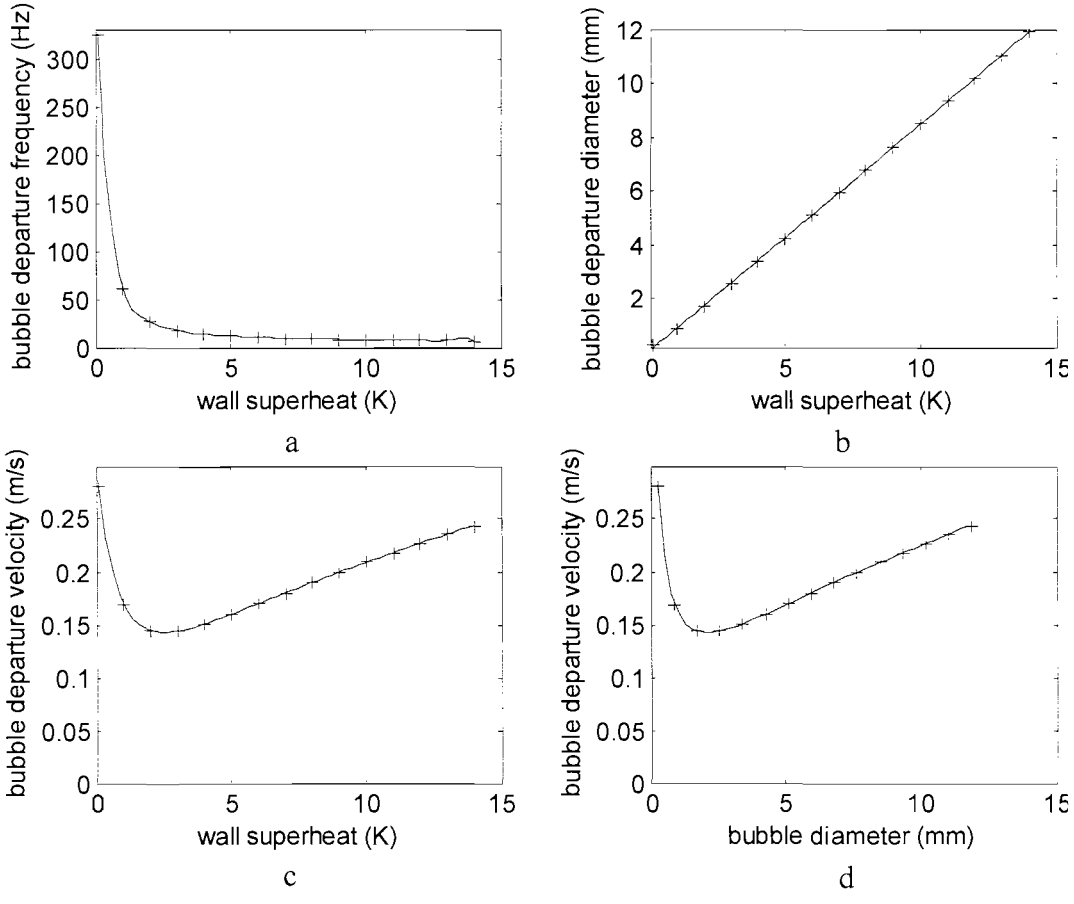

Figure 4.12, Theoretical bubble departure for the physical parameters of LN_2, for the no field condition

Furthermore the relationship of bubble departure velocity against wall superheat and the related bubble diameter are shown in the plots of Figure 4.12(c) and (d). Starting from zero and increasing wall superheat it can be seen that at first the bubble departure velocity decreases, after a minimum condition however, at a wall superheat of 2-3 K, the increase in bubble size with increasing wall superheat means that the bubble departure velocity again increases.

The validity of this model has practical limitations, because increasing the wall superheat too far will cause boiling from multiple sites and too little wall superheat results in no nucleation at all. At a wall superheat of 2 K and with a frequency of 26.8 Hz theory would predict a bubble diameter of 1.71 mm. This is considerably larger than the measured result for the diameter of bubbles, of approximately 900 μm, at this same frequency. Considered in another way, for a given bubble size a much lower detachment frequency is observed experimentally than is predicted by theory.

This could be due to fact that the bubbles in these experiments are nucleating from a cavity. Later experimental results were collected with a camera system that allowed faster download and online visual analysis. This improvement lead to a closer examination of the bubble departure and the observance of smaller bubbles occasionally being released from inside the cavity and joining the freshly released bubble. It appears therefore that for this sample the cavity size and construction creates conditions for nucleation from the inner walls of the cavity. Bubbles nucleating inside the cavity are then coalescing to form the larger bubble volume protruding from the surface and measured previously. This can cause instability in the frequency of the detachment frequency and may explain the discrepancy from theory. The sensitivity of the theoretical model to small changes in wall superheat in the range of interest may also explain the discrepancy between theory and experimental results due to relatively large uncertainty in the measurement of the wall superheat at these temperatures of 0.5 K.

The frequency instability was investigated by consideration of the data collected. It is important as it guides the view held of the data with respect to assumptions about analysis and statistical treatment of results. This is illustrated by consideration of Figure 4.13(a), showing a full frequency sweep with 95% confidence intervals also plotted. For this Figure the number of data samples varies between 14 and 22 samples except for at zero potential which was recorded in seven runs recorded in time between other results and averaged from 163 recorded periods. This accounts for the larger range and narrower confidence interval of the data for zero applied potential. Figure 4.13(b) shows the same data with maximum and minimum data plotted and Figure 4.13(c) shows the range against applied voltage. Data for this

figure was collected at 5000 fps giving a maximum error of 0.2 ms for each measured period, representing only 0.18% at 9 Hz and 0.34% at 17 Hz.

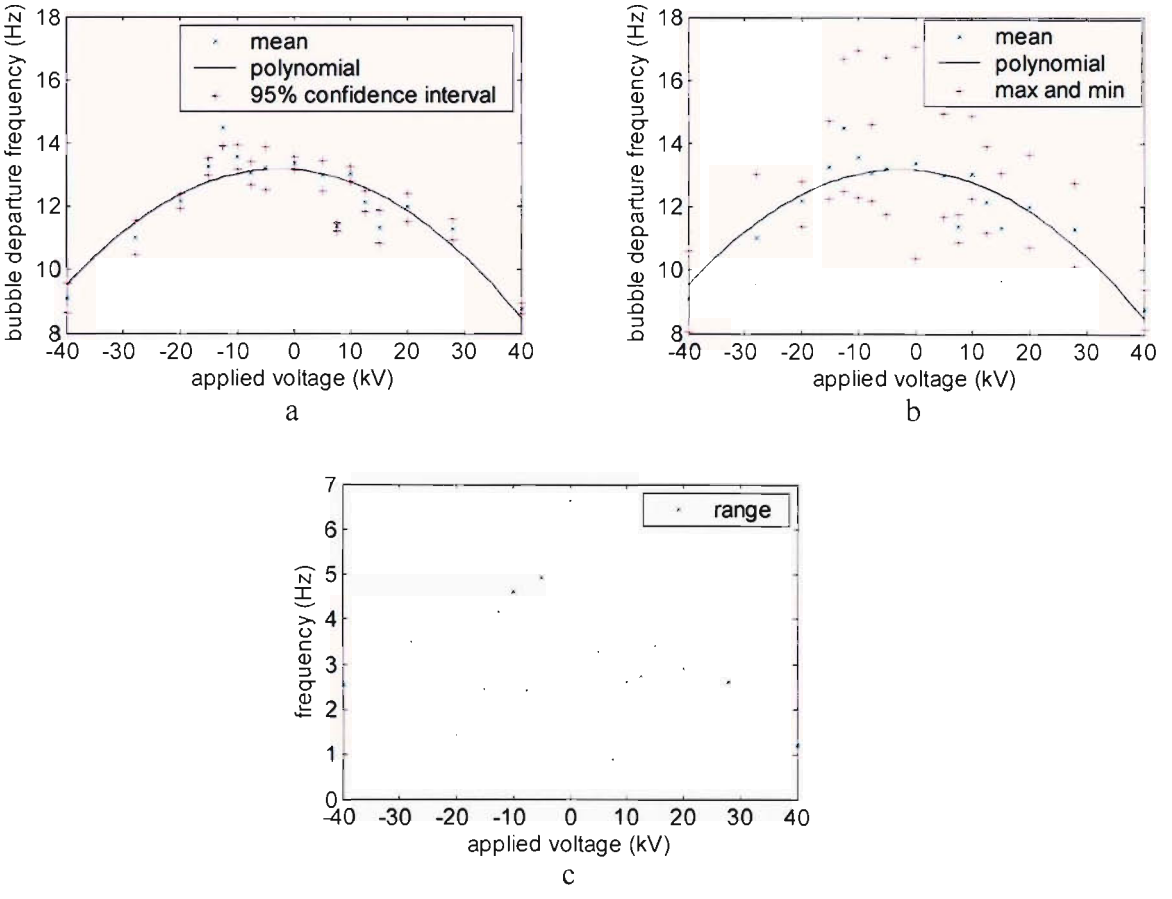

Figure 4.13, Departure frequency analysis, a) with 95% confidence intervals, b) with min and max points, c) range against applied voltage

Figure 4.13 indicates that the use of standard deviation and therefore percentage confidence intervals requires further scrutiny as the fitted curve, a second order polynomial by the method of least squares regression; does not fit the data well nor fall within the confidence interval. This is due to the departure frequency data not obeying the assumption that errors are random and normally distributed and that the data are independent. Figure 4.14 shows a run chart of detachment periods in frames. The camera recording frame rate was 5000 fps for this experimental run. There is obvious interaction from one departure period to the next and therefore an assumption of independence within the data is unwarranted. The inter-dependence of the data could be a result of the smaller bubble nucleation from within the cavity nucleating into a previously detached bubble, increasing the time for the subsequent

large bubble to obtain sufficient volume to detach. This inter-dependance may also be due to fluid currents, possibly electro-convective currents across the electrode surface interface or Rayleigh-Taylor instability due to the rising bubble column. It is also conceivable that the instability is due to chaotic behaviour induced due to the closeness of the electrode spacing and the influence of one bubble on the electric field influencing the growth and detachment of the next. Such behaviour has been shown to occur in glycol [99]. For the present, however, the nature of this instability in the present experimental arrangement remains an open question.

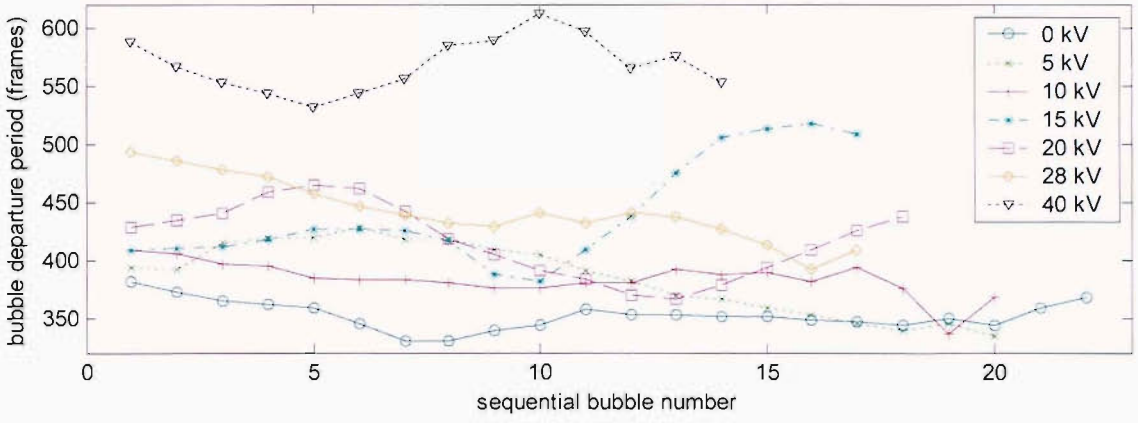

Figure 4.14, Run charts of bubble departure period (frames)

4.4 Summary and conclusions

In this chapter the possible EHD forces that could act on bubble nucleating within LN_2 and applicable theory has been reviewed. Experimentation of bubbles nucleating in LN_2 from an electrode with an embedded heater and an artificial cavity has been described. The experimental approach of this study is distinct in providing results for the case of thermal nucleation from a single site. The influence of an electric field on bubble nucleation at a single site has been characterised quantitatively by measurement of bubble detachment frequency, aspect ratio, volume and normalised volume per second. By maintaining a steady heat transfer rate it has been observed experimentally that thermally induced bubbles growing in a uniform field will be elongated in the direction of the field and held on the superheated wall for longer periods.

This result may be somewhat unexpected due to the general discussion in the literature focussing on the enhanced boiling potential of electric fields applied to the nucleate boiling regime, but is however predicable by consideration of the experimental arrangement and resulting electric field. Examination of the forces involved and the properties of LN_2 lead to a hypothesis that Columbic stress due to charge collection on the vapour-liquid interface is not responsible for this action. This is because the charge relaxation time of liquid nitrogen is relatively longer than the period of bubble detachment. The retaining force is therefore dielectrophoretic and electrostrictive in nature. The field non-uniformity, a necessary prerequisite for these forces to be present, is due to the relative permittivity of the vapour bubble and liquid phases and the resultant deviation from uniform of the electric field between the uniform plane-plane electrodes. As the bubble is held on the surface for a longer period a larger volume per bubble is produced, the aspect ratio increases, frequency of departure reduces and vapour volume released from the heated surface per second remains relatively constant. This would indicate that heat transfer may be uneffected or suppressed with an applied field under certain uniform field arrangements for insulating liquids and has implications for the successful design of liquid nitrogen based insulation systems for HTS equipment. This knowledge is also pertinent to the design of refrigeration systems where it is desirable to enhance boiling with EHD effects.

The boiling process in any liquid is complex and modelling the EHD effects on the nucleate regime continues to be challenging. An area worthy of future investigation that has arisen from the results presented is the investigation of the cause of the inter-dependence of the bubble detachment period. In addition, despite some work of previous authors toward modelling bubbles in electric fields and the EHD forces present these are for static bubbles and usually for the conducting liquid case. Present models take no account of the dynamic nature of nucleating bubbles, the effect this has on the free charge within the system, and none attempt to address the growth from a thermal source or electrophoretic behaviour in the liquid bulk arising from the conductivity and permittivity gradients due to a thermal gradient.

Despite this there exists a large body of knowledge of EHD action in liquids. In the context of an electrical insulation system it has been shown that the increase of the

vapour in the liquid gap will degrade the electrical withstand performance [57, 100]. Thermally induced bubbles will be influenced within electric fields as has been discussed and shown quantitatively by experimentation. The non-uniform fields can cause the bubble to move toward the region of low electrical stress. It has already been shown from the experimental results of other authors, that vapour can be locked to the HTS conductor and that breakdown in the vapour phase within liquid nitrogen correspond well to those lower levels predicted by Paschen's curve [15, 59, 100].

Chapter Five

Streamer Behaviour in Divergent Electric Field Geometries

5.1 Introduction

It has been shown earlier (Chapter 2) that work to characterise the electrical properties of liquid nitrogen has been concentrated on breakdown measurements. Pre-breakdown or partial discharge has also been studied in liquid nitrogen, in part because the relatively simple chemistry provides an attractive medium for the study of the physics of the pre-breakdown and breakdown mechanisms. Pre-breakdown phenomena is the subject of this chapter.

Partial breakdown is also of interest as discharge activity will potentially have a serious impact on the application of liquid nitrogen or liquid nitrogen composite insulation systems. When liquid nitrogen is electrically stressed by a strongly divergent field many phenomena are manifest including; electrohydrodynamic effects and partial breakdown resulting in light emission, acoustic waves and density change streamers [101-103]. These effects are important when considering the integrity of an electrical insulation system employing liquid nitrogen as a dielectric.

In this study experiments have been performed to characterise the behaviour of pre-breakdown streamers in sub-cooled liquid nitrogen composite insulation systems. A divergent electric field geometry, point-plane, has been used to initiate partial breakdown for a liquid nitrogen system with a glass reinforced resin (GRR) barrier over the plane electrode. It is known that pre-breakdown events in liquid dielectrics produce a streamer, a vapour cavity or low density region that propagates through the liquid and that can be imaged due to the difference of refractive index compared to the bulk liquid. Streamers occur when the discharge mechanism into the liquid heats the nitrogen above its point of vaporization, causing the generation of vapour filaments.

A technique that allows time correlated partial discharge signal and image capture of density change streamers has been developed. This method provides high temporal and spatial resolution measurements utilising stroboscopic high speed digital imaging with a copper vapour laser source to backlight the sample. Using this technique the magnitude of apparent charge and phase relationship can be correlated to a partial discharge event in the liquid nitrogen and simultaneously captured digital images of the resulting density change streamer. Imaging of density change streamers has shown that two different types of density change streamer shape are observed. Captured images demonstrate that discharge activity in the liquid results in vapour production which remains in the gap after the discharge extinguishes. Example image sequences are presented and discussed with respect to partial breakdown theories.

5.2 Theory of pre-breakdown in liquid dielectrics

In the last thirty years significant work has been completed towards the goal of understanding the process of streamer initiation and propagation in liquids [101-105]. Studies have been performed in a range of dielectric liquids including oils and non-polar liquids. These studies have gathered a great deal of data making use of techniques to record images of streamer propagation with high frame rate stroboscopic and Schlieren photography and the capturing of emitted light with image intensifiers. In addition the use of high speed digital oscilloscopes to record current and voltage waveforms and spectroscopic studies has also added to understanding of the processes involved in streamer propagation. Many factors are

known to affect the propagation of streamers in liquid dielectrics, including the chemical composition and physical properties, contaminants, hydrostatic pressure and temperature, electrode geometry and material; applied voltage magnitude, wave shape and polarity [102]; however with so many complexities the knowledge of the pre-breakdown phenomena is incomplete. Research continues internationally and much effort is still devoted to experimental study and theoretical development. This chapter describes an experiment using point-plane electrode geometry and so consideration of pre-breakdown processes is limited to streamer initiation and propagation, so called short-term processes acting in nanosecond or millisecond timeframes. Conceptual models for streamer initiation and propagation within a point-plane electrode geometry in liquid dielectrics are first discussed.

5.2.1 Streamer initiation

The mechanisms for streamer initiation and subsequent propagation are polarity dependent and each stage is considered for each polarity in turn.

5.2.1.1 Negative polarity point electrode

It is well documented that the negative polarity point streamer initiation begins with the formation of a bubble at the needle tip, this is accompanied by a current pulse. The formation of microbubbles ($r_b < 10\mu m$), subsequent growth and collapse have been well characterised. It has been shown that the current pulse from the cathode provides the energy to create the bubble, it has been hypothesised by localised heating of the fluid resulting in evaporation. The bubble expansion and collapse can be closely described by the Rayleigh model of cavitation and the growth and rebounds are limited by the liquid inertia and work against the pressure of the liquid. Furthermore it has been shown that the bubble can be considered a constant energy system, the energy supplied only by the current pulse without additional electrostatic forces provided by the high electric field [14, 49, 53, 106-109].

The mechanism of streamer initiation from a cathode needle tip current pulse can be described as beginning with electron injection by Fowler-Nordheim or Schottky injection. The possibility of field emission into liquids using very sharp points ($r < 2\mu m$) has been experimentally verified [110-112]. In these experiments no

pressure dependence was observed for the voltage-current relationship, and no pre-breakdown phenomena are initiated, e.g. light emission or bubble formation.

5.2.1.2 Electronic properties of liquids

If electron ejection and avalanche is important, first for local heating and bubble generation and then for initiating streamers, as has been proposed e.g. [49, 55, 101], it is useful to consider the electronic properties of the liquid. However, the electronic behaviour of liquid dielectrics is not well understood. The disorder and dynamic system of molecules cause difficulty if attempting to define electronic conduction theory for the liquid state. To progress in the absence of a complete theory, electronic theory from solids and gases is used where it is considered to aid understanding. The following sections present proposed theory of the electronic properties of liquids; some ideas have been developed from the theories of conduction in solids and gases.

5.2.1.3 Electron affinity in liquids

Measurement of photoelectric currents from irradiated metal targets in dielectric liquids against the wavelength of light allows the fitting of the Fowler-curve; a theoretical relationship relating the measured photocurrent to the energy required to free an electron from the metal surface. Using this function to calculate the effective cut-off frequency allows calculation of the change in the work function from the value for metal into a vacuum, W_V, to the value for a metal into a liquid, W_L. This has been termed the "work function of the liquid", V_0 [113]:

$$V_0 = \Delta W = W_L - W_V \tag{5.1}$$

The value of V_0 can be considered as a measure of the electron affinity of the liquid. For LN_2 the value of V_0 is measured to be $+0.05 \pm 0.03$ eV [114]. The positive value means that energy is required to move an electron from the vacuum level into the LN_2. A negative value is typical for many dielectric liquids and means that energy is required to remove an electron from the liquid to the vacuum level. The concept of electron traps is employed to explain the liquid affinity. The nature of the energy traps in liquids is not well understood and there exists debate as to its true nature in LN_2. Several models have been developed to explain its experimental observation.

The value of V_0 depends on the relative magnitude of the attractive polarization forces and the repulsive forces between the liquid molecules and the electrons. To remove electrons from a liquid with a negative value would release energy of the value of V_0. For dielectric liquids a large negative value of V_0 indicates that the repulsive forces are dominated by the polarisation forces holding the electron to the liquid molecules. Electrons injected into LN_2 interact with the liquid molecules and this influences the electron mobility which has also been experimentally measured [115, 116].

5.2.1.4 Electron mobility

The ion and electron mobility of LN_2 has been theoretically treated and experimentally measured using a time of flight method. Electron mobility in LN_2 has been measured at the normal boiling point to be approximately 2 to 3 $\times 10^{-3}$ cm^2 $V^{-1}s^{-1}$ [115, 116]. This is a relatively low mobility for liquefied rare gases (for example compared to LXe that has an electron mobility of 2×10^3 cm^2 $V^{-1}s^{-1}$). Difference between the measured valuess may be due to contamination of impurities, especially oxygen which may cause electron attachment to the oxygen molecule and the increased effective mass and drag of the resultant anion would reduce the magnitude of the measured drift velocity.

V_0 has been used to define the first ground state of the excess electron in a liquid and since the electron moves throughout the liquid in this state it has been termed the "conduction band" by some workers [113, 117]. This interpretation is misleading as the electron is not "free", that is able to move for extended space, as is implied by the term "conduction band" when applied to crystalline conductors. In LAr it was observed experimentally that electron mobility was higher in the liquid than in the gas for a temperature range of 135-150 K [116]. This has been used to suggest that the closer interactions of molecules in the liquid reduced scattering effects and aided conduction, encouraging the use of the conduction band theory. However this effect has not been observed in LN_2. Electrons are known to be in a localised state in LN_2 as observed by the lower mobility in liquid than that in the gas. Two models have been proposed for this localised state in LN_2, the first a formation of anions, the second the formation of electron bubbles as is known to occur in LHe and LNe.

Gee, Floriano, Wada and Huang have suggested the formation of temporary anions [116];

$$e^- + N_2 \Leftrightarrow N_2^- \tag{5.2}$$

This may be stabilized further in the liquid with the addition of another neighbouring molecule in the process;

$$N_2^- + N_2 \Leftrightarrow \left[N_2\right]_2^- \tag{5.3}$$

or

$$e^- + \left[N_2\right]_2 \Leftrightarrow \left[N_2\right]_2^- \tag{5.4}$$

where $[N_2]_2$ is a van der Waals dimer; this can then be generalised;

$$e^- + mN_2 \Leftrightarrow \left[N_2\right]_m^- \tag{5.5}$$

The effective lifetime of the anion has been estimated from experimental results in a gas to be of the order of 0.7 ps and this was found to increase with density [118].

The formation of a potential energy well by the formation of an electron bubble, so called self-trapping, has been used by Sakai, Schmidt and Khrapak to explain the low electron mobility measured in LN_2 [115]. The concept of potential energy wells is common when using a quantum mechanical approach to electron movement; the difficulty in applying these concepts to LN_2 is in defining the energetics of the well. To develop the model for the potential energy macroscopic properties have been used to estimate the potential energy of the well. The bubble model depends on three terms, first the electronic binding energy, the repulsive force between molecules and electrons. The second term is the work required to create the inner surface of the bubble against surface tension and the third term is work to balance the liquid pressure external to the bubble. The transition of the electrons from a localised state in the proposed electron bubbles near the triple point of nitrogen to a free state near

the critical point dependent on the liquid temperature (free when T > 115 K) [115] thereby also satisfies the change in mobility observed in experimental results [116].

It has been shown that the product of viscosity and electron mobility is constant for a range of temperatures [116]. In LHe and LNe the product of viscosity and electron mobility changes with temperature as anticipated due to corresponding changes in density and pressure which influence the size of the bubble. That this does not occur for LN_2 casts doubt on the use of the bubble model and it is reasonable to accept the anion theory.

Furthermore it is worth noting that due to the disorder of the liquid molecules which will be continuously moving and reordering the depth of the potential energy trap will be continuously changing also. This has led some researchers to use the concept of a band of conduction levels, but due to the lack of order in a liquid a conduction band that extends in space will not exist. The movement of the electrons is therefore explained by consideration of the attachment of electrons to a cluster of molecules to form a temporary anion or the effective mass of the electron bubble which has an associated work and time required to reorder the surrounding liquid molecules to allow its motion.

Whatever the true nature of the electron trapping or attachment mechanisms in operation, the positive value of V_0 measured for LN_2 means that the effective work function for the experimental arrangement described in this study, using a tungsten needle, will require greater energy to cause an electron to escape the metal surface into LN_2.

5.2.1.5 Liquid ionisation

A method to estimate the ionisation of a liquid has been proposed by Schmidt [117]. Due to the difficulty with defining conduction theory for liquids, theory is developed from liquid and gas theories. It has been shown that the conductivity of semiconductors upon melting decreases by only a factor of 2. This has been used to justify the assumption that short-range ordering of the molecules in the liquid phase plays an important role in their conduction properties. As mentioned this is not a suitable model for LN_2 electronic motion, but the measurement of the V_0 and its use

may provide useful to estimate the ionisation energy in LN_2. If the existence of a conduction band is assumed to exist in the liquid phase it will be located at a position V_0 from the vacuum level. This is shown diagrammatically with reference to the energy level model of solids, Figure 5.1 [117].

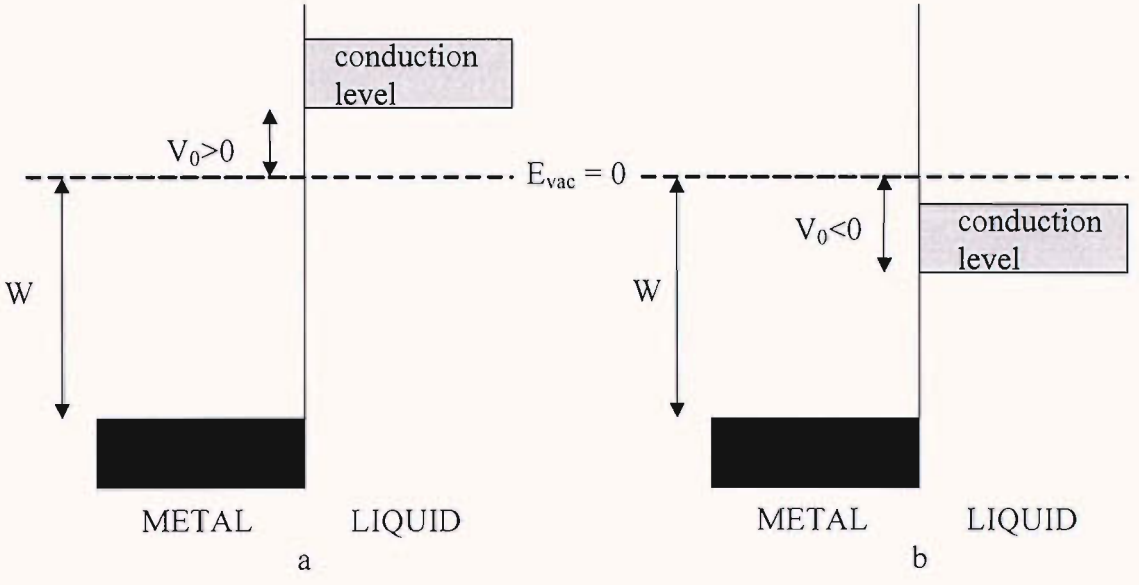

Figure 5.1, Energetic position of the proposed electronic conduction level, V_0 of the liquid with respect to the vacuum level [117], for the cases; a) $V_0>0$ and b) $V_0<0$.

It is known that the atoms or molecules of the gas phase are characterised by an ionisation energy, I_g (eV), which is defined as the energy to remove the outermost valance electron to infinity, as shown in Figure 5.2. Where the energy of vacuum is taken to be zero. It is argued that during condensation of non-polar liquids the valence electron energies move and form a band; it is also proposed that a conduction band is formed and that these bands are separated by an energy greater than 5 eV [117]. Following this argument it is possible to calculate the proposed "band gap" using the following expression;

$$I_l = I_g + P_+ + V_0 - E_{val} \qquad (5.6)$$

where I_l is the "band gap" of the liquid, P_+ is the polarisation energy of positive charge which reduces the ionisation energy; E_{val} is the energy of the valance band. It is argued that a broadening to form a band occurs due to the weak van der Waals forces which cause the greater interaction between molecules in the condensed

phase; it is estimated that the broadening of the band will be of the order of a few tenths of an electron volt [117].

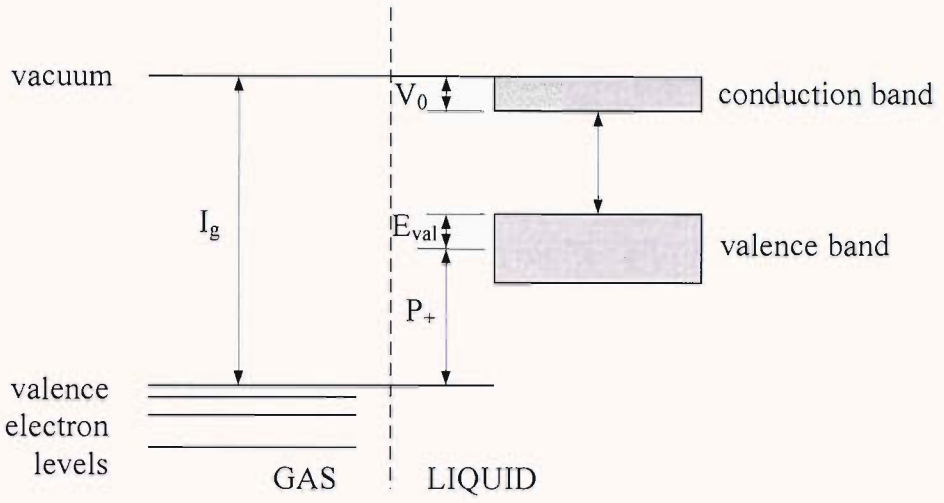

Figure 5.2, Electronic energy bands in liquids [117].

The ionisation energy is the energy required to create an electron and hole pair, also defined as the energy required to remove the outermost valence electron to infinity. The ionisation energy of gaseous nitrogen, N_2, has been measured to be 15.581 ± 0.008 eV. The appearance energy is 24.4 ± 0.25 eV to produce a N and N^+; or 48.0 ± 2 eV to produce $2N^+$; where N is a neutral nitrogen atom and N^+ a positive nitrogen ion [119]. These values represent a survey of experimental results obtained using several methods including; optical spectroscopy, electron impact techniques, photo electron spectroscopy or photoionization mass spectroscopy.

Following the analysis of Born [120] the polarisation energy of a spherical charge, P_+, can be estimated using;

$$P_+ = -\frac{e_0^{\,2}}{8\pi\varepsilon_0 R_a}\left[1-\frac{1}{\varepsilon_r}\right] \tag{5.7}$$

where e_0 is charge of an electron (1.602×10^{-19} C), and R_a is the characteristic atomic or molecular radius. For N_2 the characteristic molecular radius is calculated to be $2.4a_0$, where a_0 is the Bohr radius (0.5292×10^{-10} m) [115]. By this method P_+ is

found to be -1.733 eV. The negative sign indicates that the polarisation force is attractive.

The work function, V_0, of liquid nitrogen has only been experimentally measured at the normal boiling point, and is found to be 0.05 ±0.03 eV [114]. However an estimate across a range of densities has been calculated using known relations demonstrated to fit other cryogenic liquid data well. This is close to the experimental result, providing a value of 0.6 eV for V_0 at a density number equivalent to the liquid phase at atmospheric pressure ($N_V = 1.729\times10^{22}$) [115]. Thus it becomes possible to estimate the proposed band gap using Equation 5.6;

$$\left.\begin{aligned} I_l &= I_g + P_+ + V_0 - E_{val} \\ I_l &= 15.581 - 1.733 + 0.6 - 0.3 \\ I_l &= 14.148\text{eV} \end{aligned}\right\} \qquad (5.8)$$

There are several difficulties with this approach. The value used for polarisation energy is approximate. The expression used, Equation 5.7, is unrealistic; the polarisation of a lone positive charge can not be considered realistic for the nitrogen molecule or the closer proximity and interaction of molecules in a liquid state. The use of E_{val} is also approximate, the existence or extent of broadening in nitrogen is unknown. For this reason the largest estimation has been used in the calculation of I_l to give an estimation of the lowest ionisation level to be anticipated by this model. Despite the conceptual difficulties of the approach outlined an approximation for the reduction in ionisation energy from the value measured in gaseous nitrogen is obtained. This indicates that the variance is small compared to the ionisation energy itself, less than 10%.

The model proposes the use of a conduction band. However there can be no "extended" state within the liquid phase due to the disorder of the system; even if there is order on the scale of a few molecules, as is argued, the trapping of electrons and disorder will impede the progress of electrons through the liquid volume. Thus the existence of an extended conduction band is not possible. There will exist, however, an ionisation energy, the energy required for the outer valance electron to

be released from the liquid molecules. This concept is employed to understand the generation of avalanche breakdown within the liquid state.

5.2.1.6 Field emission

It is known that conductors have a characteristic work function which is defined as the energy required to liberate an electron from the highest filled energy level in the Fermi distribution of a solid to a point infinite distance away, at absolute zero. Using the simple classical Drude model from 1900 the electrons in the metal are considered as a gas at room temperature and it is possible to estimate the energy using kinetic theory;

$$\frac{3kT}{2} = 3.8 \times 10^{-2} eV \tag{5.9}$$

where k is the Boltzmann's constant. This value is two orders of magnitude less than the work function of tungsten which in a vacuum is 4.35-4.6eV [42].

When a high voltage is applied to the needle tip electrode a highly divergent field results, with the region of highest electrical stress being at the tip of the needle. Electrons will be emitted from the metal electrode if a sufficiently high electrostatic field is present. This is known as field emission or Schottky effect [121] and is illustrated in Figure 5.3.

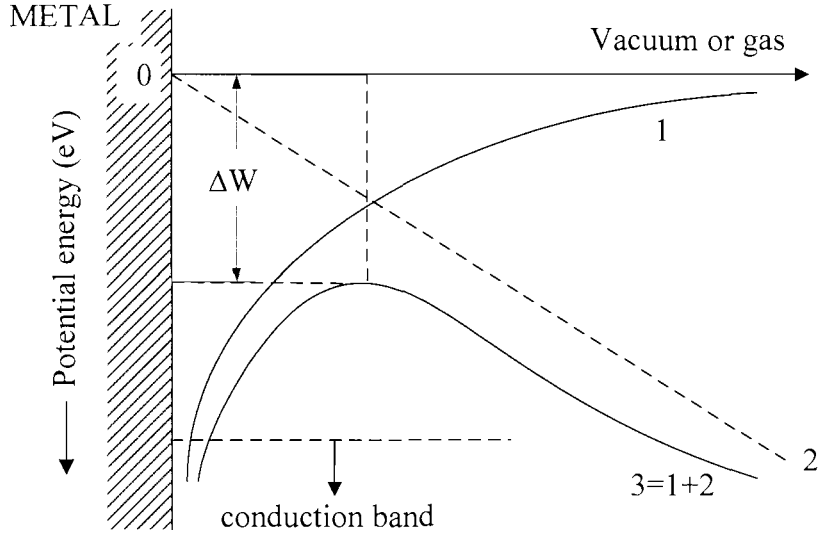

Figure 5.3, Diagram of potential energy barrier for field emission by tunneling

Referring to Figure 5.3, Line 1 represents the energy without an externally applied electric field. Line 2 represents the energy due to an applied external electrostatic field and line 3 the combined energy. Thus it is possible to express the lowering of the work function as;

$$\Delta W = -e\sqrt{\frac{eE}{4\pi\varepsilon_0}} \tag{5.10}$$

And hence the effective work function, W_{eff}, becomes;

$$W_{eff} = W - e\sqrt{\frac{eE}{4\pi\varepsilon_0}} \tag{5.11}$$

The resulting current can be found by the Schottky equation. However this picture is incomplete without considering the distribution of energies of the electrons in the metal. It has been found that at low potentials there is still considerable emission, an expression for the field emission has been derived by Fowler and Nordheim on the basis of Fermi-Dirac statistics and wave-mechanics [122]. Sommerfield had extended the simple Drude model by applying Fermi-Dirac statistics to electrons in a metal showing that some electrons have a definite probability of being in energy states above the Fermi level [123]. The Fermi-Dirac distribution, Equation 5.12, describes the probability that an energy state is occupied by an electron. The Fermi level represents the level with a 50% probability of being occupied. The levels above the Fermi level have a low probability of being filled, those below, a high probability.

$$f(E) = \frac{1}{1 + e^{(E-E_F)/kT}} \tag{5.12}$$

where E is an energy and E_F is the Fermi energy.

The construction of Figure 5.3 demonstrates that the external field lowers the potential energy required for an electron to leave the surface of the metal conductor

on the left, in the direction of the field, to the right. With a sufficiently high field applied there is a finite probability that some electrons will have sufficient energy to penetrate the potential barrier and leave the surface of the metal, this effect is termed tunneling.

Experimental investigation of current-voltage characteristics in LN_2 found that results agreed well with emission by Fowler-Nordheim tunneling for tip radii up to 0.5 μm, however for larger tip radii a current pulse or "Trichel" regime occurs so that the Fowler-Nordheim law no longer fits with the data [124]. The Trichel regime occurs when electrons emitted form a space charge in front of the tip which lowers the local electric field preventing further emission. The injected charge must then diffuse before the field is re-established and further emission can occur. The result is a train of current pulses which can be measured, each relating to field emission.

5.2.1.7 Electron avalanche

The emission of electrons into LN_2 has been observed experimentally, since it has been found that the injection is not dependent on hydrostatic pressure the injection is understood to be occurring in the liquid phase [125].

Electron avalanche processes are well understood for gases, where not all injected electrons with sufficient kinetic energy to ionise molecules will do so, but ionisation is subject to a probability function since a fast electron may pass a molecule without impact. This led Townsend to propose the use of a first ionisation coefficient, α, which is defined as the number of electrons produced, by ionisation, by an electron per unit length path in the direction of the applied field [126]. For nitrogen, if an electron collides with a molecule in the vapour which causes ionisation, there is a release of another electron and the production of a positive nitrogen ion;

$$e^- + N_2 \Rightarrow 2e^- + N_2^+. \qquad (5.13)$$

This will repeat in many steps and there is a multiplication of free electrons. This process is known as an electron avalanche; illustrated in Figure 5.4, where m represents a molecule being ionised.

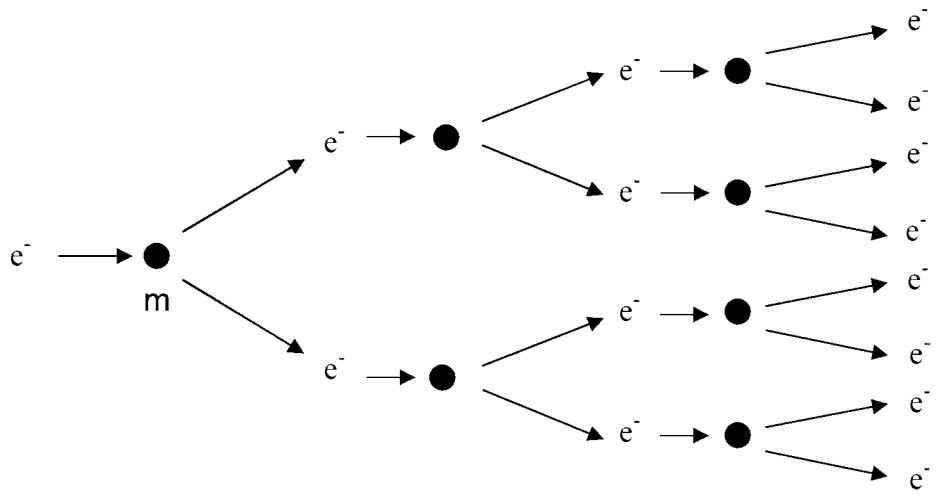

Figure 5.4, Pictorial representation of the electron avalanche process

The process can be described using α, Equation 5.14;

$$n = n_0 e^{\alpha d} \tag{5.14}$$

$$\frac{n}{n_0} = e^{\alpha d} = M \tag{5.15}$$

where n_0 the initial number of electrons and n is the number of electrons at a distance d from the cathode. The multiplication factor M depends on α which is proportional to the ratio of electric field stress at the tip (a function of tip radius) and the liquid density. For a purely field emission charge injection process M must be equal to 1 or less. Increasing the tip radius will cause the penetration depth and M to increase and the avalanche process will dominate [101]. Within an avalanche "swarm" there will exist a distribution of electron energies. The change in value of the swarm parameter defined as α divided by E, for changes in density; has been experimentally characterised for LN_2 [125].

For a negative tip in LN_2 it has been shown that for dc voltages applied to point-plane electrode geometry (point radii 1-15 μm) a bubble can be electrically induced to initiate a streamer [53]. It has been reported that at a threshold voltage the current jumps by several orders of magnitude and a regular current pulse train is observed. Furthermore the duration of pulses was measured to be 10 ns for LN_2 and this value

was not influenced by the purity of the LN_2. A current pulse causes the growth of a bubble, which grows to a maximum and collapses and rebounds. It has been attempted to fit the results to the Rayleigh model of cavitation, however good agreement only appears to exist above a pressure of 2 MPa. It was also observed that multiple current pulses can occur into a bubble once initiated. Where this occurs the Rayleigh model is less applicable as energy is injected with each pulse, whereas the Rayleigh model supposes a single energy injected to start the cavitation. It has been shown for a range of dielectric liquids that whilst the formation of a vapour bubble is not pressure dependant the bubble lifetime and maximum radius are increased for decreasing pressure and for increasing injected energy and liquid viscosity. It is also observed that the longer the bubble lifetime the greater the probability of discharges occurring into the vapour [101]. For LN_2 the discharges into the vapour completely disappear for pressures greater than 2 MPa [53], this results in the greater correlation to the Rayleigh model.

The threshold electric stress for a 1 μm radius tip has been estimated using a hyperboloid to plane approximation and calculated to be 1.1 MV mm^{-1} [53]. This is higher than for liquid argon (LAr), 0.35 MV mm^{-1}. It has been hypothesised that this is due to the vibrational and electron energy losses occurring in nitrogen, leaving it to remain in a liquid state whereas in argon inelastic losses from electronic excitation are not possible in the liquid and so energy more readily contributes to ionisation and the onset of avalanche [53]. These values are said to represent the measured minimum electric stress at the needle tip to cause electron avalanche into the liquid.

5.2.1.8 Electrohydrodynamic effects

In addition to the electronic process outlined, it has been proposed by Lewis [127, 128] that the Lippmann effect acting in the surface charge double layer could also be significant in the initiation of streamers. The Lippmann effect causes a lowering of the surface tension of the liquid at the electrode-liquid boundary by increasing the intermolecular separation. It is argued that the reduction in cohesiveness provides a small vacuum region at the electrode permitting field emission to begin. The suggestion of using theory from electrohydrodynamics to explain the initiation of streamers is relatively recent and experimental evidence to establish the relative

significance of electrohydrodynamics and electronic processes remains an open question.

5.2.1.9 Positive polarity point electrode

The process by which streamers are initiated from a positive tip are less well understood and conceptualisation of the initiation process remains difficult [101].

It has been experimentally observed that in gaseous hydrocarbons a stable train of low charge Trichel pulses can be initiated, this disappears for higher densities; still less than 10 times the density of the liquid phase. It is hypothesised that this is because of the difficulty of finding a seed electron and then initiating an avalanche with the lower mean free paths and smaller high field region [103, 129, 130]. Furthermore it is argued that this situation is similar in the liquid phase [49, 101]. Indeed the breakdown threshold voltage in liquid cyclohexane has been observed to increase two-fold with an increase in pressure from 0.1 MPa to 9 MPa [131]. The consequence is seen that in liquids pre-breakdown events are not very reproducible under applied dc and impulse voltage waveforms [131, 132]. The source of a seed electron to initiate an electronic avalanche process remains an open question with suggestions of supply at the plane electrode[133], or cosmic rays and natural radiation [101]. The suggestion of natural radiation, however, does not satisfy the numbers of positive discharges presented within this study. It is known that the strike rate of muons is approximately 1 per second per square meter of the earth surface, a positive discharge occurs every cycle at sufficiently high applied voltage some 50 times per second and for a very much smaller equivalent area. Another hypothesis suggested is that of a charge double layer at the anode with an applied field, used to suggest the Auger process causing the production of "hot" electrons capable of impact ionization and avalanche toward the anode [128]. Experimental results to support either of these hypotheses have yet to be obtained. The exact process of initiation therefore remains unknown.

5.2.2 Streamer propagation

Steamers in liquid dielectrics have generally been classified as either "bush-like" or "filamentary". The bush-like streamers have branches that spread out in many directions with many divisions resulting in a dense bush of vapour tubules. By

contrast the filamentary streamers appear in shape as a few multi-strand tubules with well defined branches. There is a common association of bush-like with slow streamers initiated from both a negative and positive point electrodes; and filamentary streamers are associated with fast positive electrode initiated streamers. Although these associations are typical it is of interest that filamentary streamers have also been reported for negative tip discharges in liquid nitrogen. They have been reported under streamer initiation conditions from a very sharp tip ($r < 1\mu m$) [102] and also for step impulse voltages (200 ns x 540 μs) for tip radii of 1μm [54, 55, 134]. The probability of a filamentary growth from the negative tip is dependent on, and increases with, applied voltage [55]. It also appears that the filamentary streamer grows out of an initial bush-like streamer. However it is more common for slow bush-like streamers with a velocity of approximately 100 m s^{-1} to be initiated from a negative tip in liquid nitrogen. For positive polarity tip both bush-like and filamentary streamers have been observed in liquid nitrogen, as is common amongst dielectric liquids [50]. The positive bush-like streamers have a similar propagation velocity to negative polarity, however the positive filamentary streamers have a velocity of up to 30 km s^{-1} [50].

It has been observed experimentally that various propagation modes can be induced within the same liquid and for the same polarity ranging from a slow bush-like shaped streamer (subsonic mode 1) to a fast filamentary streamer, velocity above 1 km s^{-1} to a very fast filamentary streamer, velocity above 100 km s^{-1} (supersonic, modes 2 to 4) [135]. The change from one propagation mode to the next is not gradual but rather dependant on exceeding a threshold electric stress. That is it is seen to be dependent on the tip radius and applied voltage [50]. In LN_2 under a square wave impulse (40 ns rise and fall time) for a small inter-electrode gap (3.2 mm) one mode has been observed for negative streamers and two modes for positive [50]. However other studies have shown two modes for each polarity [54, 55, 102, 134]. The results of this study for LN_2 under an applied ac voltage are in agreement with these observations. The propagation modes are understood to require different physical mechanisms and these are discussed in the following section.

5.2.2.1 Negative polarity point electrode – subsonic mode

The electronic process proposed for streamer propagation relies on field emission of electrons by Fowler-Nordheim tunneling at the electrode and the acceleration of the electrons in the applied field to cause ionisation of liquid molecules releasing further electrons and leading to an electron avalanche; the swarm parameters of which have been estimated for LN_2 and are found not to be dependant on hydrostatic pressure and thus are understood to occur in the liquid phase. As discussed the localised energy injected by electrons in this mode from a negative tip generates a microbubble from which a streamer can initiate.

The process for propagation of the negative streamer by electronic processes can be conceptualised as follows. Once the microbubble is induced electrons are injected into the vapour phase from the needle tip electrode and are accelerated by the applied electric field. Electron avalanche in the vapour phase results. It is observed that pressure has a large effect at this stage indicating that the discharges recorded are into the vapour phase [101]. Electron mobility is greater than the propagation velocity of a vapour/liquid interface. Electrons are accelerated into the liquid at the bubble wall opposite the tip and cause a local energy injection resulting in a density change to form another region of vapour ahead of the existing one. The vapour region can be thought of as a bubble coalescing with the existing bubble to form a vapour channel or streamer. Additional electrons reaching the streamer head propagate the streamer into the liquid further. Such a process will extinguish when the breakdown strength of the channel exceeds the voltage along it. Indeed experimental results confirm a correlation between streamer length, propagation velocity and applied voltage. The current and emitted light are constituted of short pulses (<ns) and the amplitude and spacing increase as the streamer propagates. An increase in pressure reduces the stopping distance of the streamers whilst not modifying the velocity of propagation [103]. These observations are used to support the hypothesis that the discharges are occurring in the vapour phase.

Recorded current and light pulses in LN_2 support the concept of a stepwise propagation into the liquid. Current and light pulses are recorded during the bush-like streamer propagation. It has been found that the current pulse leads the light

emission in bush-like streamers by 40 ns [55]. This has lead to the hypothesis that this may be due to the pumping of electrons, since it is known that the lifetime of the $^3\Pi_u$ molecule state is 40 ns and that light with a wavelength of 337.1 nm is emitted with electron transition to the $^3\Pi_g$ state [50, 55]. This stepwise growth is distinct from filamentary streamer growth from positive points where current and light pulses are not recorded, but rather a continuous light emission occurs. It is argued however by Yamazawa and Yamashita that in their study of fast negative filamentary growth; that recorded current and light pulses demonstrate the process is the same for both bush-like and filamentary growth from a negative tip [55]. The structure of streamers from the negative tip is then defined by the stepwise charge injection processes occurring after streamer initiation.

As the electrons are injected into the liquid toward the plane electrode they are moving away from the region of highest electric stress. With the avalanche process occurring in the tubule of the streamer the distribution of ions and free electrons can lead to local fluctuations in the electric field. If the streamer branches at a point the two streamer tips will both present regions of high stress. The local electric fields will interact to modify the electric stress and within the growing bush-like structure the many branch tips influence the total electric field profile. The total electric field profile will be the result of the conducting streamers with high electric stress at the streamer tips and the external field. Kerr effect measurements in nitrobenzene have shown that streamers are conducting and do modify the electric field [105]. At points within a growing streamer, branching occurs. This may result where the local field causes electrons to be accelerated in directions not aligned with the field lines of the externally applied field. Results presented in Section 5.4.2 show that this can cause branches within a bush-like streamer to grow in directions that spread the bush-like structure as further electrons are injected into the liquid.

5.2.2.2 Positive polarity point electrode – subsonic and supersonic modes

As the results of this study confirm bush-like or subsonic streamers are also observed for a positive tip. The similarity in mode-1 propagation for positive points, slow bush-like structures and accompanying multiple and regular current/light pulses suggests a similar mechanism of propagation to that of negative slow streamers [50]. Liquid is vaporised and this is followed by discharges in the vapour phase,

propagating into the liquid gap stepwise. The initiating conditions for this process remain unknown at this time. However the positive streamer is typically associated with faster propagation mechanisms, referred to as modes 2-4 earlier, producing a different characteristic shape. These filamentary streamers are characterised by fewer branches with more directed paths leading from the needle point out towards the plane electrode as compared with the many fine vapour branches that appear in bush-like, mode-1, streamers. It has been observed both in this study of LN_2 and in hydrocarbons that the faster positive streamer can occur by transition from bush-like propagation [136].

The initiation of a filamentary streamer in point-plane electrode geometry has been found to be dependent on both the applied voltage and the electrode tip radius. There exists a critical tip radius below which it is possible to observe both slow and fast streamer types; above which only fast filamentary streamers will be observed. It is also known that the probability of creating a filamentary streamer increases with voltage. Thus it can be argued that for the filamentary streamer propagation to occur there is a threshold electric stress [50, 132]. Comparison of the electric stress required for 50% probability of initiating a streamer for negative and positive needle tips can be estimated using a hyperboloid-plane tip stress calculation for square wave impulse voltages (40 ns rise and fall time). Counting both bush-like and filamentary streamers, values of 1.4 MV mm^{-1} and 2 MV mm^{-1} have been found for negative and positive tips respectively [50].

Photomultipliers have been used to record the light emission from propagating streamers. In LN_2 as is observed for other dielectric liquids the propagating filamentary streamer is accompanied by a single current pulse [50, 55, 132], and continuous light emission [55]. This distinguishes the filamentary streamer growth mechanism from that of a bush-like streamer where multiple current pulses and light emissions occur [55]. Where a polymer or resin barrier is placed over the plane electrode, it is observed that when the filamentary streamer propagates as far as to reach the barrier surface another current/light pulse will occur and this may repeat several times. These re-illuminations are found to be pressure dependent, not occurring at pressures over 6 MPa in LN_2 [50]. These findings support the idea that these secondary pulses are occurring within the already formed vapour channels. By

integrating light emission over the time for a filamentary streamer growth and several re-illuminations Frayssines and coworkers [50] used spectroscopy to estimate the temperature within the channels. Recording of the spectra showed vibrational and rotational excitations are present for the diatomic nitrogen molecule; and these can be characterised by a vibrational temperature, T_V, and a rotational temperature, T_R, by fitting a theoretical curve to the recorded spectra. By this method temperature of the gas within the streamer was estimated to be 500 K with an uncertainty of 30 %. Their results also suggest that the channels contain slightly ionised non-thermal plasma. For positive streamers in oils it is interesting to note that the addition of easily ionisable additives speeds up the propagation of the streamers, whilst the addition of an electron scavenger has no effect [132, 137].

A spatially resolved spectral study of electron density within positive streamers conducted in transformer oil showed increasing electron densities with increasing distance from the point electrode [138]. It is difficult to be certain of the role of electrons within the positive streamer propagation process. However the evidence gathered to date would appear to indicate that the propagation of the positive fast filamentary streamer is due to an ionisation process. The electric stress at the tip of the filaments is then responsible for driving the process; the local electric stress ionising molecules in the liquid in front of the streamer head, propagating the streamer further into the liquid. Indeed the observed speed of propagation would rule out the process occurring due to the growth of the vapour channel; the vapour channel growth must then be a consequence of the process occurring at the streamer tip [101]. A simple model considering the propagating streamer as a thin conducting plasma filament shows order of magnitude agreement for calculated electron densities within the channel and propagation velocity with experimental results [101]. However the model did not accurately calculate the potential drop along the streamer length; this result may indicate that temperature in the filament would increase over time to allow greater conduction and faster propagation modes to occur. Furthermore the knowledge that pressure does not effect the overall growth length of positive steamers unlike the case for negative streamers would add weight to the argument that the process is one of ionisation into the liquid phase [52].

The idea of the electric stress at the filamentary tip driving the process would also be supported by less branching of the streamer as it progresses across the electrode gap as is always observed; and the possibility of streamers "stalling" when branching reduces the local electric stress. Both these effects have been observed experimentally in this study for positive streamers in LN_2.

5.3 Experimental arrangement

To study the pre-breakdown phenomena in liquid nitrogen an experimental technique has been developed to image streamer activity and synchronously measure partial discharge activity by electrical means [139]. This technique has been employed to characterise partial discharge behaviour in LN_2 composite systems, for a range of pressures, temperatures and applied voltages. For study of partial discharges under applied ac voltages a point-plane system has been used. Point-plane arrangements are used extensively to create a strongly divergent electric field, providing high electric stresses at the point electrode tip at relatively lower voltages than other electrode geometries. In practice a highly divergent field may occur by design due to engineering constraints; or by contamination of particulate matter in a fluid dielectric. Particulate could be within the bulk of the liquid, deposited onto one of the conductors or onto an insulator surface. As discussed streamer propagation length is dependent on the applied voltage and electric stress at the needle tip. This means that for relatively small inter-electrode gaps a stable discharge that does not bridge the gap is difficult to achieve. Total breakdown can result in a large discharge current and severe damage to the electrodes, especially the needle point. A solid dielectric barrier can be used to prevent total breakdown. Various solid dielectrics suitable for use in the cryogenic environment have been used in the following experiments to prevent total breakdown of the gap. The experimental arrangement is shown schematically in Figure 5.5.

For these experiments a sample has been designed and manufactured to support a point electrode suspended below a plane electrode which is connected to the bottom end of the cryostat high voltage bushing, terminating within the LN_2, Figure 5.6. With reference to Figure 5.6; the point electrode is a tungsten needle (1). The tip radii of needles used have been measured before each experimental run and re-measured following an experimental run to compare and examine the erosion of the

tip. The needle tip is positioned below the plate of solid dielectric sheet (2) which has been clamped to cover the face of the plane stainless steel electrode (3). The inter-electrode spacing of the gap to be filled with LN_2 is measured before the experiment is performed and an allowance for thermal contraction mechanical supports of the sample is allowed. Gap distance is then confirmed by optical measurement once the temperature of the sample has reached the desired value for a given experiment.

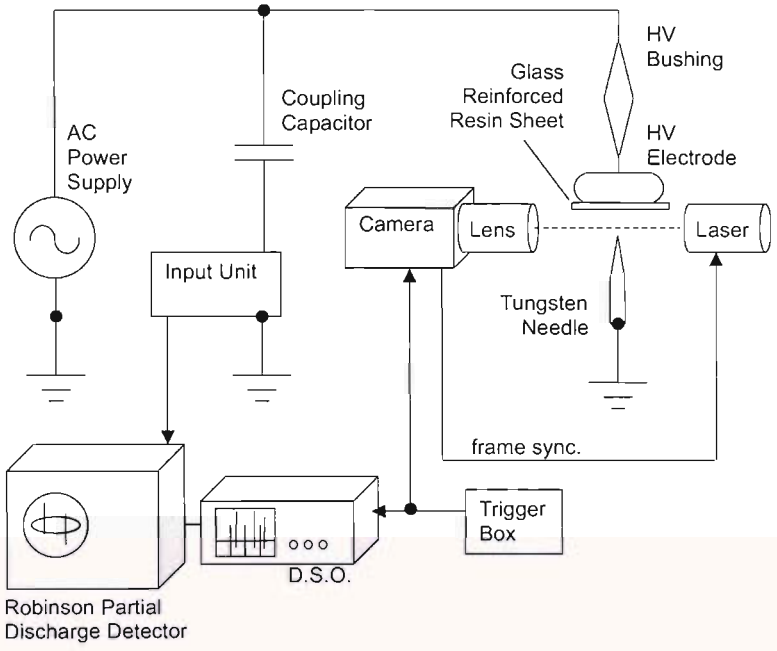

Figure 5.5, Schematic diagram of experimental arrangement

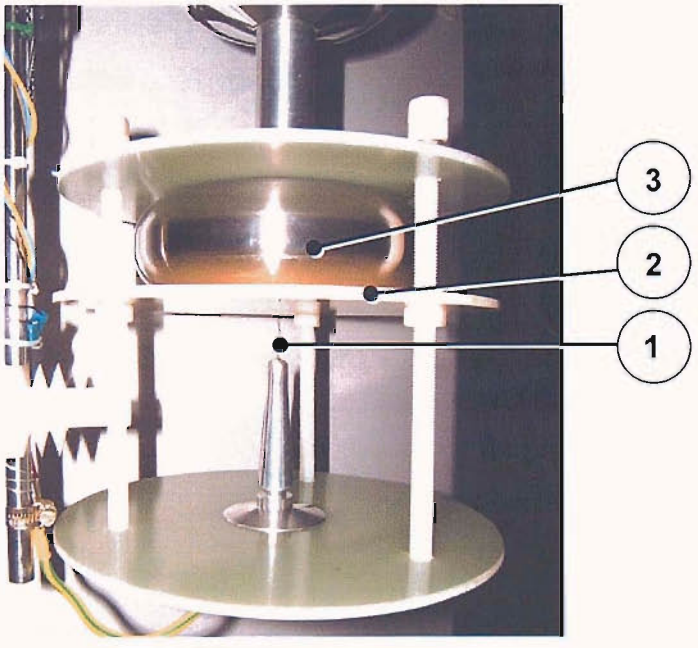

Figure 5.6, Electrode arrangement for point-plane sample with PTFE solid dielectric barrier sheet

For this study of streamers, experiments using three separate solid dielectric barriers in a point-plane electrode arrangement have been performed to characterise the discharge activity in LN_2. The experimental arrangements are summarised in Table 5.1. With reference to Table 5.1, The Tungsten needles used all have an apex angle of 20° and a shank diameter of 1 mm. Tufnol grade 10G/40 is a glass fibre weave impregnated with epoxy resin. Tufnol grade 6F/45 is a cotton fibre weave with 100 by 100 weaves per inch impregnated with epoxy resin. PTFE is a fluorocarbon based polymer, in this case unfilled.

Table 5.1, Details of experimental arrangements

Solid dielectric barrier material	**Nominal barrier thickness (mm)**	**Liquid spacing (mm)**	**Needle tip radius (µm)**
10G/40	4	2.6	2.7 ± 0.4
6F/45	4	3.0	5.0 ± 1.6
PTFE (polytetrafluoroethylene)	3	3.0	5.0 ± 1.6

5.3.1 Calculating point electrode electric stress

Calculating the maximum electric stress at the tip of the needle is difficult for several reasons. Conventionally an expression derived for a hyperboloid to plane geometry is used to solve for electric stress [140]. This assumes that the needle geometry is regular and can be represented as a hyperboloid. The needle tip in this experiment is eroded as discharges occur and so the use of an approximation reliant on perfectly regular hyperboloid geometry becomes questionable. Further to use this expression it is assumed that there is no space charge in the bulk material. It is unlikely that this is the case for this sample, as results obtained show a phase advance observed in partial discharge activity with increasing applied voltages. The characteristic of a discharge current leading the voltage indicates that there is storage of charge in the system, i.e. a capacitance. The phase advance indicates that the effect of this phenomenon is increasing with an increase in voltage. Such expressions are commonly used to provide an approximation for point plane systems, but this is further complicated in this case due to the inclusion of the solid dielectric sheet placed on the plane electrode. Whilst the effects of space charge have been treated analytically by Coelho and Debeau [141] and using FEM by Chen and Davies [142],

this has only been performed for the space charge effects of one material, rather than the composite situation used in this study.

To calculate the electric stress at the tip would require knowledge of the space charge behaviour (volume effects) in the solid dielectric sheet and LN_2 in the gap, in addition to surface charge behaviour on the solid dielectric sheet. In addition a dynamic model would be required for the ac voltage applied in the experiments reported here. Such a comprehensive model would be complex and results may not be reliable for the experimental conditions studied. Therefore results are presented with reference not to electric stress, but referenced to the applied voltage.

5.3.2 Phase correlated imaging technique

A technique for time-correlated measurement of apparent charge and images of streamers in LN_2 resulting from partial discharge activity has been developed. The imaging of the pre-breakdown phenomena in liquid nitrogen can be approached in two ways. The first is to use an image intensifier to capture the light emitted from the discharge event itself, which has been reported by other researchers [52, 55]. The second method is stroboscopically to backlight the sample as was employed in this study. This allows imaging of the density change streamers, where liquid is turned to vapour in the electrode gap due to electrical streamer activity. By this method the motion of vapour generated in the gap by the initial discharge event can be recorded, at and after the event. The advantage of this method is to allow longer sequences of activity to be recorded.

Before filling the cryostat, the inner vessel was evacuated below 10^{-4} Torr to remove moisture, preventing ice particle contamination of the LN_2. The cryostat was then filled with commercial grade LN_2 and sub-cooled by the cryo-cooler to the desired temperature. With the cryostat temperature and pressure controlled for the experiment a voltage was applied to plane electrode via the cryostat bushing. Discharge signals were then measured using a calibrated Robinson pd detector Type 700 via an input unit. A coupling capacitor, Figure 5.5, is used to couple the pd source to the input unit and removes most of the power frequency noise. The input unit is connected to the low voltage output, ensuring that the pd signal is sensitively and safely measured. The input unit collects the higher frequency pulse signals over

a range of 40 to 80 kHz from the pd event but suppresses the power frequency and lower frequency harmonics.

The output amplifier of the Robinson pd detector was connected to the digital storage oscilloscope (dso) for data capture. The camera and the dso are simultaneously triggered by the trigger box. Since it is not possible to measure the true charge, directly at the discharge site, a standard technique of calibration was used to allow measurement of "apparent charge". Apparent charge is defined as the charge transfer between two electrodes as measured by the external circuit and is proportional to the product of the capacitance of the sample and the change in voltage across the sample due to the pd event. Calibration of the system prior to operation was achieved by injecting signals of known charge into the circuit. The amplitude of this signal was then measured by the pd detector instrumentation and dso to provide calibrated scaling. The dso was configured to store with a sampling rate of 1 Mega samples per second (1Ms/s), i.e. 20000 data points per 50 Hz power frequency cycle (20 ms). The Robinson pd detector amplifier output is used to feed signals to the dso, pd signals obtained at this point are up to 40 μs in duration. The dso can therefore capture each pd pulse transmitted from the Robinson detector by this method without aliasing.

The measurement technique developed allows capture and measurement of apparent charge from the discharge pulses, and this electrical signature can be directly correlated in time to images of density change streamers in the electrode gap. Thus electrical signals can be correlated to imaging of the streamer activity and phase and "apparent charge" magnitude data is obtained for the streamer activity imaged. This allows comparative investigation of discharges occurring at the same or different parts of the applied voltage cycle. The influence of varying temperature, pressure and applied fields upon the resultant density change streamers can also be examined with correlated electrical discharge amplitude. Using this method an extensive study of discharge behaviour for point-plane samples has been undertaken.

Images have been captured at frame rates of 5000 and 30,000 frames per second (fps) using the HG100K CMOS camera. A QM100 microscope lens with a long working distance was used to magnify the density change streamer images. An intense light

source is required at high frame rates to provide sufficient light to illuminate the subject for the effective shutter duration which is very short. Three light sources have been used, the first a 500 W tungsten filament flood lamp, the second was a 50 W focused microscope directional fibre light. For high frame rates the high frequency copper vapour laser with pulse duration of 25-30 ns has been used stroboscopically to backlight the sample. The energy of the light from the laser is calculated here, Equation 5.16, to ensure that no photoelectric effect is present in the experimental results obtained. That is that energy of photons incident on the electrode surface does not exceed the work function of the Tungsten needle and so is not sufficient to eject electrons. The copper vapour laser has wavelengths of 510.6 nm and 578.2 nm.

$$E = \frac{hc}{\lambda} = \frac{6.6262 \times 10^{-34} \times 2.9979 \times 10^{8}}{510.6 \times 10^{-9}} = 3.89 \times 10^{-19} \text{J} \equiv 2.43 \text{eV} \qquad (5.16)$$

This value is less than the work function of tungsten (4.35 eV).

5.4 Typical ac results - streamer shapes

Using the technique developed the partial discharge behaviour in LN_2 has been characterised for applied ac voltages at 50Hz power frequency. Taking the example of the experimental arrangement using a 10G/40 solid dielectric sheet, a typical sequence of discharge and streamer behaviour is shown in Figures 5.7 to 5.9. Figure 5.7 shows the electrical discharge signal captured for one 50Hz ac cycle, Figure 5.8 and Figure 5.9 show the corresponding streamer sequences for the positive and negative half cycles respectively.

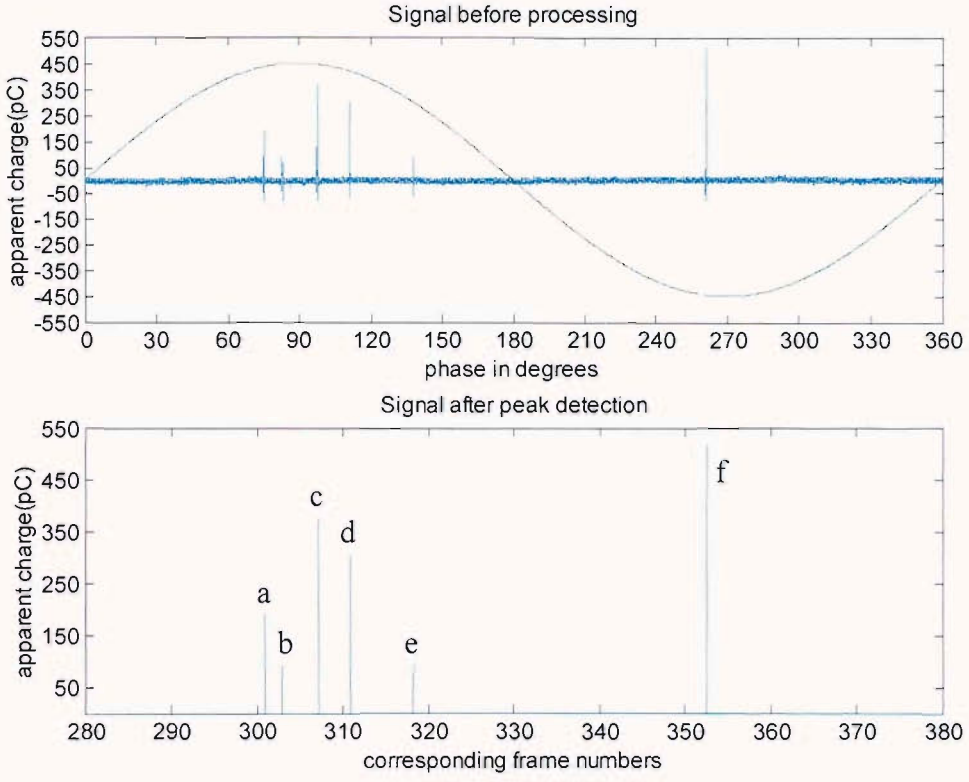

Figure 5.7, Typical result, discharge data at 18.3±0.9 kV, 76±0.5 K

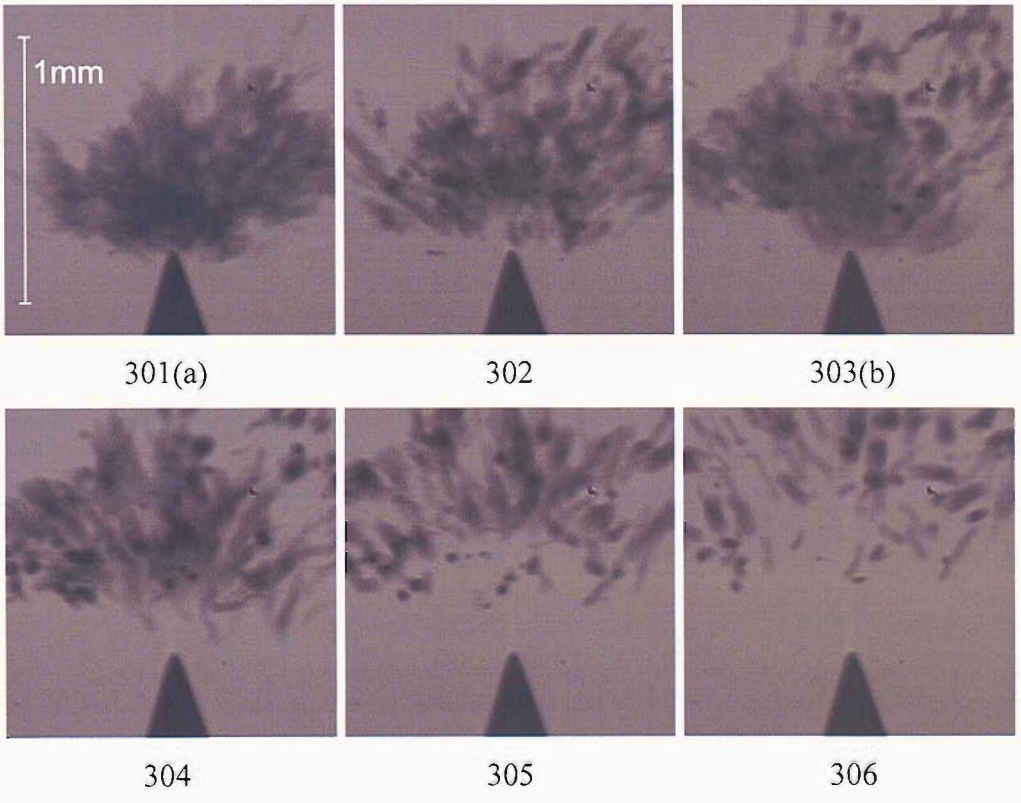

The image sequence continues next page.

307(c) 308 309

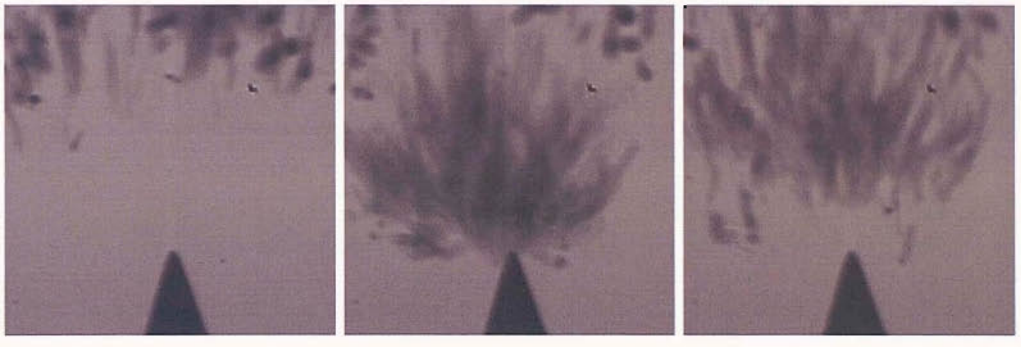

310 311(d) 312

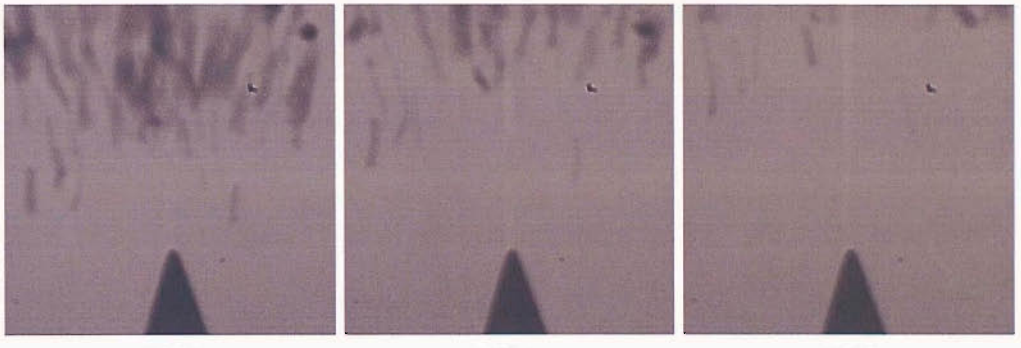

313 314 315

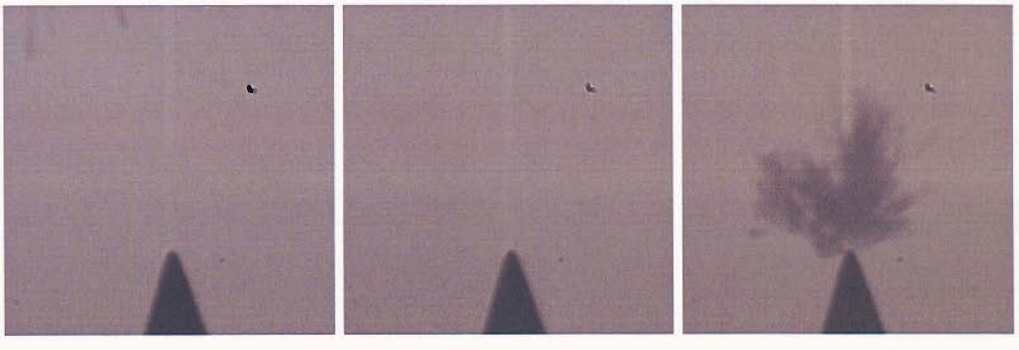

316 317 318(e)

The image sequence continues next page.

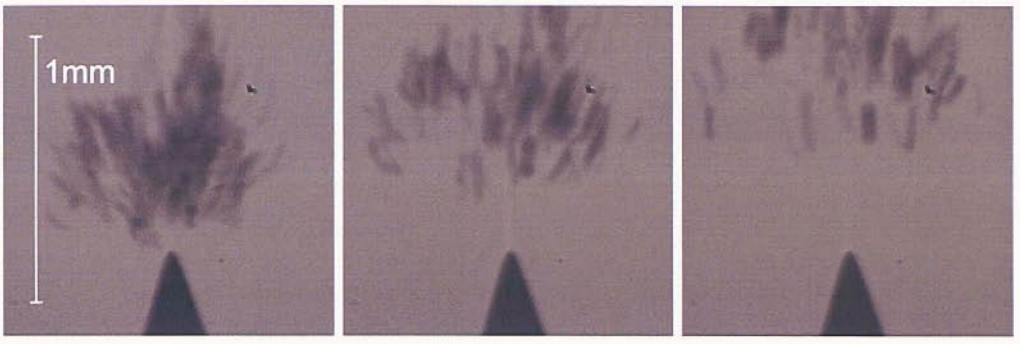

319 320 321

Figure 5.8, Sequence of images showing typical negative tip bush-like discharges recorded at 5000 fps, 1.24 mm frame width at 18.3±0.9 kV, 76.0±0.5 K, frame numbers correspond to Figure 5.7.

Figure 5.8, is a typical sequence of images showing discharge activity causing density change streamers in the positive half cycle, i.e. a negative needle tip with respect to the plane electrode. This sequence illustrates typical behaviour for this half cycle, a discharge occurs and a bush-like like streamer shape is recorded. The vapour produced then rises out of frame and another discharge will occur. Thus bush-like discharges repeat in a series.

Figure 5.9, shows a sequence of images during the negative half cycle, positive needle tip with respect to plane, the partial discharge events recorded for this half-cycle is discharge 'f' shown in Figure 5.7. These images show the vapour resulting from the discharge, at and after the discharge event. A discharge occurs and a streamer is imaged, the streamer vapour column turns to bubbles which then rise out of shot, the speed of the bubbles produces some motion blur; a microscope lamp was used to light this image sequence.

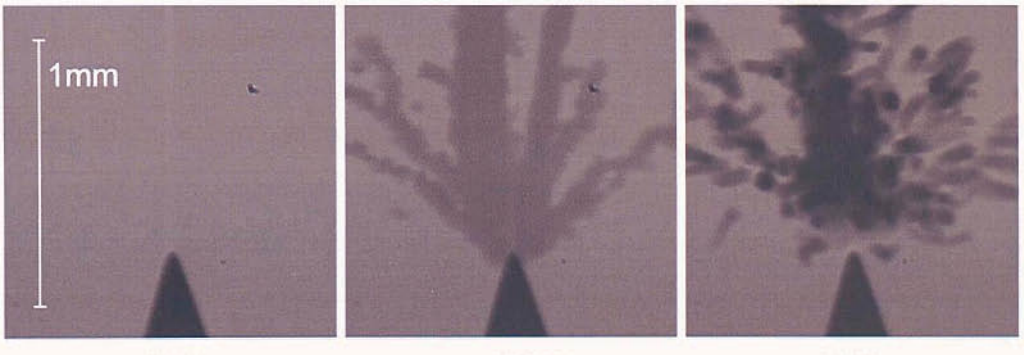

351 352(f) 353

The image sequence continues next page.

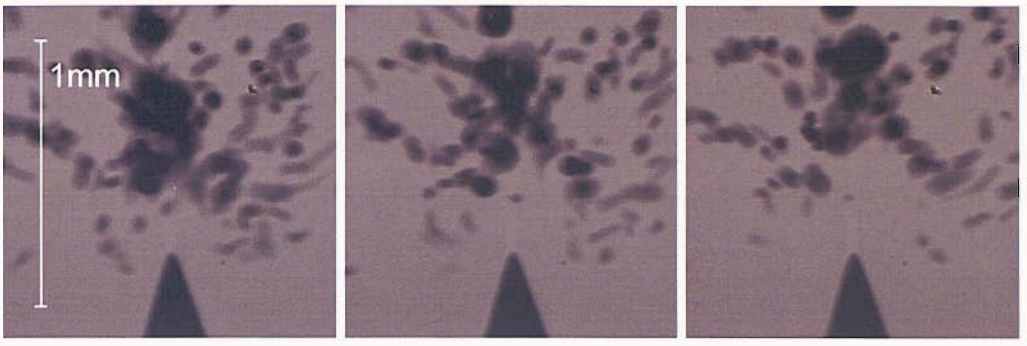

354 355 356

Figure 5.9, Sequence of images showing typical positive tip filamentary discharge recorded at 5000 fps, 1.24 mm frame width at 18.3±0.9 kV, 76.0±0.5 K, frame numbers correspond to Figure 5.7.

5.4.1 Discussion – typical streamer behaviour near inception voltage

Under applied ac stress both characteristic shapes of density change streamers, bush-like and filamentary have been observed. In agreement with [56] it is observed that the negative tip discharges are more frequent than the positive. Bush-like streamers are very common in the positive half-cycle, i.e. when the needle tip is negative with respect to the plane electrode. The bush-like streamers are characterised as having many more branches which are thinner and form more complex branch structures with many offshoots and without a dominant direction (for example see frame 303 and 318, Figure 5.8). The bush-like streamers have also been observed to occur from a positive tip, although this event can be described as rare. Above the inception voltage, defined as the minimum voltage required to cause discharge activity to initiate, discharges will occur for every cycle while the tip is negative. Multiple bush-like discharges will be observed in one half-cycle. Larger bush-like structures with extended shapes have also been observed to occur from a negative polarity needle tip.

Bush-like streamers are very common. By contrast when the polarity reverses, i.e. negative half-cycle when the needle tip is positive with respect to the plane electrode the initiation of positive streamers is irregular and may not occur at all. For 18.3 kV the voltage recorded in Figure 5.7, filamentary streamers do not occur every cycle; if a discharge is initiated only one streamer is observed per cycle at this voltage. Positive filamentary streamers appear in shape as single or multi-strand discharges

with well defined channels along the discharge paths (for example see frame 352, Figure 5.9). There is typically one or two main paths directly from the needle tip toward the plane electrode barrier, these may be accompanied by short side channels also characterised as direct paths with well defined edges. Furthermore, for an applied voltage of 18.3 kV the recorded positive partial discharges appear to be of a higher apparent charge magnitude compared to negative tip partial discharges.

5.4.2 Streamer behaviour – voltage effect

The effect of increasing the voltage from 18.3 kV to 26.4 kV on the streamer shape for the same sample arrangement and temperature is shown in Figure 5.10 and Figure 5.11.

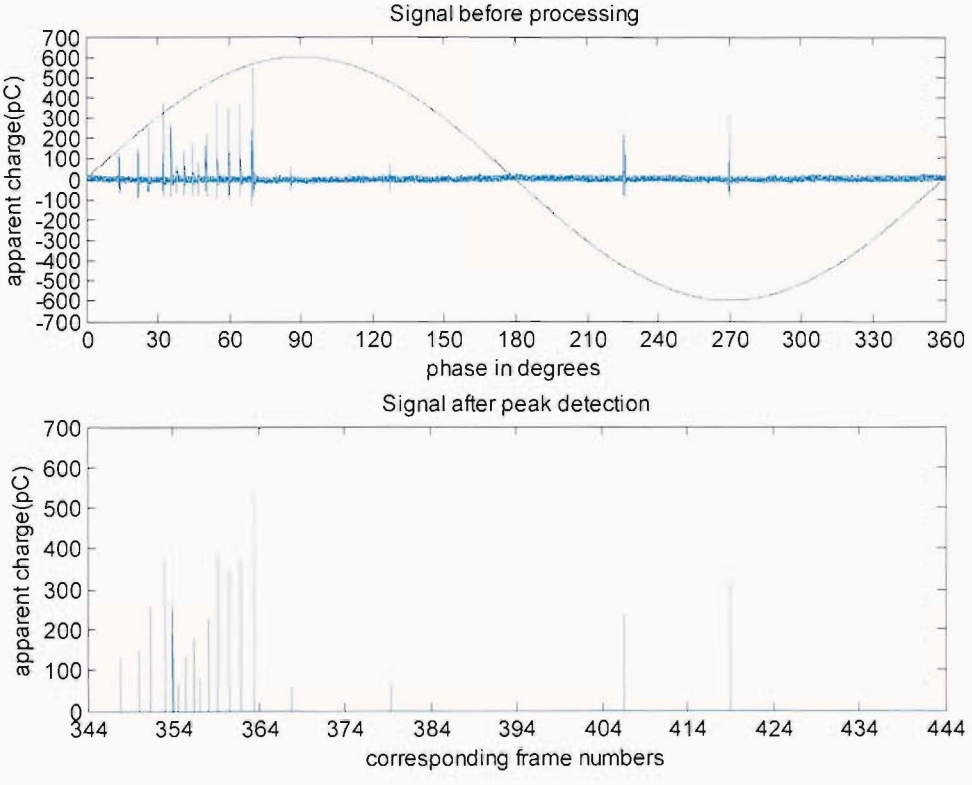

Figure 5.10, Discharge data at 26.4±0.9 kV, 76±0.5 K

346 347 348

349 350 351

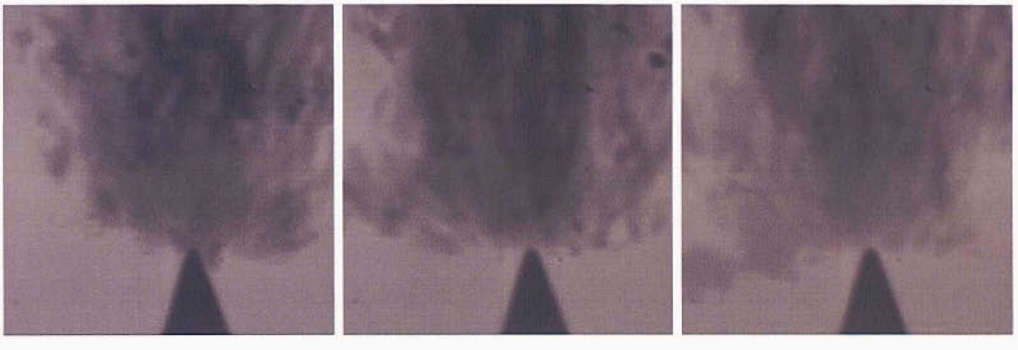

352 353 354

355 356 357

The image sequence continues next page.

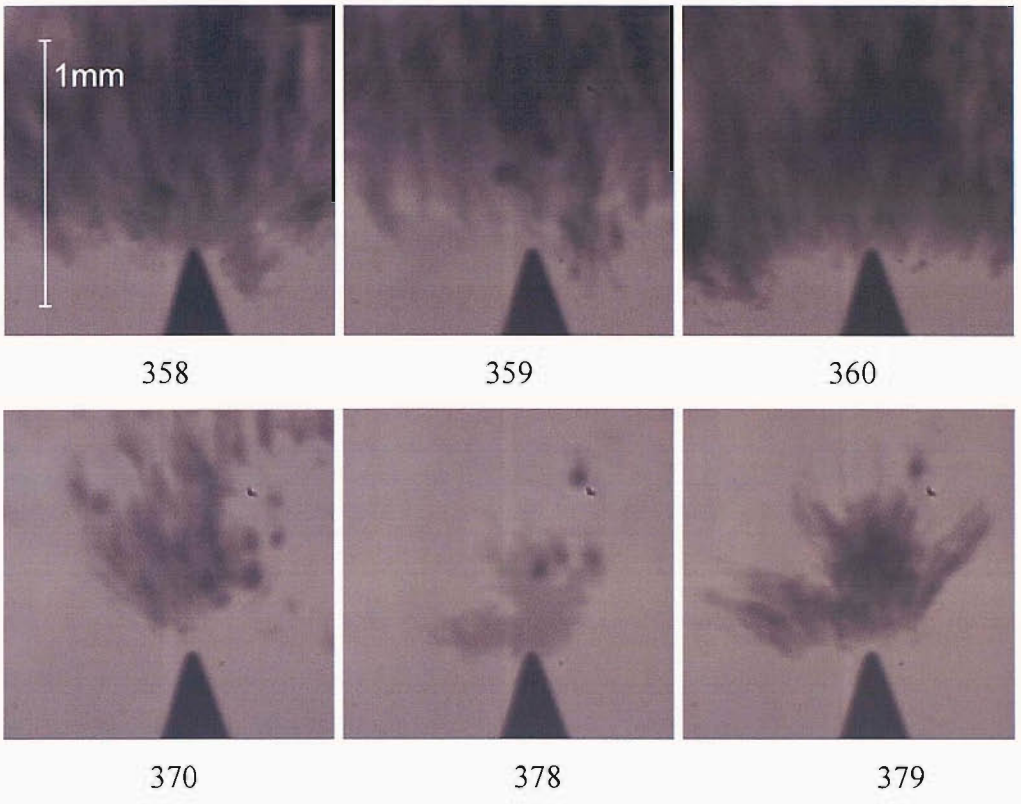

Figure 5.11, Sequence of images showing typical negative tip filamentary discharge recorded at 5000 fps, 1.24 mm frame width at 26.4±0.4 kV, 75.7±0.5 K, frame numbers correspond to Figure 5.10.

5.4.2.1 Negative bush-like shape

Discharge events seen in the sequence presented in Figure 5.11, show that the discharges occur repetitively. In the early frames 347-367 the discharge is continuous and the vapour from a discharge does not lift very far off from the needle tip before the next discharge occurs. Later in the cycle, frames 369 and 378 show bush-like discharges recur after the vapour from a previous discharge has lifted away from the needle tip. At this voltage level of 26.4 kV more discharges occur for each positive half-cycle than seen at 18.3 kV, Figure 5.7.

Spreading of the discharge base out sideways from the tip is observed at this higher voltage, this is clearly seen in frames 354, 357 and 360. This is a result repeated by each discharge that occurs as part of a longer sequence of imaged frames; or active discharge period. This may be due to the columbic repulsion of like charge as it is ejected from the negative tip. The charge within the streamer will have an electric field associated with it. As charge is ejected from the tip in the direction of the

external field, straight up toward the plane electrode, the local field will be modified; becoming the sum of the field from the charge within the streamer, previous streamer vapour clouds and the external field. Thus as more charge continues to be ejected it does so away from the high electric stress, in the direction of the electric field, out to the sides. The resulting bush is therefore wider at the base. This hypothesis is supported by observation that spreading only occurs for discharges occurring in rapid succession during longer periods discharge activity.

5.4.2.2 Negative filamentary shape

The negative filamentary discharge has rarely been reported for pre-discharge studies and it would appear to be peculiar to liquid helium and liquid nitrogen [54, 55, 102]. For this experimental arrangement with a 10G/40 dielectric sheet and an applied voltage of 26.4 kV a negative filament discharge has been observed twice out of 892 negative discharges within the 50 ac cycles imaged in this study; these are shown in Figure 5.12. None occurred for the sequence captured at 18.3 kV.

1766 (668pC, 80°) 2464 (490pC, 77°) 2465

Figure 5.12, Selected images showing negative tip filamentary discharge recorded at 5000 fps, 1.24 mm frame width at 26.4±0.4 kV, 75.7±0.5 K

It is seen from Figure 5.12, frame 2464, that the light emission from ionisation appears in the liquid phase, before the vapour column seen in frame 2465, the frame also contains vapour from a previous bush-like discharge. Thus the vapour results from the ionisation process in the liquid phase, rather than occurring into a generated vapour column. This is common to the negative filamentary streamer mode and to the positive filamentary streamer as discussed in Section 5.4.2.3.

Examination of the results using a lens with a wider field of view (FOV) and a higher frame rate of 30,000 fps; for the experimental arrangement using a 3 mm PTFE dielectric sheet and 3 mm LN_2 gap and an applied voltage of 26.8 kV, reveals four negative tip filamentary streamers in 36 of the ac cycles imaged, representing 4 in 1118 partial discharges measured. These are shown in Figure 5.13, from which two shapes of filamentary streamer can be identified. Frames 1498 and 21827 demonstrate a single filament, without branching, very directly connecting between the needle tip and insulated plane. Both of these streamers have occurred after smaller bush-like discharges have occurred; the cloud of vapour bubbles from these remained above the tip when the filamentary streamer propagated through it. This type of filamentary streamer is distinct from the filamentary streamers reported by Yamazawa and Yamashita who always saw a bush-like structure at the base of the filamentary streamer [54]. A similar branch structure is seen to extend down and out away from the main streamer of frame 8096. By contrast the streamers of frames 2037-8 and 8096, which do not totally bridge the gap, have a much more bush-like edge to the main branch, but are clearly separated from typical bush-like streamers by the length and speed of propagation. For comparison frame 21791 is a more typical bush-like streamer but with a single branch on the right of the main bush.

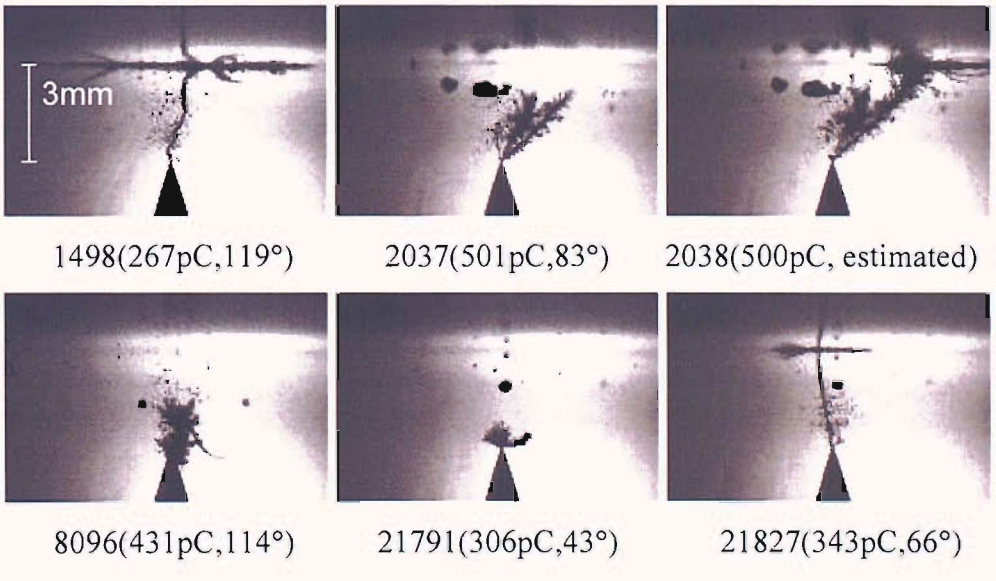

Figure 5.13, Selected images showing negative tip filamentary discharge recorded at 30,000 fps, 3 mm LN_2 gap, 3 mm PTFE, 26.8±0.4 kV, 77.3±1 K

It has been proposed that a filamentary streamer such as seen in frames 2037-8 and 8096 is an extension of the bush-like mechanism, occurring due to a dominance of charge injection in a particular direction, the local electric stress at the tip of the streamer driving further propagation. However the speed and length of propagation would seem to separate the mechanism of the bushy filaments of frames 2037-8 and 8097. Furthermore the filamentary streamers of frames 2037-8 and 8096 are very different in appearance and do not display a bush at their base.

It can be argued therefore that such filaments are propagating by a different mechanism; indeed this must be the case for frame 2464 of Figure 5.12. It would seem appropriate to hypothesise an ionisation into the liquid phase by avalanche stimulated by the larger externally applied field. If such a propagation mechanism can be initiated with a higher field it may be that the bush-like bases seen by Yamazawa and Yamashita and the more bushy filament observed in this study are caused by the onset of the ionisation process near the transition from one propagation mode to the next. Thus a bush may occur leading to filamentary growth as the voltage increases; and a step-wise, ionisation process with bush-like scattering processes along the path may produce the bushy filament streamers witnessed in frames 2037-8 and 8096 of Figure 5.13.

5.4.2.3 Positive streamer shapes

Figure 5.14 shows a typical positive filamentary streamer, at 26.4 kV for the 10G/40 experimental arrangement, recorded during the ac cycle before that of Figure 5.10. At this voltage and frame rate a bright light emission can be imaged within the column of vapour; frame 317.

The vapour column condenses from the needle tip up toward the plane, the tail motion can be seen with motion blur in frame 318, some vapour has broken into separate bubbles. Further close-up images of positive needle tip discharges are shown in Figure 5.15, with frame number, discharge magnitude in pC and phase angle.

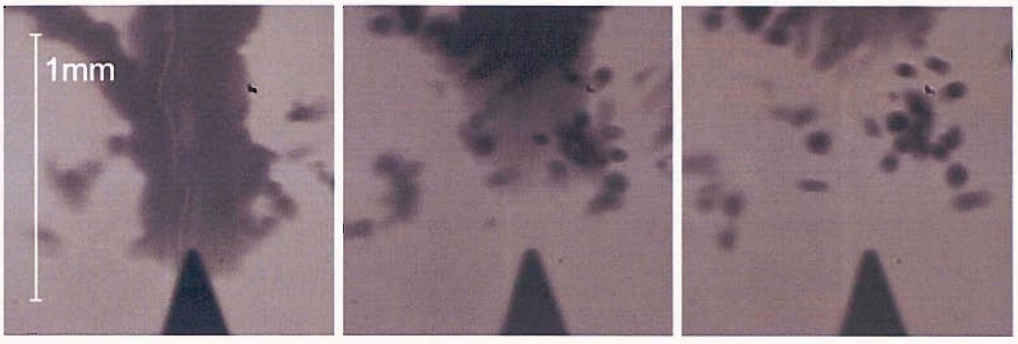

317 318 319

Figure 5.14, Sequence of images showing typical positive tip filamentary discharge recorded at 5000 fps, 1.24 mm frame width at 26.41±0.4 kV, 75.7±0.5 K, 369 pC discharge recorded at 267° phase angle.

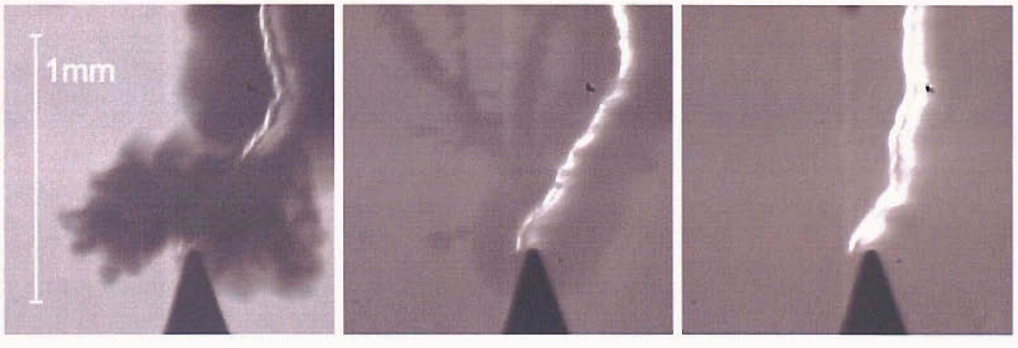

1009 (199pC, 237°) 1109 (263pC, 239°) 1211 (327pC, 247°)

1212 1807 (170pC, 232°) 1913 (163pC, 251°)

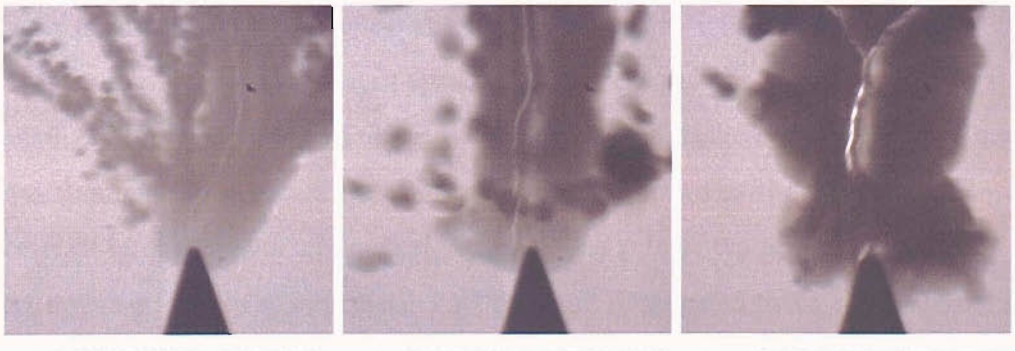

2000 (178pC, 206°) 2105 (234pC, 271°) 2508 (142pC, 233°)

Images continue on the next page.

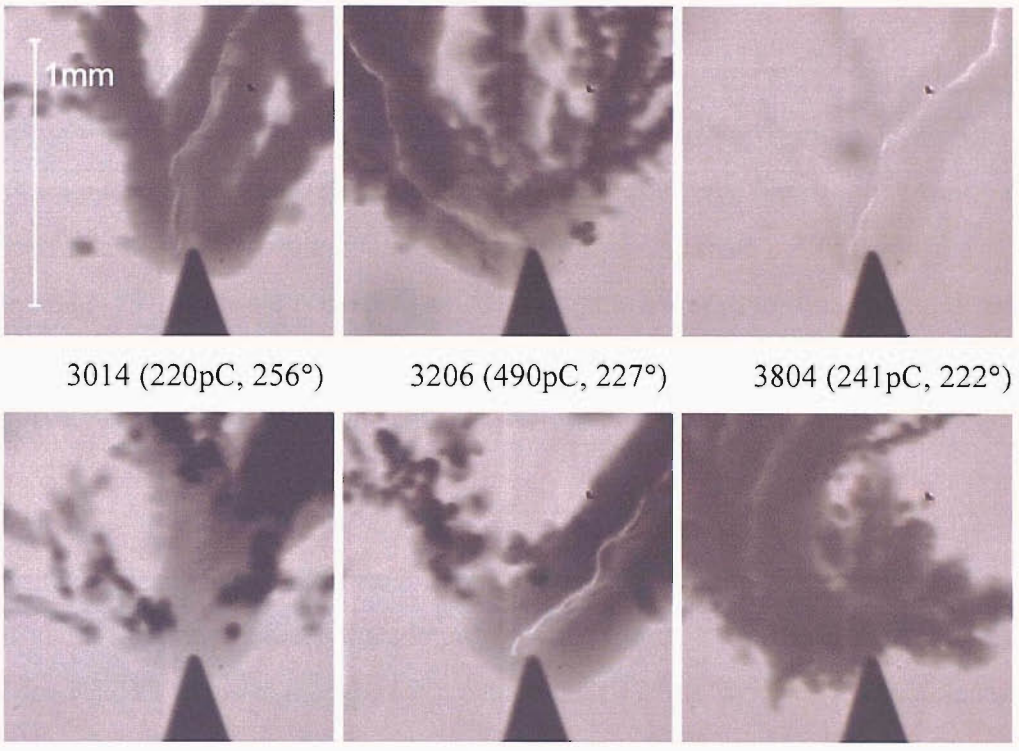

Figure 5.15, Selected images showing typical positive tip filamentary discharge recorded at 5000 fps, 1.24 mm frame width at 26.4±0.4 kV, 75.7±0.5 K

The discharges of Figure 5.15 have been selected for their characteristic filamentary shape. A main filament is visible with some side branches, also with clearly defined edges to the vapour columns. Of interest are the frames 1211 and 1212; these have captured the light emission and subsequent vapour column in separate frames, demonstrating that the vapour results from the discharge producing the light emission. As already discussed the experimental data of other authors has indicated the generation of a plasma column within the streamer. This combined with the evidence of these images leads to the hypothesis that propagation of the positive streamer is occurring by ionisation of the liquid resulting in the generation of conducting plasma. These images appear to have recorded light emission from such a plasma column and it is seen that it is the discharge into the liquid phase that causes the gas filament to form. Closer examination of these frames shows that in the majority of images, the discharge originates to one side of the needle, left of the frame, not from the tip as expected. As this result is repeated there is a preferential initiation at this point, this maybe due to local protrusion of the needle surface causing a local field enhancement.

Frames 1009, 2508 and 4410 of Figure 5.15 and frames 6547, 7181, 15560 and 16145 of Figure 5.16 for a wider FOV; clearly show a bush-like shape at the base of the filamentary streamer, at the needle tip. This confirms the observation of other workers that the positive filamentary streamer may grow from out of bush-like streamers [129]. This supports the use of propagation modes to discuss liquid pre-discharge phenomena; following the idea that streamer shape changes with a change in propagation mechanism which may be determined by the applied voltage or resultant electric field within a streamer.

Using the wider FOV lens for the PTFE sheet experiment a further selection of positive tip filamentary discharges is presented in Figure 5.16 for 26.8 kV and Figure 5.17 for 19.2 kV. This higher frame rate and wider FOV provides a greater clarity in classification of streamer shapes that grow across the total liquid gap.

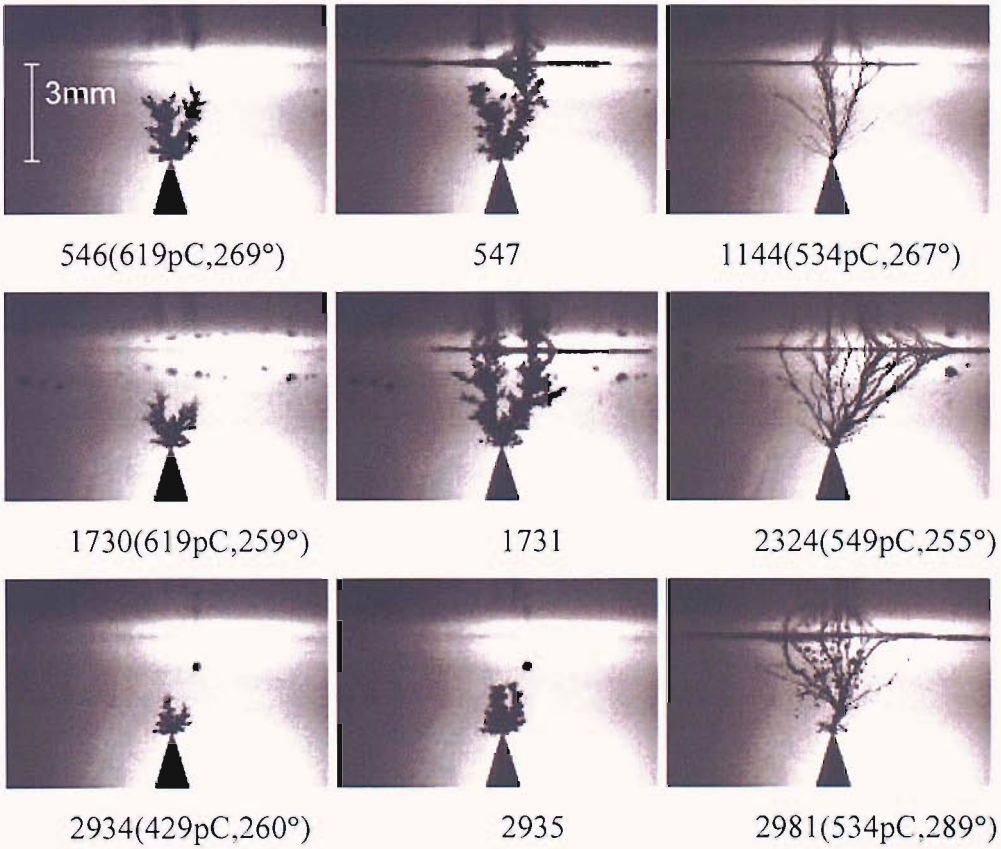

Images continue on the next page.

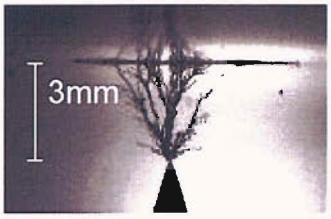

3546(543pC,267°)

4155(547pC,272°)

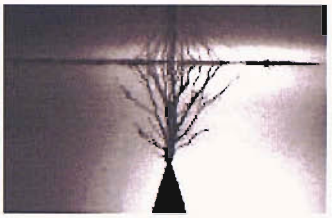

4757(560pC,273°)

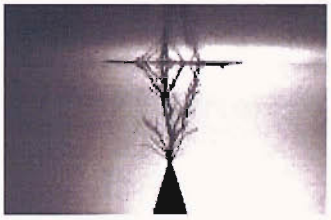

5328(503pC,256°)

5924(462pC,252°)

5964(573pC,277°)

6547(606pC,266°)

7135(350pC,259°)

7136

7180(619pC,286°)

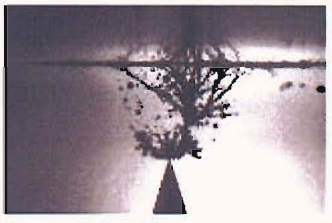

7181

10761(593pC,272°)

10762

11950(671pC,265°)

11951(near 265°)

(it is difficult to discriminate the magnitude of each pulse, 11950/51 and 15559/60)

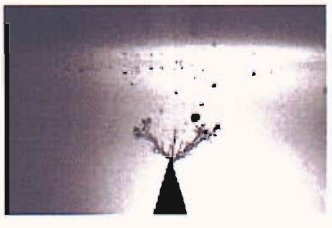

14391(514pC,288°)

15559(632pC,268°)

15560(near 268°)

Images continue on the next page.

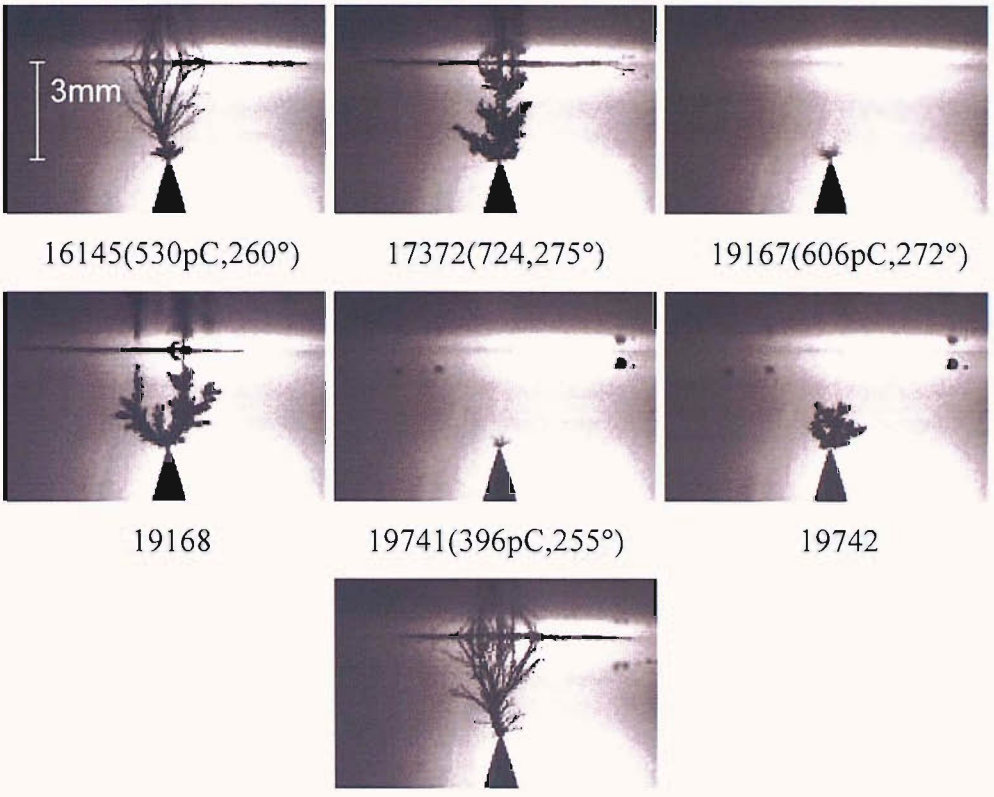

16145(530pC,260°) 17372(724,275°) 19167(606pC,272°)

19168 19741(396pC,255°) 19742

21561(540,266°)

Figure 5.16, Selected images showing positive tip filamentary discharge recorded at 30,000 fps using a 50W microscope focused lamp, 3 mm LN_2 gap, 3 mm PTFE, 26.8±0.4 kV, 77.3±1 K

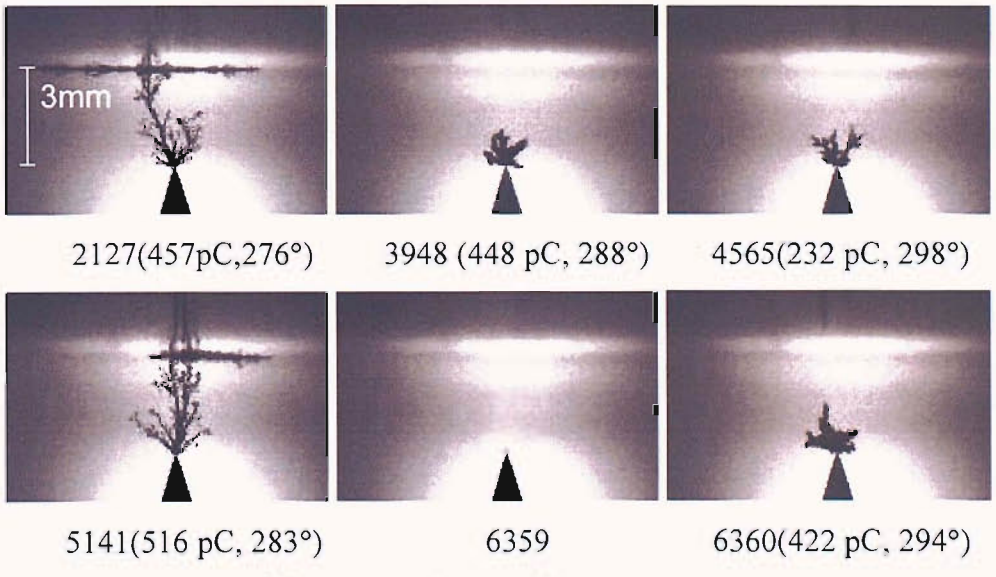

2127(457pC,276°) 3948 (448 pC, 288°) 4565(232 pC, 298°)

5141(516 pC, 283°) 6359 6360(422 pC, 294°)

Images continue on the next page.

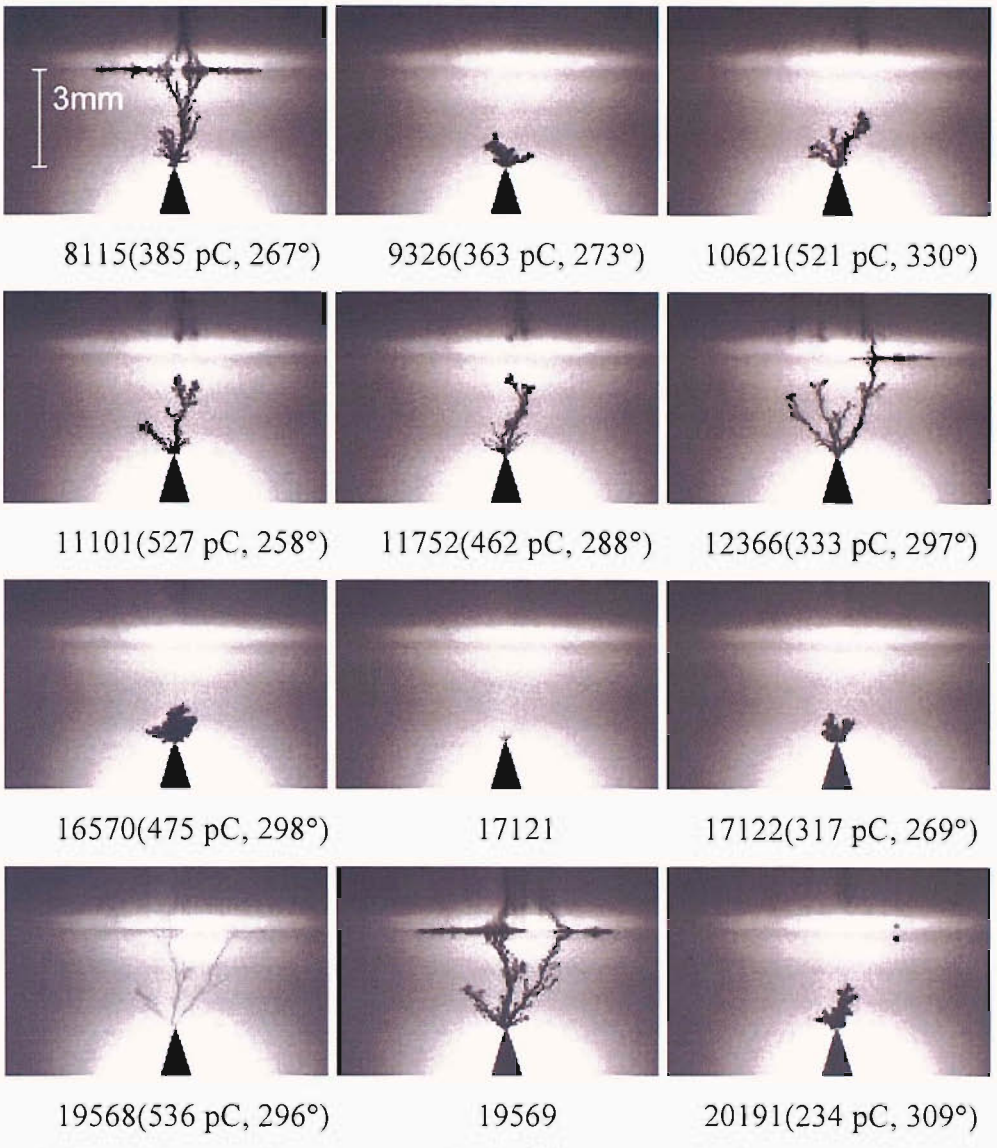

Figure 5.17, All images showing positive tip filamentary discharge over 36 cycles ac; recorded at 30,000 fps, 3 mm LN_2 gap, 19.2±0.4 kV, 77.3±1 K

With reference to Figure 5.17, two distinct shapes are seen in these frames; first a filamentary streamer with clear defined channels from tip toward the plane, for example frames 5141, 8115 and 19568, and second a bushy streamer with more irregular edges for example frames 3948 and 16570. At this voltage, 19.2 kV, no bush-like streamers totally bridge the liquid gap, but many do have prominent branches protruding from the main body, for example 4546, 6360 and 20191. It is also of interest that at this voltage not all filamentary streamers totally bridge the liquid gap. Those streamers that do not bridge the gap appear to have blunt ends. This may suggest that the propagation which has been hypothesised is an ionisation process driven by the electric field stress at the filament tip, may have stalled for

these filaments as stress was reduced at the tip due to branching. An alternative explanation is that there is insufficient voltage to maintain the ionisation process across the gap, since the filament will have a finite conductivity. With the voltage at the tip dropping as the filament grows the stress at the tip reduces and propagation may switch back to a bush-like streamer mode causing small bushes at the tips giving the blunt appearance observed. There is insufficient resolution with the current experimental arrangement to establish with certainty the exact structure at the stalled branch tips.

For 26.8 kV the same distinction of two steamer shapes can be made; first a filamentary streamer with clearly defined channels from tip toward the plane, for example frames 1144 and 2324, and second a bushy streamer with more irregular edges for example frames 547 and 1731. Comparing results for the two voltages for this experimental arrangement there is much greater discharge activity in the negative half-cycle; positive needle tip, at 26.8 kV over that at 19.2 kV. At 19.2 kV a positive streamer does not always occur; of the 36 cycles of data collected a streamer only appeared in 21, representing only 0.417 occurrences per cycle or a 41.7% chance of occurrence per cycle. This is compared to activity at 26.8 kV where there is always streamer activity for every negative half-cycle and sometimes two streamers occur for the same cycle; resulting in a 1.28 occurrences per cycle. Considering the data for bush-like and filamentary streamers from the positive tip no trend is apparent to distinguish the two types by phase or magnitude. Of all positive streamers observed at 19.2 kV, filamentary streamers represent 53.3%, at 26.8 kV this figure rises to 67.4%. This trend of greater probability of a filamentary streamer occurrence with increasing voltage is in agreement with other authors [54, 102, 129].

Visual inspection of Figure 5.16 and Figure 5.17 reveals that the density of the branch structures is greater for both streamer types at the higher voltage. The filamentary streamers exhibit many more branches at 26.8 kV and in contrast to 19.2 kV none are seen to stall, i.e. all bridge the liquid gap. At 26.8 kV some bush-like streamers are seen to bridge the liquid gap, for example, Figure 5.16 frames 547 and 1731, although this does not always occur. By contrast no bush-like streamer totally bridges the gap at 19.2 kV.

It is of note that for the PTFE and 6F/45 samples an EHD fluid motion in the liquid gap occurs above a voltage of approximately 22 kV. This fluid motion in the liquid gap is presumed to be electroconvection caused by the high electric stress of the needle tip. No evidence has been seen to link an influence of the fluid motion to the streamer shape. Indeed fluid motion velocity is estimated to be significantly below that for a propagating streamer [129]. No EHD effect was obvious below 26.5 kV for the 10G/40 sample, although onset was difficult to estimate due to the small frame size used. Motion became apparent at increasingly lower voltages as the LN_2 temperature was reduced, onset was observed to be less than 21 kV at 68 K.

Closer inspection of frames where a filamentary streamer bridges the liquid gap reaching the solid dielectric shows that common to both voltages when the filament strikes the surface there is propagation across the surface. This is evidenced by the vapour generated on the surface, appearing in the frame as a darker horizontal line between the filament and its reflection. It is to be expected that the like charges will not remain at the filament strike point, but will spread across the surface. The weakest dielectric path is at the interface between liquid and solid and the propagation here causes local vaporisation of the liquid.

There are limited images of negative filaments reaching the solid dielectric, for example, frames 1498, 2038 and 21827 of Figure 5.13. When these are compared to the positive tip results of Figure 5.16 and Figure 5.17 it appears there is a difference in surface propagation. The positive surface propagation is limited to a region close to the surface; by contrast for the negative results the propagation appears to lift away from the surface again in further filaments, this is most clear in frame 1498 and the right hand side of frame 2038, Figure 5.13. At this time there is little data, but such a result would be consistent with the conception that for the negative surface propagation an electron avalanche occurs across the solid dielectric surface and the excess of electrons supplied to the surface via the filament may result in further filaments branching into the liquid. For the positive case this does not occur as propagation is by movement of holes, electrons are travelling toward the filament strike zone to fill these, but are limited by the poor conduction of the dielectric sheet and so a similar charge multiplication process can not occur to cause the generation of further filaments into the liquid.

5.5 Summary and conclusions

The pre-breakdown of liquids has been studied extensively and theory relevant to the understanding of the discharge activity within LN_2 has been reviewed. Pre-breakdown within liquid can be evaluated by consideration first of the conditions and mechanisms for initiation and then for propagation modes. Several propagation modes have been reported; observed in a range of liquids. These modes are dependent on the properties of a liquid, the polarity of the applied voltage, the electrode surface condition and geometry, and liquid temperature and pressure. The point-plane electrode geometry is widely used to study discharges within dielectrics, liquids, solids and gases. In liquids this may be analogous to the deposition of particles on electrodes, within the bulk liquid or regions of high electric stress caused by design; this may lead to the pre-breakdown phenomena characterised in this study.

In LN_2, initiation from a negative polarity tip is known to begin with current pulses and charge injection into the liquid phase causing a local energy injection and the formation of a bubble; further discharge into the bubble then causes streamer propagation. The formation of bubbles and particulate contamination are therefore issues of keen interest to the design and employment of successful LN_2 composite insulation systems in HTS power apparatus. In LN_2, as is common to all liquids, the positive streamer initiation mechanism remains difficult to establish and is an open question at this time.

Streamers within liquids cause vaporisation of the liquid, the resultant change in density and refractive index allows imaging of what are termed density change streamers. An experimental technique has been described that allows simultaneous measurement of partial discharge by electrical detection and correlated imaging of density change streamer behaviour. Streamer behaviour has been studied for point-plane composite insulation systems, with a solid dielectric sheet placed over the plane electrode to prevent total breakdown.

Streamer behaviour imaged in this way has allowed the classification of different streamer propagation modes. For a negative tip both bush-like and filamentary

streamer behaviour has been observed. Filamentary streamer from a negative tip is peculiar to LN_2 and LHe, and its manifestation in LN_2 has been confirmed in this study. For a positive tip both bush-like and filamentary streamers have been observed. The propagation mechanisms responsible have been discussed for each polarity and propagation mode in turn. Unique to this study, light emission has been imaged before vaporisation of the liquid, for filamentary streamers from both positive and negative electrodes. This result reinforces the idea that ionisation processes occur within the liquid phase to propagate filamentary streamers prior to the vaporisation of the liquid. To allow further understanding of the pre-breakdown behaviour in LN_2, discharge activity for a range of voltages, temperatures and pressures has been characterised, this is the subject of the next Chapter.

Chapter Six

Partial Discharge Characterisation in LN_2 Composite Systems

6.1 Introduction

There is very little published research into partial discharge behaviour for different composite systems within LN_2. Reported experimental investigations typically employ an artificially created void or bubble. Work performed includes pd within thermally induced bubbles, for example [63, 143] and discharge in air voids cooled to 77 K [144, 145]. Although a significant amount of work has been undertaken to develop understanding of streamer behaviour in liquids, little work has been performed to characterise the pd for streamers initiated into LN_2 for a point-plane electrode system. The comprehensive study undertaken here to characterise the pd of streamers in a LN_2 and solid dielectric point-plane composite sample is therefore significant in this respect.

Using the three experimental arrangements described in Chapter 5, Table 5.1 partial discharge (pd) activity of streamers in LN_2 has been recorded. The pd activity has been characterised using φ q n plots. In this Chapter results are obtained for studies of three parameters; bulk temperature of the liquid nitrogen over the full liquid range,

a range of applied 50 Hz ac voltages and pressure up to 0.4 MPa. The sample arrangements consist of point-plane electrodes with composite LN_2 and solid-dielectric insulation system as described in Chapter 5. The use of a solid dielectric is not uncommon for point-plane samples of this kind with small liquid gaps. The solid barrier was designed into the sample arrangement to prevent total breakdown, however, it also represents a composite system likely to be found in HTS power equipment. Results are therefore significant from the point of view of characterising the pd activity in LN_2 and assessing the influence of the barrier material on the experimental results. Although not the focus of this study, results also indicate issues with the performance of LN_2 solid-dielectric composite insulation systems at cryogenic temperatures. The experiments of this study are for ac voltages and are useful to further understanding of streamer behaviour and make a step toward establishing design criteria for HTS applications.

6.2 Partial discharge signals of streamers in LN_2

To date the characterisation of pd activity related to streamer behaviour within LN_2 has not received much attention. Takahashi and Ohtsuka [146] counted the frequency of pd pulses above a threshold for point-plane systems using a 3 μm tip radius for ac (50 Hz) and dc applied voltage. They found that the positive dc results were too intermittent to provide a reliable result, but observed that the magnitude was almost independent of the gap spacing. Negative dc results were more repetitive, but smaller in magnitude. Results for three liquid gap lengths and varying voltage show that the numbers of discharges have a distribution of magnitudes, there are more low magnitude discharges and above a given level the numbers reduce with a near liner relationship for increasing magnitude. Cumulative numbers increased with applied voltage and reached higher magnitudes. These trends were reversed for increasing gap spacing. Partial discharge for ac voltages with a gap length of 30 mm show that again the negative pulses were greater in number, but were smaller in magnitude than for the positive tip. Increasing the voltage increased the magnitude and the numbers for both polarities. The maximum magnitude of pulses increased from approximately 60 pC to 180 pC, positive tip and from 30 pC to 50 pC, negative tip for applied voltages of 17 kV and 25 kV respectively.

Sumereder, Muhr and Worschitz found that the purity of the LN_2 has an effect on the pd activity [147]. It is reported that the maximum pd level for pure LN_2 reached only 4 pC up to breakdown voltage and that for LN_2 with ice contamination maximum pd magnitude reached 40 pC before breakdown. The contamination was not found to influence the pd inception voltage, V_i. They found that there was no significant influence on V_i with gap distance, however experimental detail of gap spacing is not given in the paper and the gap or gap range may be too small to observe an effect; pd results are only reported for a gap of 3 mm. The greater range of gap spacing reported in [146] shows clear results of gap spacing between 5 mm and 50 mm greatly influencing V_i.

6.2.1.1 Pressure effect on pd in bubbles

Although not for streamer behaviour reports of the effects of pressure on pd in thermally induced bubbles is informative for this work. For bubbles trapped between coils wound onto a fibreglass reinforced resin (FRP) cylinder and an outer cylinder wall partial discharge was recorded at pressures up to 0.2 MPa [63]. At atmospheric pressure discharge activity was recorded in the phase bands of -30° to 80° and 150° to 260°. The phase advance of the discharge current pulses on the applied voltage was explained as charge storage on the surface of the FRP cylinder. The effect of pressure was to retard these activity bands suggesting less charge storage on the sheet, this is to be anticipated as the number of discharges is significantly reduced. The magnitude in both half cycles was observed to be roughly equal in maximum magnitude and this increases from less than 50 nC at atmospheric to 150 nC at 0.2 MPa. Thus it is seen for a bubble trapped between electrodes that the discharge magnitude can increase with pressure. It was suggested that this was due to the pressurization of the gas within the bubble causing a higher V_i within the bubble and therefore higher voltage collapse upon discharge.

Other work has investigated V_i of bubbles rising under buoyancy between two parallel plate electrodes [143]. It was found that pd was initiated within the bubbles. The magnitude of the pd could be modelled with reasonable agreement by assuming spherical bubbles and a scatter in pd magnitude was observed to correspond to a scatter in bubble diameters. V_i decreased with an increase in the ratio of bubbles to liquid in the electrode gap and decreased as pressure increased.

6.2.1.2 Temperature and pressure effect on surface pd

Of some relevance to this study is the case reported for partial discharges onto a FPR surface using sphere-plane electrodes in LN_2, where the effect of temperature on pd activity was considered [148]. Phase and charge magnitude data demonstrated that the effect of reducing the temperature from 77 K to 67 K in atmospheric pressure LN_2 was to reduce the frequency or number of discharges. Little effect was observed however on the maximum magnitude of either polarity, approximately 100 nC, or the phase position of the discharge activity recorded.

A similar experimental arrangement was used to investigate the effect of pressure on surface pd initiated onto 100 μm thick PE film between rod-plane electrodes [149]. It might be expected that a liquid dielectric would display self-healing properties, i.e. that the resilience to discharge would recover as the voltage returns below the inception voltage, causing the inception and extinction voltages to be equal. Results of this study, however, showed that for 60 Hz ac voltages the extinction voltage, V_e, was always lower than the inception voltage, V_i. A pressure increase from 0 to 5 atmospheres (approximately 0.1 to 0.6 MPa absolute pressure) increased the inception by approximately 38% and the extinction by approximately 50%; the frequency of pulses or number were also reduced. Maximum discharge magnitude was recorded for three pressures and for increasing voltages. It was found that the maximum magnitude increased with applied voltage and reduced with applied pressure. By means of comparison with the results of the temperature study [148] an applied voltage of 10.5 kV produced a maximum discharge magnitude of 100 nC, this reduced to approximately 10 nC for a pressure of 5 atmospheres.

6.3 Partial discharge characterisation

Using the experimental arrangements described in Chapter 5, Section 5.3 and Table 5.1, recorded partial discharge data has been analysed using φ q n plotting. The results show that there are common features to partial discharge activity for all the temperatures, pressures and applied voltages investigated.

6.3.1 φ q n plotting

φ q n plots are an effective way to display pd behaviour, clearly relating phase position, apparent charge, and cumulative numbers of recorded discharges. φ q n plots provide a picture of the discharge activity over multiple cycles of applied voltage. The discharge phase location and amplitudes were recorded and cumulative numbers of recurrence in 200 phase windows and 100 charge amplitude windows were calculated.

Within the φ q n algorithm a minimum signal threshold is set to remove electrical noise from the recorded data. Although the sensitivity of the detection circuit is approximately 5 pC a higher computational threshold of 45.5 pC has been used to prevent noise within the recorded data being misclassified as pd pulses, Figure 6.1. The software algorithm steps though the data and for points above the threshold records the highest peak within a "hold-off" period. This period was selected to be 80 data samples, equating to 80 μs. This is also the time allowed between finding one peak in the electrical signal and any subsequent peak, thus setting the effective measurable repetition rate for the discharge signals. Using this algorithm discriminates the pd signal peaks from noise and pd signal oscillations preventing them from being misclassified as discharge events.

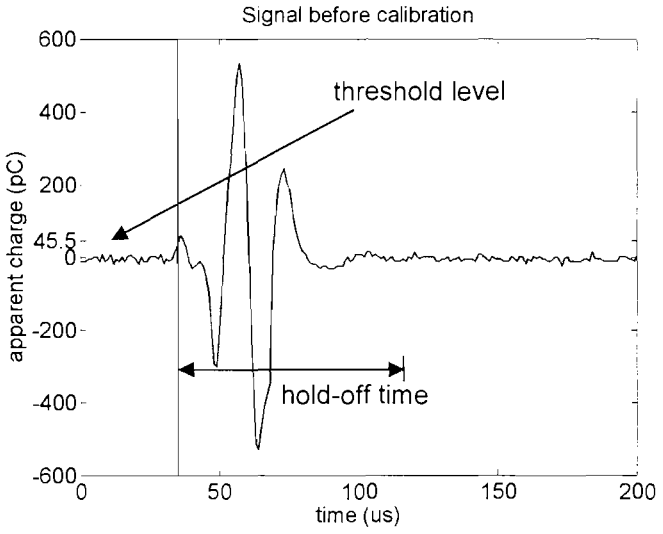

Figure 6.1, Sample pd pulse signal with threshold level and hold-off time shown

Phase measurement error due to zero crossing detection is estimated to be ± 11 μs. Within the φ q n algorithm the pd location will be recorded at the point of maximum amplitude. Since the signal waveform may have a width up to 40 μs the combined error may be up to 51 μs equating to a phase shift of 0.92° representing less than one phase window width of 1.8°. Using this method the error in phase measurement will not significantly alter the φ q n plots for discharges recorded over 200 cycles of applied voltage.

6.3.2 Typical φ q n characteristics

6.3.2.1 10G/40 results

A typical φ q n plot shows the character of the streamer discharges with an applied ac voltage (50 Hz) of 18.3 kV over 200 cycles, Figure 6.2; this Figure corresponds to the streamers imaged and reported in Chapter 5 at a voltage of 18.3 kV just above the pd inception voltage of 17.3 kV. As described in Chapter 5 more activity is seen in the positive half-cycle when the needle is at a lower potential to the plane electrode. This again demonstrates a difference in the mechanisms of discharge for positive and negative tip discharge.

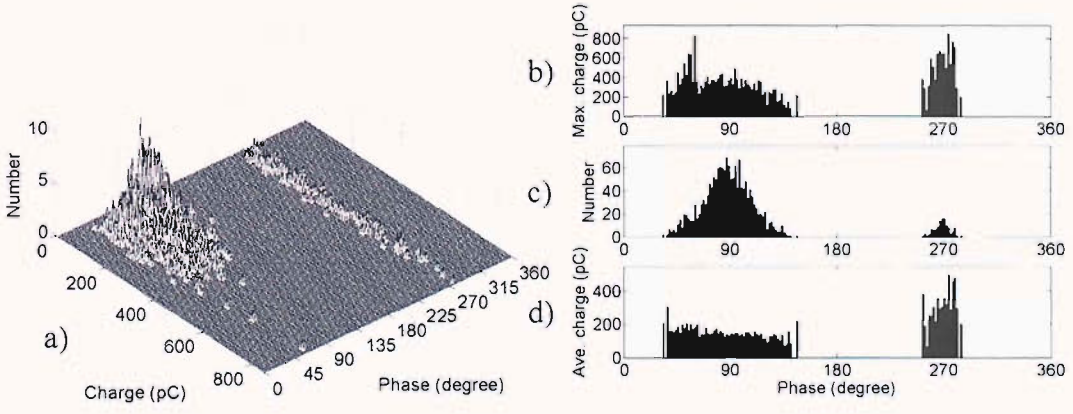

Figure 6.2, 10G/40 sample; 18.3 kV, 76.0±1 K, atmospheric pressure, a) φ q n plot, b) maximum charge, c) cumulative number and d) average charge by phase window

More discharge activity is observed in the positive half cycle, i.e. when the needle is at lower potential than the plane electrode; this is typically the repetitive bush-like discharge and few filamentary streamers, especially near inception voltage i.e. at

18.3 kV for the 10G/40 sample. In general average discharge magnitudes recorded by phase window are greater in the negative half cycle, i.e. when the needle is at a higher potential to the plane electrode. It is seen in the φ q n plots, Figure 6.2 (a), and in the difference between the maximum and average charge plots, Figure 6.2 (b) and (d), that the discharges of the negative tip are typically low with fewer high magnitude events. In contrast the φ q n plots and the similarity in the maximum and average plots for positive tip discharges demonstrate they are typically of larger magnitude than the average negative tip discharge.

Across the active phase bands the maximum pd magnitudes are generally higher for a positive streamer. However the values of the largest maximum pd seen in the positive and negative half-cycle are approximately equal. As discussed in Chapter five it is difficult to prove a link between a particular mode of negative streamer propagation and the measured magnitude of apparent charge. It is clear however, that the pd signal for negative tip and positive tip is different, with the repetitive negative tip bush-like discharges producing a consistent average discharge magnitude over a broad phase range (Figure 6.2 (d)).

There are a few discharge events at both ends of the region that appear to attain a higher magnitude than average and the average tails off later in the half-cycle, sometimes with a few very late discharges managing a greater apparent charge magnitude. Thus it would appear that when a bush-like discharge occurs its magnitude is smaller on average if it follows a previous discharge in quick succession. Where this is not the case, early and late in the cycle, a greater magnitude may occur. In addition the initial discharge will on average be of greater magnitude than the following discharges, leading to the slight bias in the square shape of the positive half cycle toward the beginning of the cycle, for example Figure 6.2 (d). It may be hypothesised that the free charge injected by one discharge event impedes the propagation of the next. Although no imaging evidence is available to support this concept, this may be because it is difficult to prove by means of a 2D image which does not provide a true measure of the 3D structure density of a streamer or a true picture of the space charge.

6.3.2.2 PTFE and 6F/45 results

Additional φ q n plots showing the same general characteristics discussed for voltages near discharge inception, but for the PTFE and 6F/45 sample arrangements at atmospheric pressure, can be seen in Figure 6.3 and Figure 6.4 respectively. Figure 6.3 and Figure 6.4 for the PTFE and 6F/45 show the same general characteristics as for 10G/40; the distribution for streamer discharge from a negative tip seem a little retarded, located with peaks on 100°, compared with that of 10G/40 at the 90° phase. It appears plausible that this could be due to the higher tip stress of the needle tip for this sample with smaller liquid spacing and tip radius. An advance in phase is seen for higher voltages or higher resultant tip stress. In agreement with this trend the positive discharge activity for the plots of the 6F/45 and PTFE samples, Figure 6.3(d) and Figure 6.4(d), show most positive tip discharge activity is centred about 280°, although a few additional discharges are observed later in the cycle. Again it is difficult to ascertain the cause of this effect, due to the lack of knowledge of the initiation condition of the positive streamer. Conceivably it could be attributable to a higher electric stress at the tip, more readily causing electron scavenging near the peak voltage. For a larger radius tip to cause initiation would require a local field enhancement by space charge effect, charge movement, liquid motion or asperity of the electrode and would therefore be less repeatable.

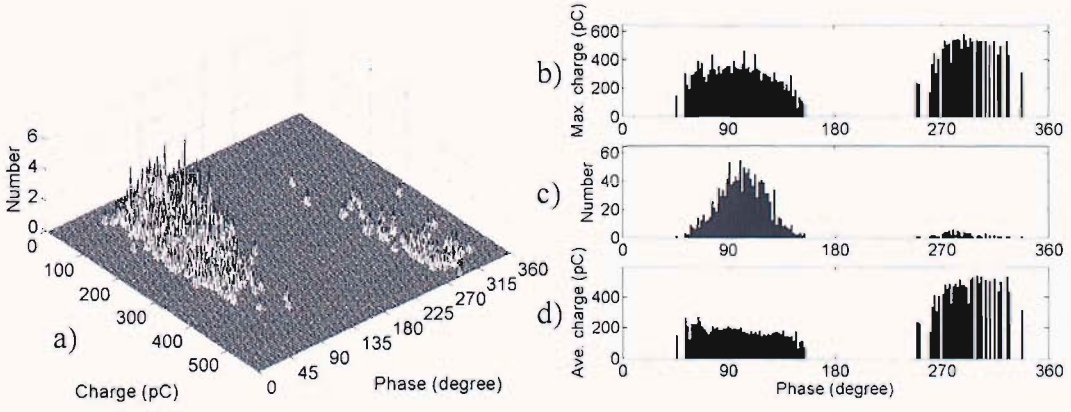

Figure 6.3, PTFE sample; 20.6 kV, 77.3±1 K, atmospheric pressure, a) φ q n plot, b) maximum charge, c) cumulative number and d) average charge by phase window

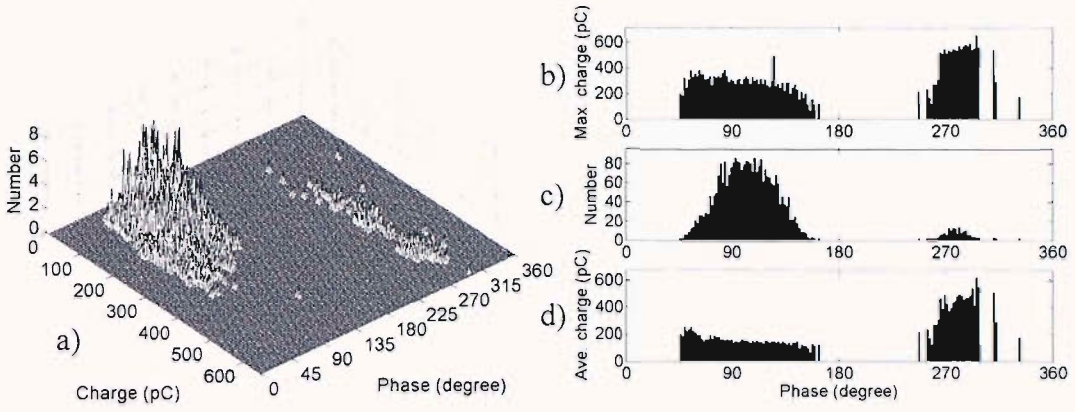

Figure 6.4, 6F/45 sample; 20.7 kV, 77.4±1 K, atmospheric pressure, a) φ q n plot, b) maximum charge, c) cumulative number and d) average charge by phase window

6.3.3 Voltage effect

For the 10G/40 sample the effect of increasing the voltage from 18.3 kV to 26.4 kV can be seen in Figure 6.5. Little effect is observable on the overall regular shape of the average negative tip discharge magnitudes. The active phase band widens and the average discharge magnitude is raised from approximately 150 pC to 250 pC, Figure 6.5 (d).

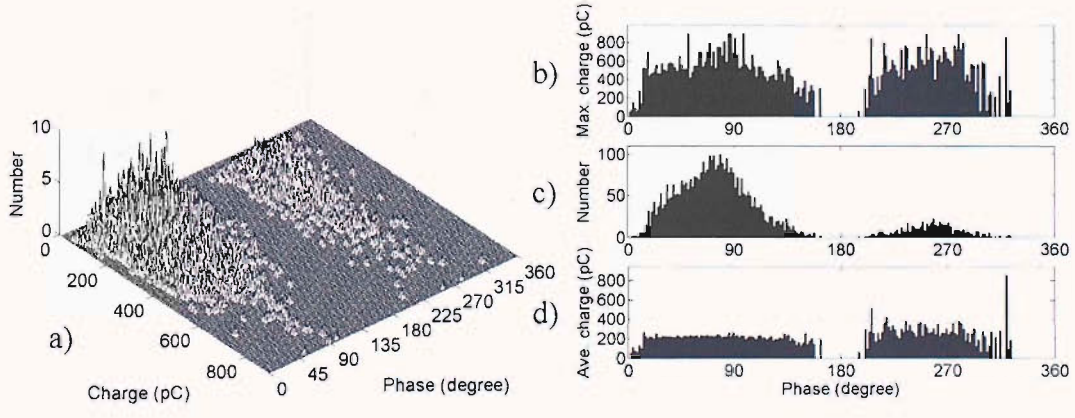

Figure 6.5, 10G/40 sample; 26.4 kV, 76.0±1 K, atmospheric pressure, a) φ q n plot, b) maximum charge, c) cumulative number and d) average charge by phase window

6.3.3.1 Charge storage

At 18.3 kV, Figure 6.2 (c), the activity seen in the cumulative number plot has a peak of 68 and is in the phase window 86.4° to 88.2°. Increasing the applied voltage to

26.4 kV increases the discharge activity and advances the location of the maximum cumulative number to 89 in the 77.4°-79.2° phase window, Figure 6.5. This result is also observed in the negative half-cycle with a phase shift of the peak by approximately 10°. This observation could be due to two possibilities. The characteristic of a discharge current leading the voltage may indicate that there is storage of charge in the system, a capacitive effect. The concept is of a discharge depositing charge onto the solid barrier, which in turn has a field contributing to the total field of the next half-cycle. Therefore, a phase advance seen in partial discharge activity for an increase in applied voltage would indicate that there is an increase in the stored charge in the system with increasing voltage. If this mechanism is in operation it is unknown whether this charge is within the liquid or on the surface of the solid dielectric.

This result resembles that for the reported case of the FRP former in a study of pd in coils [63]. In that case it was argued that the charge would be stored on the surface of the solid dielectric and might be considered a logical proposition here, however it is unclear that this is the only mechanism. Furthermore, as discussed in Chapter 5, it has been seen that when positive streamers reach a solid dielectric re-illuminations occur, indicating a conducting channel and the movement of charge in pulses [52], some charge may remain trapped within the dielectric surface. In Chapter 4 the relaxation time for LN_2 was estimated to be much longer than one period of 50 Hz ac (20 ms); additionally streamer generation involves injection of charge and the charge will have lost its kinetic energy when streamer propagation has halted. It may be conceived therefore that charge may also be stored within the liquid itself. However it is not clear that the results shown are purely a true phase advance.

It is also observed that increasing the voltage has the effect of increasing the average magnitude of charge across the positive half-cycle and widening the phase range during which there is pd activity in both half-cycles. This observation of a broadening of the active phase band could be explained as due to the greater rate of change of voltage for the higher applied voltage. If the inception is a fixed magnitude a greater magnitude and rate of change of applied voltage will result in pd inception earlier in the cycle and a longer period for which the applied voltage is greater than the extinction level after pd inception. These conditions will result in

more charge being injected into the system each cycle and more charge storage by the mechanisms suggested. The relative contribution of each storage mechanism remains unknown. However since the pd activity has not been seen to cross the zero crossing point it is questionable that the storage of charge has a significant influence on the pd behaviour.

6.3.3.2 PTFE results

Considering the voltage effect for PTFE experiments, the results of Figure 6.3 and Figure 6.6, demonstrate similar trends to those for 10G/40. Cumulative numbers increase significantly and the distribution for the positive half-cycle reveals a bell-like distribution. pd activity in both cycles advances in phase and the band of activity widens for the positive half-cycle. For the negative half-cycle the activity has advanced and activity is limited to a narrower band with fewer late cycle discharges separated from the main grouping. It is interesting to note the appearance of the grouping and growth of a peak in the φ q n plot for the positive tip discharge just below 600pC, 270°. A correlation between the measured apparent charge and modes of streamer propagation, or propagation length was difficult to prove from the limited frames captured and discussed in Chapter Five. The full electrical signal data for 200 ac cycles may however be displaying a peak due to the increased likelihood of a positive filamentary streamer and these having a limited propagation length defined by the liquid gap. An increase in probability of a positive filamentary discharge rather than bushy for increased voltages was witnessed in the visual record in Chapter Five and has also been reported by others [54]. If as seems reasonable it is assumed that discharge magnitude is proportional to streamer length, including all branches, then the dielectric barrier represents a limit in propagation toward the high-voltage electrode. Since at higher voltages the discharge is more likely to be of one mode, namely filamentary, and this is more consistent in occurrence and has higher probability of reaching the solid dielectric; a peak arises representing this propagation limit. The idea that the propagation length can be distinguished using magnitude, for a particular sample arrangement, is also supported by noting that the magnitude for the more repeatable negative discharge is limited to below a threshold magnitude. This limit has also increased with applied voltage.

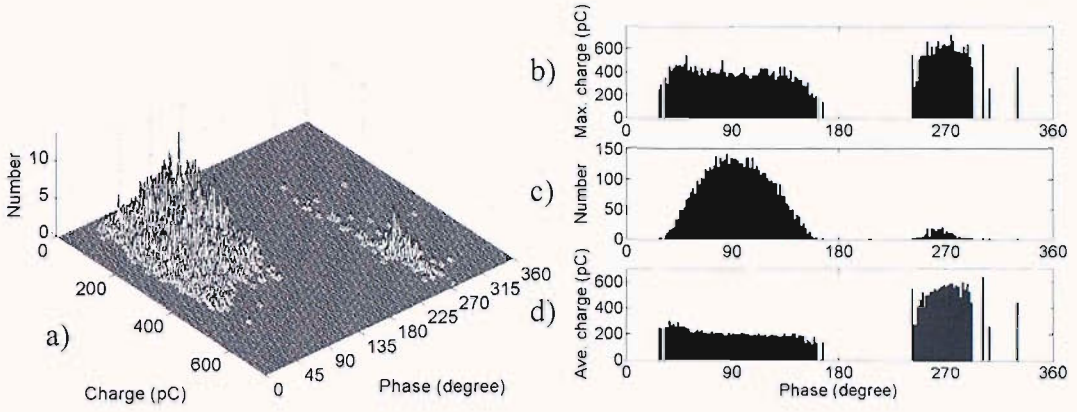

Figure 6.6, PTFE sample; 26.78 kV, 77.3±1 K, atmospheric pressure, a) φ q n plot, b) maximum charge, c) cumulative number and d) average charge by phase window

6.3.4 Partial discharge characterisation, pressure effect

The effect of increasing the pressure from atmospheric pressure (approximately 0.1 MPa) to 0.4 MPa is shown by comparing the results of PTFE, Figure 6.6 and Figure 6.7.

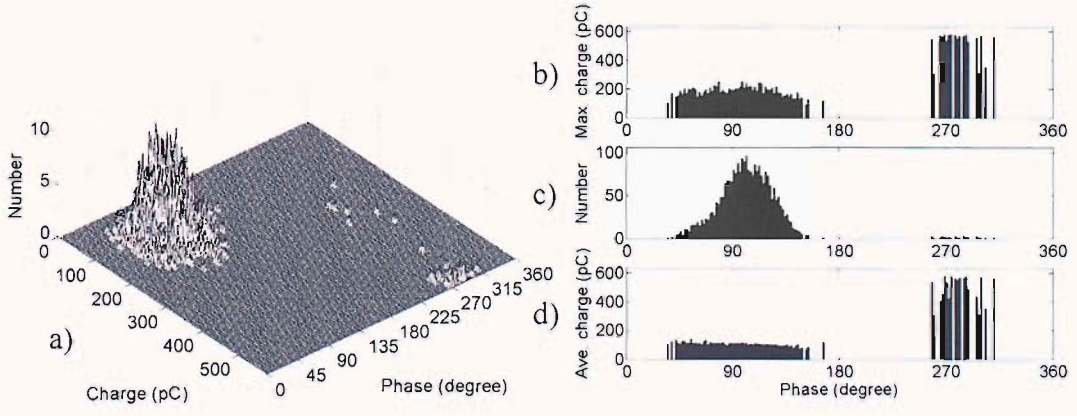

Figure 6.7, PTFE sample; 26.78 kV, 77.3±1 K, 0.4 MPa, a) φ q n plot, b) maximum charge, c) cumulative number and d) average charge by phase window

For the negative tip activity is reduced in numbers from a peak of 140 to 90. The negative streamer discharge maximum and average magnitudes are halved, from approximately 400 pC to 200 pC and 200pC to 100pC respectively. Pressure suppresses the number and magnitude of negative discharges, this is not the case for the positive streamer discharges. Again a grouping of positive discharges occurs just

below 600 pC, 270°. For the positive tip discharges the numbers of discharges have been reduced, but the magnitude is largely unaffected by pressure. This confirms the concept that the positive streamer propagates by an ionisation process into the liquid phase; whilst the negative discharge occurs into the generated vapour phase of the streamer channels. The retardation in phase for both polarities may be due to the elevation of the inception voltage or less charge storage in the insulation system.

6.3.4.1 6F/45 results – voltage effect at elevated pressure

The voltage effect was also examined at an applied pressure of 0.4 MPa for the 6F/40 sample; Figure 6.8 and Figure 6.9. At elevated pressure the data for the positive discharges displays a split in magnitudes with the appearance of two distinct groups by magnitude Figure 6.8(a) and Figure 6.9(a), this is clearer than for the data of Figure 6.7(a). The two groups are overlapped by phase position, but smaller discharges are seen to occur earlier in the cycle for the lower voltage of Figure 6.8. If it is assumed that the magnitude correlates to the propagation length, the groups may represent two modes of propagation, the larger magnitudes a mode 2 or filamentary streamer that bridges the full gap.

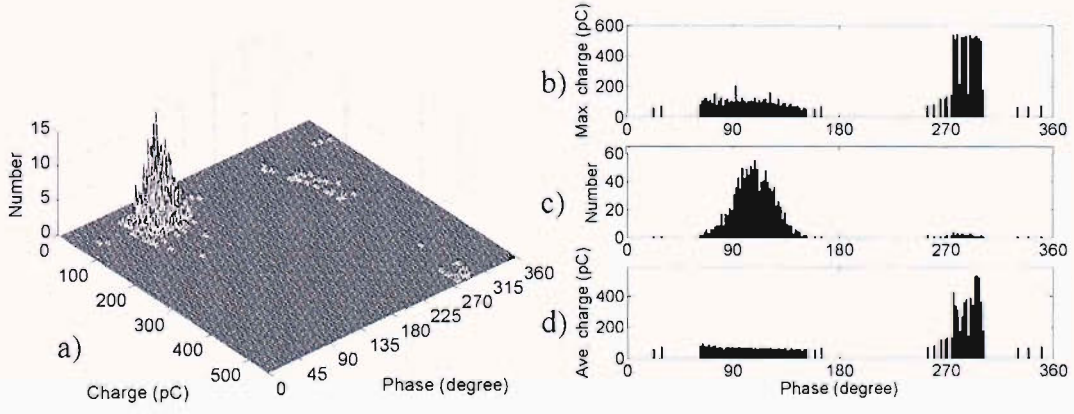

Figure 6.8, 6F/45 sample; 20.7 kV, 77.2±1 K, 0.4 MPa, a) φ q n plot, b) maximum charge, c) cumulative number and d) average charge by phase window

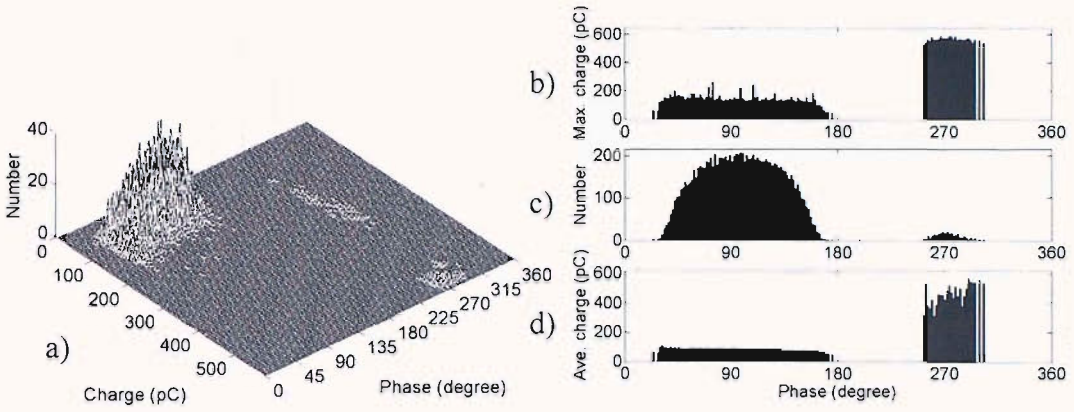

Figure 6.9, 6F/45 sample; 28.0 kV, 77.2±1 K, 0.4 MPa, a) φ q n plot, b) maximum charge, c) cumulative number and d) average charge by phase window

The smaller magnitude discharges may represent mode 1 or positive bush streamers, it is not possible to determine the validity of this hypothesis with certainty since visual data to support these ideas has not been collected. What is known is that for the positive streamers as the pressure is increased less branching occurs and channels are narrower, for examples see Figure 6.10.

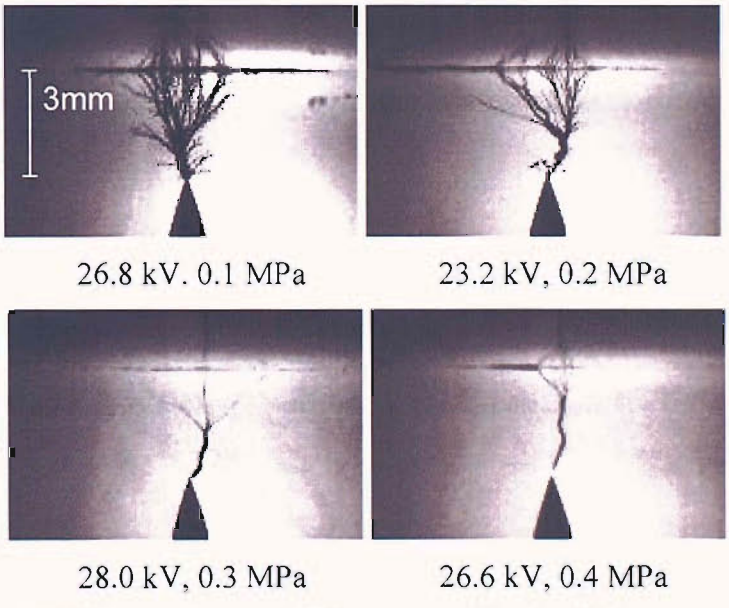

Figure 6.10, PTFE Sample, 3 mm LN_2 gap, positive tip discharge exemplars at elevated voltages and a range of applied pressure

As is the case with an increase in voltage at atmospheric pressure at an elevated pressure of 0.4 MPa increasing the voltage causes an increase in the discharge

activity, characterised by an increase in the band over which there is discharge; a phase advance and increased number of discharges for both half-cycles. There are many more negative discharges with the peak rising from below 60 to over 200 and higher numbers across the full width of the active band. In addition the negative discharges display a similar average magnitude, with higher maximum magnitudes. For the positive tip discharges the activity increase is characterised by the discharges occurring before 270° increasing in number and magnitude. There is a very consistent value of maximum magnitudes at the higher voltage of 28 kV, the highest voltage of all results recorded for any of the samples.

6.3.5 Partial discharge characterisation, temperature effect

The effect of reducing the temperature to 63.7 K has been examined for the 10G/40 sample, Figure 6.11. Lowering the temperature has in appearance similar effects to an increase in pressure. The active pd phase range narrows for both half cycles and the maximum discharge activity and cumulative numbers retard toward the applied voltage peaks, comparing Figure 6.5 and Figure 6.11. This appears to concentrate the activity later in the cycle and sees the maximum cumulative number for this sample, negative tip, of 103 retarded to 91.8°, there is less discharge activity.

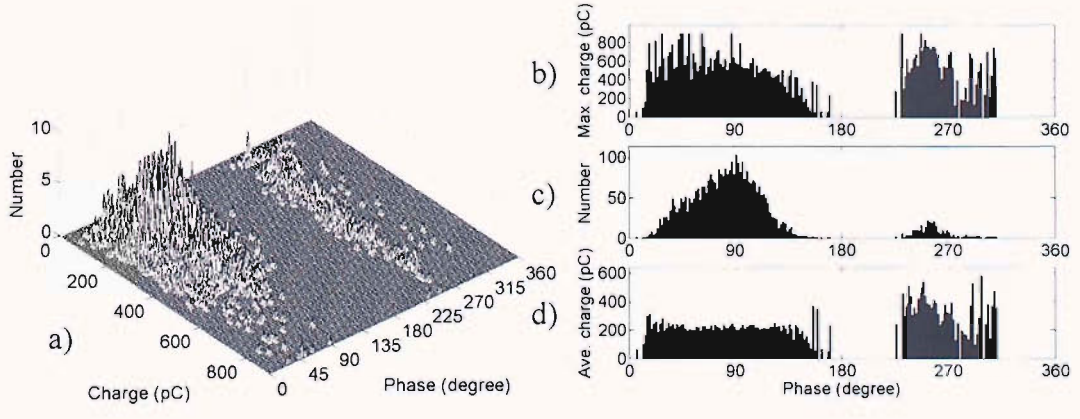

Figure 6.11, 10G/40 sample; 26.5 kV at 63.7±1 K, atmospheric pressure, a) φ q n plot, b) maximum charge, c) cumulative number and d) average charge by phase window

Again for the negative tip the difference, and for the positive tip the similarity, in the maximum and average charge plots show that the positive tip discharges are typically

larger than for negative tip. Reducing the temperature has little effect on the magnitude of the maximum charge or the average charge in the positive half-cycle. The cumulative numbers are lower and the phase band of activity narrows. The similar effect of reducing the temperature and increasing the pressure on the character of the φ q n results indicate that streamer propagation may in effect be more appropriately related to the change in liquid density.

6.3.6 Effect of density on discharge inception

A decrease in temperature from 77.36 K, the normal boiling point LN_2, density of 806.59 kg m^{-3}; to 63.7 K provides a liquid density of 865.12 kg m^{-3}. At 77.36 K and a pressure of 0.4 MPa the liquid density is 806.83 kg m^{-3}. Thus a reduction in temperature to 63.7 K causes a much larger increase in density than application of hydrostatic pressure to 0.4 MPa. It is difficult to obtain a repeatable measure of the inception voltage since as voltage is increased intermittent pd activity may occur before stable and repetitive pd, V_i is also dependent on the ramp rate of the voltage; thus a somewhat arbitrary criterion must be chosen for V_i [150]. For the results presented V_i is defined as the voltage level at which stable discharges are first observed using a Robinson detector. The method used was to increase the voltage manually, estimated to be less than 1 kV per second. Furthermore the sample and needle tip will erode with pd activity and so every measurement made affects the next, which may manifest as dependence in the data set. This makes it difficult to attach significance to the measured V_i. Despite these effects the trends of Figure 6.12 and Figure 6.13 demonstrate the difference in extent of the effect on inception voltage by increasing the applied pressure compared to reducing the temperature. It must be stated that these plots are only sufficient to provide trends, however, and comparison between one sample and the next is not valid without consideration of the tip radius and erosion of the solid dielectric. A Pearson or R^2 test of the fit of the least squares fitted polynomial curve in Figure 6.12 results in a value of 0.9996; for Figure 6.13 this value is 1. This indicates a satisfactory fit to the data when a normal distribution of variance and independence of measurements is assumed.

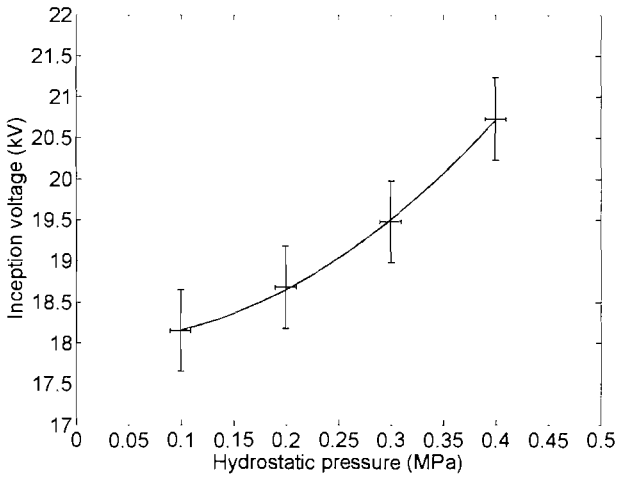

Figure 6.12, 6F/45 Sample, effect of hydrostatic pressure on inception voltage

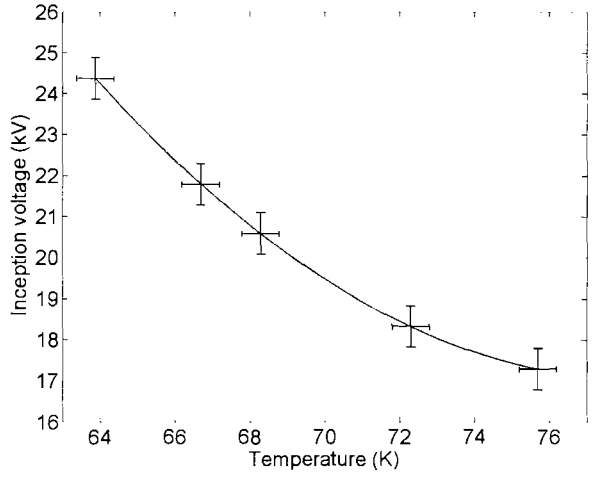

Figure 6.13, 10G/40 Sample, effect of liquid temperature on inception voltage

6.3.7 Needle erosion

As an example the 10G/40 sample the needle was measured to have a tip radius of 2.7 ±0.4 μm a 20 ° apex angle and 1 mm shank diameter. This electrode needle was earthed and positioned 2.6 mm below the 4 mm thick 10G/40 glass-fibre reinforced resin sheet clamped to cover the face of the plane stainless steel electrode connected to the cryostat high voltage bushing. For this sample ac voltage has been applied to the plane electrode at stages between 18.3 kV and 26.4 kV. The tip radius of the needle has been measured after pd activity experiments and is observed to have eroded producing an irregular shape and displays a pitted surface Figure 6.14. A radius measurement is approximated and the tip radius measured to be 15.1 ±0.4 μm.

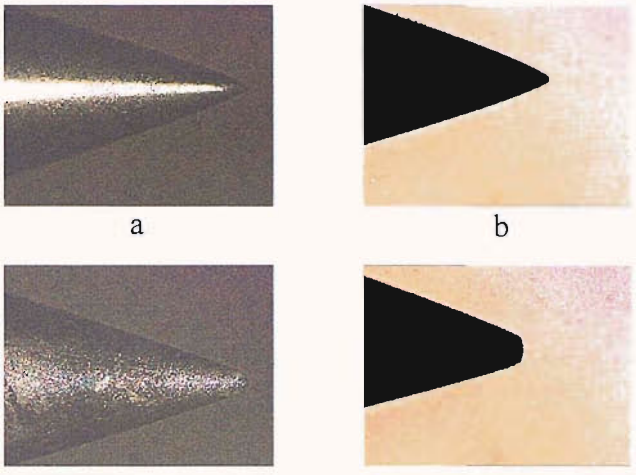

Figure 6.14, Needle tip used in discharge experiments; image size 297 μm by 223 μm, (a) and (b) before, (c) and (d) after

The erosion of the needle tip from breakdown discharge in liquid dielectrics has been studied previously [151]. It was suggested that the material loss at the needle tip is likely due to intense local heating due to high current density during discharge. Other workers studying the generation of a micro-bubbles preceding streamer propagation for negative a needle tip suggest that the shock-waves associated with the bubble collapse causes erosion by cavitation [106]. For the same magnitude of applied dc voltage erosion of needles was found to be more rapid with negative polarity compared with that of positive, and V_i and V_e found to be smaller for the negative tip [146]. In the imaged results of this study the generation and collapse of the streamer vapour channel is observed and can be supposed to cause cavitations for both polarities of discharge. The larger erosion from a negative dc point may suggest that the larger number of discharges may be more detrimental than the fewer larger current pulses of the positive half-cycle.

The erosion of the tip complicates the interpretation of inception voltage results, since V_i increases as the tip radius increases, due to a reduction in the electric stress at the tip. This effect was seen in this study and elsewhere the tip radius was reported to increase by several tens of percent after an hour of discharge [146]. An ideal liquid dielectric would recover after removal of the voltage; and extinction voltage, V_e, might be expected to match V_i. However this ideal is not attained in practice, values of V_e have been reported several tens of percent smaller than V_i

[146]. The change of inception voltage with erosion over time has been investigated for the PTFE sample. After collection of data for the φ q n plots presented above had been completed the inception voltage was measured at 77.4 K, V_i was 21.9 kV, V_e was 20.7 kV. Voltage was increased to 27.0 kV and allowed to cause discharge for a 5 minute period, V_i and V_e were then measured to have increased to 25.5 kV and 23.8 kV, respectively. Another 5 minutes of discharge at 27.1 kV increased V_i and V_e to 25.8 kV and 24.3 kV, a further 10 minutes at 27.3 kV increased these values still further to 27.0 kV and 24.4 kV. Following this 30.7 kV was applied; the magnitude of pd was estimated to be several thousand pC, up to 8000 pC. Total breakdown, puncturing through the PTFE sheet occurred after 3 minutes.

In conclusion it is clear that the needle tip will erode by one of the means suggested, effectively reducing the tip radius and the electric stress at the tip and resulting in increase of V_i and V_e. This means the use of V_i and V_e is an unreliable means of characterising partial discharge behaviour. In addition a dielectric sheet blocking the propagation of streamers will be eroded over time. This was seen for the PTFE sheet, Figure 6.15, where complete puncture occurred resulting in failure of the insulation system under the conditions described. The 10G/40 sample also eroded under the application of streamer discharges, the surface displayed a "burnt" region, a pit where resin has been removed exposing the glass fibre weave and damaging the glass fibre weave to a depth of several layers. No damage was observable on the 6F/40 sample after the experiments performed, but this was not subjected to discharges for periods of similar length to the other samples. Further characterisation of the degradation of insulation systems with duration and magnitude of applied voltage would be required to allow comparison of one system against another.

Figure 6.15, PTFE puncture from breakdown

6.4 Summary and conclusions

Streamers initiated from the needle tip in point-plane electrode system are accompanied by an electrical discharge signal. It has been shown that the use of V_i and V_e values to characterise pd behaviour within a point-plane system is unreliable due to the constant erosion of the needle tip by streamer activity. Thus the pd signal has been captured and analysed using φ q n plots to relate pd magnitude, phase and cumulative number by phase window. Using this tool the pre-discharge activity has been characterised under applied ac voltages for conditions of variable voltage, liquid temperature and hydrostatic pressures. In this manner it has been possible to further clarify the difference in nature between the negative and positive tip discharge behaviour.

Streamer discharges from a negative tip are much more frequent and have a lower average magnitude than for the positive streamers. Near V_i pd activity is centred on 90° and 270° phase. An increase in the applied voltage results in an advance in phase of pd and broadening of the phase over which pd activity occurs. In addition increasing the voltage increased the maximum discharge magnitude and number of discharges.

Streamer behaviour is influenced by an increase in hydrostatic pressure and decrease in temperature. It has been shown that an increase in the pressure or a decrease in temperature narrows the active pd phase band, retarding the phase of pd activity and reducing the number of pd. It is suggested therefore; that the characterisation of pd in LN_2 can be more correctly said to be density dependent. This is consistent with the hypothesis of electronic driven processes where for the negative tip, the mean free path of electrons accelerated by the applied field will be reduced as will the kinetic energy distribution of the swarm resulting in an increase in the inception voltage. This concept also accounts for the reduction in streamer discharge activity and propagation length in the negative half-cycle. It is also consistent with the little observable effect on positive discharge magnitude. The positive streamer is hypothesised as an ionisation process into the liquid phase of the nitrogen.

As discussed that the active discharge phase band widens or that the discharge current leads the voltage is unclear and may indicate either storage of charge within the insulation system or an increase in the inception voltage. Charge might be stored either on the surface of the solid dielectric barrier or within the liquid; the relative significance of these mechanisms is unknown at this time and requires further clarification. What has been observed is the degradation of both the needle tip and more significantly the solid dielectric barrier which is sited to block streamer propagation. It is assumed that this is due to the discharge current; that is the movement of charge in the solid dielectric or across its surface. This damage to solid dielectrics within a LN_2 solid dielectric composite insulation system has significant implications for the design of HTS equipment. The performance of the dielectric material was not the focus of this study and further work to establish the relationship between degradation and streamer exposure would have a practical design benefit.

Chapter Seven

Conclusions & Further work

7.1 Summary

Progress toward operational designs of superconducting power apparatus has been aided by the advent of HTS and the availability of production quantities of HTS tapes. Prototype designs for HTS power apparatus, for example cables, terminations, current fault limiters, transformers and generators exist and many use liquid nitrogen as both coolant and dielectric. For any new equipment to be applied in the field it must be competitive in the market place both in terms of cost and reliability. To achieve these goals equipment design must be optimised. This necessitates good characterisation of the dielectric properties of LN_2 when used for electric and thermal control simultaneously. It has been reported that bubbles have a significant detrimental effect on the electrical withstand performance of LN_2. Thus knowledge of bubble behaviour within electric fields is of interest to HTS power apparatus design. In addition, electromagnetic requirements may need to be traded for lower thermal stress to ensure greater dielectric performance. Pressurising and sub-cooling LN_2 is known to suppress the production of vapour but increases the pressure rating of designs and the refrigeration effort. This will have associated capital expenditure and operational costs. Thus experimental data to allow optimised design of power apparatus is important. It has been the topic of this thesis to experimentally

characterise the dielectric performance of LN_2 and the behaviour of thermally induced bubble dynamics and electrically induced density change steamers.

A LN_2 cryostat has been designed and manufactured to facilitate the experimental study of bubble dynamics and streamer behaviour. The cryostat incorporates a high voltage bushing rated to 80 kV and pd free to 50 kV. Four optical ports permit the imaging of bubble dynamics and streamer growth in LN_2. The cryostat vessel is pressure rated to 2 MPa and controlled temperature across the liquid range of nitrogen is achieved by an integrated cryo-cooler.

7.2 Conclusions from a study of bubble dynamics in LN_2

An experimental study of bubble dynamics in uniform dc electric fields has been conducted. This study is distinct in its focus on the growth and detachment of thermally nucleated bubbles from a single site. Imaging of the bubble detachment showed that the bubbles elongated in the direction of the external field, and contrary to expectation were held on the surface for longer periods. Consideration of the EHD forces acting upon the bubbles leads to the hypothesis that the retaining force is dielectrophoretic and electrostrictive in nature; not Coulombic. This conclusion is drawn from the charge relaxation time having been estimated to be much longer than the detachment period of the bubbles and is supported by the observation of 100 Hz oscillations of bubbles within a 50 Hz ac field; again a period much shorter than the charge relaxation time.

Examination of bubble dynamics in dc fields shows that for both polarities, increasing the field strength increases the bubble aspect ratio and decreases the bubble departure frequency. However the volume over time for continuous bubble nucleation remained constant. Thus heat transfer in boiling may be held constant or reduced by the application of an electric field. This result may be surprising given the considerable research reported in the literature on field enhanced boiling. It demonstrates that the electric field geometry has significant effect on the behaviour of bubbles. This is of importance with respect to the design of HTS power apparatus if nucleation is permitted.

An area worthy of future investigation is to identify the source of inter-dependence within the data obtained for bubble detachment period. Several possibilities have been proposed, including; fluid currents, Rayleigh-Taylor instability and field modification due to multiple bubbles between the electrodes. The modelling of the boiling process in any liquid is complex and is further complicated by EHD effects. A more complete model of the dynamics of single bubbles thermally nucleated within electric fields could be attempted in future. This would need to address the dynamic nature of the growth from a thermal source in addition to the effects of conductivity and permittivity gradients resulting from thermal gradients within the liquid.

7.3 Conclusions from a study of streamer behaviour in LN_2

Significant research effort has been dedicated to developing the understanding of the streamer propagation within liquids. Despite this there exists little published work to characterise pd in composite LN_2 and solid dielectric systems. A comprehensive experimental investigation of streamer propagation and pd characterisation has been completed. To achieve this, a technique to measure the electrical pd signal and simultaneously record images of the streamer events has been designed. Samples of point-plane electrode geometry with a composite of LN_2 and a solid dielectric barrier on the face of the plane electrode have been studied. Three solid barriers have been used; a glass reinforced resin, cotton reinforced resin and PTFE sheet. The electrical discharge signal accompanies a charge injection into the liquid causing the vaporisation of channels in the liquid known as density change streamers. pd characterisation demonstrates that general trends exist, common to all the solid barriers used. Thus the influence of the choice of solid dielectric on pd results is concluded to be unappreciable.

Streamer behaviour is typically discussed in terms of initiation and propagation modes. A review of the literature has found that the negative needle tip initiation in LN_2 is known to occur when multiple discharges into the liquid near the tip cause a bubble formation. Propagation occurs as discharges into the bubble vapour causes growth of the streamer channel and dense branching of the streamer channels results in the formation of a bush-like structure.

Filamentary streamers which are typically associated with a positive tip discharge have the appearance of well defined channels directed toward the plane electrode with less dense branching. Both of the typical shapes, bush-like and filamentary, have been observed and recorded for both polarities of needle electrode. Peculiar too LN_2 and LHe, filamentary streamers from a negative tip have been reported and this result has been confirmed in the experiments undertaken.

The positive tip initiated streamer is less well understood and remains a topic for further investigation. Both the more typical filamentary streamer and bush-like streamers have been observed to propagate from a positive point. Filamentary streamers have also been observed to propagate from out of smaller bush-like streamer growth.

Using the different lens arrangements and frame rates it has been possible to capture light emission before vaporisation resulting in a vapour channel for both polarities of discharge. This supports the concept that filamentary growth is by means of ionisation in the liquid phase. A result further supported by the lack of influence of hydrostatic pressure on the pd magnitudes of the mostly filamentary streamers of the recorded positive tip pd results.

In contrast to the positive tip discharge the negative tip discharge magnitudes are clearly shown to be influenced by hydrostatic pressure. The propagation mode for bush-like streamers is therefore demonstrated to be different. It has been conceptualised as a step-wise process of charge injection at the streamer head causing vaporisation. Conduction through the vapour and further injection into the liquid at the streamer head propagates the streamer into the liquid. The different propagation modes have been reported elsewhere to have propagation velocities different by an order of magnitude.

The recorded image sequences of the negative tip streamers, positive half-cycle, are characterised as a sequence of multiple bush-like streamers occurring in rapid succession during the half-cycle. The electrical pd record confirms that the negative tip discharges are more frequent and shows they have a lower average magnitude than for the positive tip streamers. The negative tip, positive half-cycle, pd activity

for voltages near the discharge inception voltage are centred at approximately 100° phase and the positive tip at approximately 280° phase.

Investigations of the influence of increasing the applied voltage showed that, regardless of the pressure, increasing the voltage widens the phase range of pd activity and advances the phase position of the active band. The numbers of discharges also increase as does the average magnitude of discharges for the negative streamer.

It has been clearly shown that hydrostatic pressure and temperature have an effect on streamer behaviour initiated from a negative tip. Increasing pressure or decreasing temperature has the effect of reducing the number of discharges and the active pd phase band, also retarding the phase of pd activity. It is suggested that these effects are due to a reduction in the mean free path of electrons in the liquid as the density increases.

7.4 Further work

A survey of the literature found that the presence of bubbles is critical to the electrical withstand level of liquid nitrogen when applied as a dielectric. The work of Hara and colleagues and more recently Hong has found that thermally generated vapour can be retained between electrodes by EHD forces. However a systematic study for different electrode geometries, and a range of hydrostatic pressure and temperatures has not to date been completed. In addition development of a model for the dynamics of the thermally nucleated bubble remains to be attempted. An extension of this work would be to characterise boiling from surfaces under pool boiling and forced convection boiling regimes in electric fields. Data for both regimes will be important for the use of LN_2 in power apparatus design.

A precise explanation for the conditions leading to the initiation of the positive tip streamer remains to be solved. Experimental studies of the influence of electrode spacing, tip radius, applied voltage, hydrostatic pressure and temperature on pd and images steamer data would be a prudent course of investigation.

Modelling of the propagation and stalling distance of streamers includes the influence of reduced conduction along the length of the streamer and the reduced stress at the streamer head due to branching. High resolution and high frame rate imaging of the shape of the streamer head during propagation and when stopping would allow the modelling of the electric field at the streamer head. This information would provide clarification of the relative significance of electric potential along the streamer length or electric stress at the streamer head as the driver of propagation and streamer stalling distance.

There remains difficulty modelling charge movement within LN_2. Developing understanding of phenomena such as the bubble EHD effects, conduction and charge injection by quantum mechanical tunneling is difficult without a fuller knowledge of the electronic processes at work within the liquid state. At the present time there exists debate over the nature of the electron traps in LN_2. Two concepts have been proposed, the first is electron attachment to molecule clusters to form temporary anions; the second is the formation of electron bubbles. The measurement of an effective work function and relatively low mobility for LN_2 has shown that there is no conduction band which extends in space. This undermines ideas developed from theories applicable to solids. Clarification of the charge transport mechanisms for both low and high field conduction would assist the theoretical development for conditions leading to streamer initiation in LN_2.

The erosion of the solid dielectric barriers during the experiments of this study was not the focus of this work. However such erosion is of interest to the application of solid dielectrics within LN_2-solid composite insulation systems as employed in power apparatus. Characterisation of erosion by streamer strike would be of interest. This could be achieved for a point-plane samples such as has been used to investigate pd behaviour in this study. An extension of this work would be to characterise the behaviour of surface discharge for solid dielectrics in LN_2. This would be possible using the pd measurement and imaging techniques of this study with two needles opposite each other and touching onto the surface of a solid dielectric in LN_2.

Appendix A

Cryostat design calculations

A.1 Top plate

The top plate is manufactured from plasma cut blanks in Stainless Steel 316L supplied by AALCO Metals. The design of the flat top plate follows PD5500:2000 Appendix R.

(a) Design:

D = ave. diameter = 303 mm

e_{cyl} = cylinder thickness = 3 mm

p = design pressure = 2.2 N mm^{-2}

f = design stress = 150 N mm^{-2} (same as category 1 and 2 for flat ends)

$$e_{cylo} = \frac{p \times D}{2 \times f} = \frac{2.2 \times 303}{2 \times 150} = 2.22$$

p/f = 0.014666

and:

(1) Using figure 3.5.5(3) to evaluate C

e_{cyl}/e_{cylo}=1.35

C = 0.64

$e = 0.64 \times 303 \times \sqrt{0.014666} = 23.48\text{mm}$

(2) assuming C = 0.41 (permissible providing $e/e_{cyl} \leq 2.0$)

e = 15.0 mm

e/e_{cyl} = 5 mm therefore case (2) is not permissible

(b) Stress Calculation:

take the design from drawing ITEM 13/14:

D = 303 mm

e_{cyl} = 3 mm

e = 33 mm

p = 2.2 N mm^{-2}

then:

$a = e/e_{cyl} = 33/3 = 11$

$b = D/e_{cyl} = 101$

$$I = \frac{1}{2} + \left(\frac{5904.5}{2689}\right) = 2.7$$ see PD5500 Appendix R

Therefore Stress S in tube is:

$$S = \frac{I \times p \times D}{2 \times e_{cyl}} = \frac{2.7 \times 2.2 \times 303}{2 \times 3} = 299.5\text{N mm}^{-2}$$

Thus S is only 2f, confirming that the stress in the cylinder is not controlling.

However this is only an estimate and is complicated by the fact that the top plate has to have a central opening to permit the HV bushing. The plate thickness required to withstand the stress on the plate i.e. 22 mm is therefore increased to account for the hole. This is done using the material replacement method PD5500:2000 Appendix F.

"Flat ends that have an opening of D/2 or less shall be provided with a total area of reinforcement equal to half that determined in accordance with Appendix F." section 3.5.5.2.1

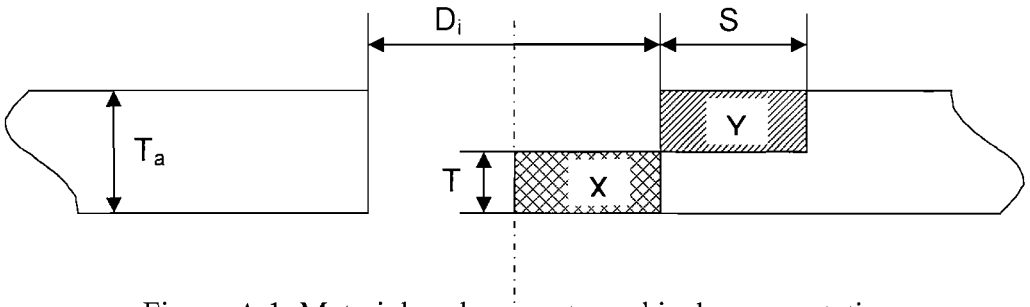

Figure A.1, Material replacement graphical representation

D_i = 120mm

T = 23.48mm

T_a = 33mm

Therefore;

Area X = 60 mm × 23.48 mm = 1409 mm^2

S is the greater of the two values (T_a + 75) mm and $D_i/2$

Therefore S = (T_a + 75) mm = 108 mm, the top plate total diameter is 400 mm

and Area Y = 108 mm × 10.98 mm = 1186 mm^2 > 1409/2 = 704.5 mm^2

The removed area is therefore sufficiently well compensated for.

A.2 Bottom plate

Stress calculations are identical to those of the top plate, except the final stress value in the tube end is higher due to a plate thickness of 30 mm. The stress value is calculated to be 319 Nmm^{-2}.

The material replacement method is less critical for the bottom pate as the hole in the centre of the plate is to be replaced with an OFHC copper block. Although this block is to provide a thermal feed-through from the LN_2 to the cryo-cooler coldhead it also provides additional strength to the end plate.

The material replacement method demonstrates that the thickness of the stainless steel alone would not be sufficient alone, as follows;

$D_i = 115$ mm

$T = 23.48$ mm

$T_a = 30$ mm

Therefore;

Area X = 57.5 mm × 23.48 mm = 1350 mm^2

S is the greater of the two values $(T_a + 75)$ mm and $D_i/2$

Therefore S = $(T_a + 75)$ mm = 105 mm, the top plate total diameter is 300 mm and so S is limited to 92.5 mm.

Area Y = 92.5 mm × 6.52 mm = mm^2 603.1 < 1350/2 = 675 mm^2

This analysis shows that the steel is close to the desired values for the material replacement method. However the OFHC copper block that replaces the steel removed from the hole is machined to a tight sliding fit into the steel plate. Thus the copper will transmit and bear loads applied by the steel; this compensates for the hole in the steel end plate. If the analysis for a complete plate is carried out for the lowest standard design stress value f = 120 mm, the thickness is less than the 30 mm used.

Design:

D = ave. diameter = 303 mm

e_{cyl} = cylinder thickness = 3 mm

p = design pressure = 2.2 Nmm^{-2}

f = design stress = 120 N mm^{-2} (same as category 1 and 2 for flat ends)

$$e_{cylo} = \frac{p \times D}{2 \times f} = \frac{2.2 \times 303}{2 \times 120} = 2.7775$$

p/f = 0.0183333

and:

(1) Using figure 3.5.5(3) to evaluate C

$e_{cyl}/e_{cylo}=1.08$

$C = 0.72$

$e = 0.72 \times 303 \times \sqrt{0.018333} = 29.54\text{mm}$

A.3 Top plate bolt torque calculations

Thirty-two M12s are used to hold the top plate to the top flanges and form the pressure vessel. These have to be sufficient to withstand the force applied to the top plate in service and maintain the pressure seal. They therefore have to be correctly tightened to a calculated torque related to the bolt pre-tensioning. The torque applied to the thirty-two M12 bolts is calculated using a German bolt manufacturer, Bossard, guidelines to the VDI2230 standard as follows [152];

First decide parameters;

1. Lubrication : No Lubrication
2. Friction $\mu = 0.23 - 0.5$: $\mu = 0.3$
3. Bolt Size and Class : M12-70mm Stainless Steel A4-80

From the VDI2230 torque chart (reproduced in the Bossard guide);
with 90% utilisation of the Bolt Yield Value $R_{p\,0.2}$;

Maximum Preload, $F_v = 25.6$ kN
Maximum Tightening Torque, $M_A = 117$ Nm

4. Scatter ± 23% for a manual torque wrench,

"any tightening method has involves certain inaccuracies which are the result of;

- Estimating the friction coefficient
- Manipulation errors of torque wrench (operator errors)
- Tolerance of torque wrench itself." [152]

$\frac{117}{1.23} = 95.12$ Nm Therefore torque to be set on wrench = 95 Nm

5. Check Preload

Mean torque = 95 Nm
Minimum torque applied = $0.77 \times 95 = 73.15$ Nm

$$\text{Minimum preload} = \frac{25.6}{117} \times 73.24 = 16026 \text{ N}$$

Force applied to top plate for 30 bar (3 MPa) pressure test is calculated;

$$A = \pi r^2 = \pi \times (0.15)^2 = 0.0707 m^2$$

$$\text{Force} = p \times A = 3000000 \times 0.0707 = 212058 \text{ N}$$

$$\text{Preload} \times 32 \text{ bolts} = 512832 \text{ N}$$

$$\text{therefore, Safety factor} = \frac{512832}{212058} = 2.4$$

References

1. The Nobel Foundation http://nobelprize.org/physics/laureates/1913/index.html. p. accessed 15 November 2004, last updated 16 June 2000.

2. Sykulski, J.K., Beduz, C., Stoll, R.L., Harris, M.R., Goddard, K. and Yang, Y., Prospects for large high-temperature superconducting power transformers: conclusions from a design study. IEE Proceedings on Electrical Power Applications, 1999. 146(1): p. 41-52.

3. Al-Mosawi, M.K., Beduz, C., Goddard, K.F., Sykulski, J.K., Yang, Y., Xu, B., Ship, K.S., Stoll, R. and Stephen, N.G., Design of a 100 kVA high temperature superconducting demonstration synchronous generator. Physica C, 2002. 372-6(P3): p. 1539-1542.

4. Sykulski, J.K., Goddard, K. and Stoll, R.L., High temperature superconducting demonstrator transformer: design considerations and first test results. IEEE Transactions on Magnetics, 1999. 35(5): p. 3559-61.

5. Lindmayer, M. and Schubert, M., Resistive fault current limiters with HTSC-measurements and simulation. IEEE Transactions on Applied Superconductivity, 1993. 3(1, pt.2): p. 884-8.

6. Norris, W.T. and Power, A., Fault current limiters using superconductors. cryogenics, 1997. 37(10): p. 657-65.

7. Spreafico, S., Bechis, M., Caracino, P., Cavalleri, G., Coletta, G., Carsaro, P., Ladie, P., Nassi, M. and Kelly, N., Status of warm dielectric cable installation at Detroit Edison. Physica C, 2002. 372-376(pt 3): p. 1588-1590.

8. Willen, D., Hansen, F., Daumling, M., Rasmussen, C.N., Ostergaard, J., Traeholt, C., Veje, E., Tonnesen, O., Jensen, K.-H., Olsen, S.K., Rasmussen, C., Hansen, E., Schuppach, O., Visler, T., Kvorning, S., Schuzster, J., Mortensen, J., Christiansen, J. and Mikkelsen, S.D., First operation experiences from a 30 kV, 104 MVA HTS power cable installed in a utility substation. Physica C, 2002. 372-376(pt 3): p. 1571-1579.

9. Masuda, T., Kato, T., Yamura, H., Watanabe, M., Ashibe, Y., Ohkura, K., Suzawa, C., Hirose, M., Isojima, S., Matsuo, K., Honjo, S., Mimura, T., Kuramochi, T., Takahashi, Y., Suzuki, H. and Okamoto, T., Verification tests of a 66 kV HTSC cable system for practical use (first cooling tests). Physica C, 2002. 378-381(pt2): p. 1174-1180.

10. Gouge, M.J., Demko, J.A., Fisher, P.W., Foster, C.A., Lue, J.W., Stovall, J.P., Sinha, U., Armstrong, J., Hughey, R.L., Lindsay, D. and Tolbert, J., Development and testing of HTS cables and terminations at ORNL. IEEE Transactions on Applied Superconductivity, 2001. 11(n1 pt2): p. 2351-2354.

11. Ashworth, S.P., Metra, P. and Slaughter, R.J., A techno-economic design study of high-temperature superconducting power transmission cables. European Transactions on Electrical Power Engineering, 1994. 4(4): p. 293-300.

12. Lock, G.S.H., Latent heat transfer, an introduction to fundamentals. 1994: Oxford.

13. Klimenko, V.V. and Sudarchikov, A.M., Investigation of forced flow boiling of nitrogen in a long vertical tube. Cryogenics, 1983. 23(7): p. 379-385.

14. Denat, A., Jomni, F., Aitken, F. and Bonifaci, N. Generation of bubbles in liquid argon and nitrogen in divergent electric fields. in IEEE 13th International Conference on Dielectric Liquids (ICDL'99). 1999. Nara, Japan: IEEE.p. 384-7.

15. Hara, M., Koishihara, H. and Saita, K., Breakdown behaviour of cryogenic liquids in the presence of thermal bubbles under ramped voltage. IEEE Transactions on Electrical Insulation, 1991. 26(4): p. 685-91.

16. Marto, P.J., Moulson, J.A. and Maynard, M.D., Nucleate boiling of nitrogen with different surface conditions. Transactions of the ASME. -series C Journal of Heat Transfer, 1968. 90(4): p. 437-444.

17. Nishio, S., Study of the minimum heat flux for boiling heat transfer on horizontal flat plates (effects of transcients and thermal conductance of surface). Heat transfer - Japanese Research, 1986. 15(1): p. 15-33.

18. Duluc, M.C., Francois, M.X. and Brunet, J.P., Liquid nitrogen boiling around a temperature controlled heated wire. International Journal of Heat and Mass Transfer, 1996. 39(8): p. 1758-62.

19. Sakurai, A., Shiotsu, M. and Hata, K., Boiling phenomenon due to quasi-steadily and rapidly increasing heat inputs in LN_2 and LHe I. Cryogenics, 1996. 36(3): p. 189-196.

20. Xiulin, Y., Hongji, X., Yuweng, Z. and Hongzhang, Q., Pool boiling heat transfer to liquid nitrogen from porous metallic coatings of tube bundles and experimental research of hysteresis phenomenon. Cryogenics, 1989. 29(4): p. 460-462.

21. Sakurai, A., Shiotsu, M. and Hata, K., A general correlation for pool boiling heat transfer from a horizontal cylinder to subcooled liquid. experimental data for various liquids and its correlation. Transactions of the ASME. Journal of Heat Transfer, 1990. 112(2): p. 441-50.

22. Abashichev, E.N., Dreitzer, G.A., Panevin, V.I. and Firsov, V.P., Influence of subccoling on heat transfer in pool boiling of liquid nitrogen. Heat Transfer Research, 1996. 27(1): p. 239-41.

23. Pasek, A.D., Pool boiling on porous surfaces in cryogenic and refridgerant liquids. PhD. Institute of Cryogenics, University of Southampton. 1992.

24. Levterov, A.I., Semena, M.G., Zaripov, V.K. and Gershuni, A.N., Nucleate boiling on porous surface. Thermal Engineering, 1983. 30(3): p. 62-64.

25. Brentari, E.G. and Smith, R.V. Nucleate and film pool boiling design correlations for O_2, N_2, H_2 and He. in 1964 Cryogenic Engineering Conference. 1965. University of Pennsylvania, Philadelphia.p. 325-341.

26. Leighton, T.G., The Acoustic Bubble. 1997: Academic Press.

27. Zemansky, M.W. and Dittman, R.H., Heat and thermodynamics an intermediate textbook. 7th ed. 1997, New York: McGraw-Hill.

28. Kandlikar, S.G., A theoretical model to predict pool boiling CHF incorporating effect of contact angle and orientation. Transactions of the ASME. Journal of Heat Transfer, 2001. 123(6): p. 1071-9.

29. Bald, W.B., Cryogenic heat transfer research at Oxford : Part 1 -- nucleate pool boiling. Cryogenics, 1973. 13(8): p. 457-469.

30. Tong, W., Bar-Cohen, A., Simon, T.W. and You, S.M., Contact angle effects on boiling incipience of highly-wetting liquids. International Journal of Heat and Mass Transfer, 1990. 33(1): p. 91-103.

31. Schafer, R., Merten, C. and Eingenberger, G., Bubble size distributions in a bubble column reactor under industrial conditions. Experimental Thermal and Fluid Science, 2002. 26: p. 595-604.

32. Rayleigh, L., On the pressure developed in a liquid during the collapse of a spherical cavity. Phil Mag, 1917. 34: p. 94-8.

33. Blake, F.G., Technical Memo 12, Acoustics Research Lab. 1949, Harvard University: Massachusetts, USA.

34. Plesset, M.S. and Prosperetti, A., Bubble dynamics and cavitation. Annual Review Fluid Mechanics, 1977. 9: p. 145-85.

35. Golubnitchii, P.I., Dyaduishkin, P.I., Kalugnii, G.C., Korchikov, S.D. and Kudlenko, V.G., Laser cavitation in liquid nitrogen. PMTF, 1979. 5: p. 103-106.

36. Sato, H., Sun, X.W., Odagawa, M., Maeno, K. and Honma, H., An investigation on the laser induced bubble in cryogenic liquid nitrogen. Transactions of the ASME, 1996. 118: p. 850-856.

37. Tomita, Y., Tsubota, M., Nagane, K. and An-naka, N., Behavior of laser-induced cavitation bubbles in liquid nitrogen. Journal of Applied Physics, 2000. 88(10): p. 5993-6001.

38. Tomita, Y., Tsubota, M. and An-naka, N., Energy evaluation of cavitation bubble generation and shock wave emission by laser focusing in liquid nitrogen. Journal of Applied Physics, 2003. 93(5): p. 3039-48.

39. Gerhold, J., Dielectric breakdown of cryogenic gases and liquids. Cryogenics, 1979: p. 571-584.

40. Gerhold, J., Properties of cryogenic insulants. Cryogenics, 1998. 38(11): p. 1063-81.

41. Gerhold, J., Cryogenic Liquids - A Prospective Insulation Basis for Future Power Equipment. IEEE Transactions on Dielectrics and Electrical Insulation, 2002. 9(1): p. 68-75.

42. Kuffel, E., Zaengl, W.S. and Kuffel, J., High voltage engineering: fundamentals. 2nd ed. 1984: Newnes. 532.

43. Gerhold, J., Potential of cryogenic liquids for power equipment insulation in the medium high voltage range. IEEE Transactions on Dielectrics and Electrical Insulation, 2002. 9(6): p. 878-90.

44. Goshima, H., Hayakawa, N., Hikita, M., Okubo, H. and Uchida, K., Wiebull statistical analysis of area and volume effects on the breakdown strength of liquid nitrogen. IEEE Transactions on Dielectrics and Electrical Insulation, 1995. 2(3): p. 385-393.

45. Hayakawa, N., Sakakibara, H., Goshima, H., Hikita, M. and Okubo, H., Breakdown mechanism of liquid nitrogen viewed from area and volume effects. IEEE Transactions on Dielectrics and Electrical Insulation, 1997. 4(1): p. 127-134.

46. Kawashima, A., Electrode area effect on the electrode breakdown of liquid nitrogen. Cryogenics, 1974: p. 217-219.

47. Naphthenics, Nynas Transformer Oil Data Sheet - Nytro 10GBN. 2004.

48. Hanaoka, R., Ishibashi, R., Kasama, M., Uchiyama, A. and Kawaguchi, A., Pre-breakdown current in liquid nitrogen under dc nonuniform field. Nuclear Instruments and Methods in Physics Research, 1993. A327: p. 107-110.

49. Peier, D., Breakdown of LN_2 by field induced microbubbles. Journal of Electrostatics, 1979. 7: p. 113-122.

50. Frayssines, P.E., Bonifaci, N., Denat, A. and Lesaint, O., Streamers in liquid nitrogen: characterization and spectroscopic determination of gaseous filament temperature and electron density. Journal of Physics D (Applied Physics), 2002. 35(4): p. 369-377.

51. Frayssines, P.E., Lesaint, O., Bonifaci, N., Denat, A. and Devaux, F. Prebreakdown and breakdown phenomena under uniform field in liquid nitrogen. in IEEE 14th International Conference on Dielectric Liquids (ICDL). 2002.p. 139-142.

52. Frayssines, P.E., Lesaint, O., Bonifaci, N., Denat, A., Lelaidier, S. and Devaux, F., Prebreakdown phenomena at high voltage in liquid nitrogen and comparison with mineral oil. IEEE Transactions on Dielectrics and Electrical Insulation, 2002. 9(6): p. 899-909.

53. Denat, A., Jomni, F., Aitken, F. and Bonifaci, N., Thermally and electrically induced bubbles in liquid argon and nitrgoen. IEEE Transactions on Dielectrics and Electrical Insulation, 2002. 9(1): p. 17-22.

54. Yamazawa, K. and Yamashita, H., Prebreakdown Density Change Streamer in Liquid Nitrogen. Japanese Journal of Applied Physics, 1997. 36 part 1(10): p. 6437-6443.

55. Yamazawa, K. and Yamashita, H., Pre-breakdown Light Emission and Current Pulses in Liquid Nitrogen. Japanese Journal of Applied Physics, 1998. 37 part 1(1): p. 171-178.

56. Takahasi, Y. and Ohtsuka, K., Corona discharges and bubbling in liquid nitrogen. Journal of Physics D (Applied Physics), 1974. 8: p. 165-169.

57. Kim, S., Jeong, J., Kim, Y., Kim, C. and Baek, S., Influence of bubble size and flow velocity on AC electrical breakdown characteristics on LN_2. Cryogenics, 2002. 42: p. 411-414.

58. Hara, M., Kaneko, T. and Honda, K. Thermal-bubble initiated breakdown characteristics of liquid helium and nitrogen at atmospheric pressure. in IEEE 9th International Conference on Conduction and Breakdown in Dielectric Liquids (ICDL). 1987.p. 466-470.

59. Hara, M. and Kubuki, M., Effect of thermally induced bubbles on the electrical breakdown characteristics of liquid nitrogen. IEE Proceedings, 1990. 137(Part A, No.4): p. 209-216.

60. Hara, M., Wang, Z. and Saito, H. Thermal bubble breakdown in cryogenic liquids under non-uniform fields. in IEEE 11th International Conference on Conduction and Breakdown in Dielectric Liquids (ICDL). 1993. Baden-Dattwil, Switz: IEEE.p. 249-253.

61. Hara, M., Wang, Z. and Saito, H., Thermal Bubble Breakdown in Liquid Nitrogen under Non-uniform Fields. IEEE Transactions on Dielectrics and Electrical Insulation, 1994. 1(4): p. 709-715.

62. Takano, K., Matsuura, S., Yan, J., Suehiro, J. and Hara, M., Effect of a Thin Insulation Film on Thermal Bubble-Triggered Breakdown Phenomena in Liquid Nitrogen. Electrical Engineering in Japan, 1999. 127(4): p. 18-26.

63. Seok, B.Y., Komatsu, M., Kushinaga, M., Suehiro, J. and Hara, M., Pressurizing and Sub-cooling Effects on Electrical Breakdown of LN_2 in Modeled HTS Coils. IEEE Transactions on Dielectrics and Electrical Insulation, 2001. 8(6): p. 1016-24.

64. Seok, B.Y., Tamuro, N. and Hara, M., A study of thermal bubble behaviour in the simulated electrode system of high temperature superconducting coils. IEEE Transactions on Dielectrics and Electrical Insulation, 1999. 6(3): p. 109-116.

65. Ladie, P., Caracino, P. and Nassi, M. Patent: Superconducting Cable, Appl.No. EP1195777A1. Patent No. 6th October. 2000

66. Von Dollen, D., Metra, P. and Rahman, M. Design concept of a room temperature dielectric HTS cable. in American Power Conference. 1993. Chicago.p. 1206-1211.

67. Ashibe, Y., Hirose, M., Furukawa, K., Takahashi, Y., Matsuo, K., Honjo, S., Mimura, T. and Aiba, T. Patent: Terminal structure of extreme-low temperature equipment, Appl.No. EP1283576A1. Patent No. 13th February. 2002

68. Nassi, M. and Ladie, P. Patent: Superconducting cable, Appl.No. PCT/EP99/10446. Patent No. WO 00/39813. 6th July. 1999

69. Nassi, M. and Ladie, P. Patent: Electrical power transmission system using superconductors, Appl.No. 09/886,043. Patent No. US 2002/0019315 A1. 14th February. 2002

70. Klimkin, V.F. High speed optical and statistical investigations of pre-breakdown in liquid dielectrics in the nano-second region. in 13th IEEE International Conference on Conduction and Breakdown in Dielectric Liquids (ICDL). 1999. Nara, Japan: IEEE.p. 152-155.

71. Span, R., Lemmon, E.W., Jacobsen, R.T., Wagner, W. and Yokozeki, A., A reference equation of state for the thermodynamics of nitrogen for temperatures from 63.151 to 1000 K and pressures to 2200 MPa. Journal of Physical and Chemical Reference Data, 2000. 29(6): p. 1361-1433.

72. Cigre and Study Committee SC21 - HV Insulated Cables, High Temperature Superconducting (HTS) cable systems, in Cigre Technical Brochure. 2003.

73. Lim, C.C., Indium seals for low-temperature and moderate-pressure applications. Review of Scientific Instruments, 1985. 57(1): p. 108-114.

74. Hathaway, G.M., High Temperature Superconducting Power Cable Termination. PhD. Electrical Engineering, University of Southampton. 1999.

75. Allen, P.H.G. and Karayiannis, T.G., Electrohydrodynamic enhancement of heat transfer and fluid flow. Heat Recovery Systems and CHP, 1995. 15(5): p. 389-423.

76. Watson, P.K., Influence of an electric filed upon the heat transfer from a hot wire to an insulating liquid. Nature, 1961. 189: p. 563-564.

77. Ogata, J. and Yabe, A., Basic study on the enhancement of nucleate boiling heat transfer by applying electric fields. International Journal of Heat and Mass Transfer, 1993. 36(3): p. 775-82.

78. Ogata, J. and Yabe, A., Augmentation of boiling heat transfer by utilizing the EHD effect--EHD behaviour of boiling bubbles and heat transfer characteristics. International Journal of Heat and Mass Transfer, 1993. 36(3): p. 783-791.

79. Markels, M. and Durfee, R.L., The effect of applied voltage on boiling heat transfer. American Institute of Chemical Engineers Journal, 1964. 10(1): p. 106-110.

80. Jones, T.B. and Hallock, K.R., Surface wave model of electrohydrodynamically coupled minimum film boiling. Journal of electrostatics, 1978. 5: p. 273-284.

81. Jones, T.B. and Schaeffer, R.C., Electrohydrodynamically coupled minimum film boiling in dielectric liquids. AIAA Journal, 1976. 14(2): p. 1759-65.

82. Zaghdoudi, M.C. and Lallemand, M., Electric field effects on pool boiling. Journal of Enhanced Heat Transfer, 2002. 9(5-6): p. 187-208.

83. Rutkowski, J., The influence of electric field on heat transfer in boiling cryogenic liquid. cryogenics, 1977. 17: p. 242-243.

84. Savin, I.K., Bologa, M.K. and Korovkin, V.P., Effect of an electric field on the rate of heat and mass exchange during evaporation. Soviet Surface Engineering and Applied Electrochemistry (English translation of Electronnaya Obrabotka Materialov), 1986. 6: p. 70-73.

85. Stratton, J.A., Electromagnetic Therory. International series in physics, ed. DuBridge, L.A. 1941, New York and London: McGraw-Hill.

86. Pohl, H.A., Some effects of nonuniform fields on dielectrics. Journal of Applied Physics, 1958. 29(8): p. 1182-1188.

87. Ogata, J., Iwafuji, Y., Shimada, Y. and Yamazaki, T., Boiling heat transfer enhancement in tube-bundle evaporators utilizing electric field effects. ASHRAE Transactions, 1992. 98(2): p. 435-444.

88. Zaghdoudi, M.C., Cioulachtjian, S. and Lallemand, M. EHD enhancement of pool boiling of pentane on a horizontal copper surface. in International

symposium on two-phase flow modelling and experimentation. 1995. Rome, Italy.p. 1075-1082.

89. Kweon, Y.C., Kim, M.H., Cho, H.J. and Kang, I.S., Study of the deformation and departure of a bubble attached to a wall in dc/ac electric fields. International Journal of Multiphase Flow, 1998. 24(1): p. 145-162.

90. Zuber, N., Hydrodynamic aspects of boiling heat transfer, in Atomic Energy Commision Report, number AECU-4439. 1959.

91. Cheng, K.J. and Chaddock, J.B., Maximum size of bubbles during nucleate boiling in an electric field. International Journal of Heat and Fluid Flow, 1986. 7(4): p. 278-282.

92. Cho, H.J., Kang, I.S., Kweon, Y.C. and Kim, M.H., Study of the behaviour of a bubble attached to a wall in a uniform electric field. International Journal of Multiphase Flow, 1996. 22(5): p. 909-922.

93. Kweon, Y.C. and Kim, M.H., Experimental study in the nucleate boiling enhancement and bubble dynamic behavior in saturated pool boiling using a non-uniform dc electric field. International Journal of Multiphase Flow, 2000. 26: p. 1351-1368.

94. Zaghdoudi, M.C. and Lallemand, M., Nucleate pool boiling under dc electric field. Experimental heat transfer, 2001. 14: p. 157-180.

95. Zaghdoudi, M.C. and Lallemand, M., Analysis of the polarity influence on nucleate pool boiling under a dc electric field. Transactions of the ASME: Journal of Heat Transfer, 1999. 121: p. 856-864.

96. Byatt, S.W. and Secker, P.E., Electrical conduction in liquid air and liquid nitrogen. British Journal of Applied Physics (J. Phys. D), 1968. Ser. 2 v.1: p. 1011-17.

97. Malenkov, I.G., The frequency of vapour bubble seperation as a function of bubble size. Fluid Mechanics Soviet Research, 1972. 1: p. 36-42.

98. Kutateladze, J.J. and Grogonin, I.I., Growth velocity and bubble departure diameter of vapour bubbles in saturated liquids in free convective flow. Teplofiz. Vys. Temp, 1979. 17: p. 792-797.

99. Sarnobat, S.U., Rajput, S., Bruns, D.D., DePaoli, D.W., Daw, C.S. and Nguyen, K., The impact of external electrostatic fields on gas-liquid bubbling dynamics. Chemical Engineering Science, 2004. 59: p. 247-258.

100. Hong, T.P., Frayssines, P.E., Lesaint, O., Aitken, F. and Devaux, F. Influence of vapor bubbles initiated by steady heating on the breakdown of liquid nitrogen. in 2003 Annual Report: Conference on Electrical Insulation and Dieletric Phenomena, Oct 19-22 2003. 2003. Albuquerque, NM, United States: Institute of Electrical and Electronics Engineers Inc.p. 313-316.

101. Denat, A. High field conduction and pre-breakdown phenomena in dielectric liquids. in International Conference on Dielectric Liquids, ICDL2005. 2005. Coimbra, Portugal.p. 57-62.

102. Beroual, A., Zahn, M., Badent, A., Kist, K., Schwabe, A.J., Yamashita, H., Yamazawa, K., Danikas, M., Chadband, W.D. and Torshin, Y., Propagation and structure of streamers in liquid dielectrics. IEEE Electrical Insulation Magazine, 1998. 14(2): p. 6-17.

103. Tobazeon, R., Pre-breakdown phenomena in Dielectric Liquids. IEEE Transactions on Dielectrics and Electrical Insulation, 1994. 1(6): p. 1132-1147.

104. Badent, A., Kist, K., Schwab, A.J., Beroual, A., Chadband, W.G., Danikas, M., Sierota, A.B., Torshin, Y. and Zahn, M. Preliminary report for the IEEE DEIS Liquid Dielectrics Committee international study group on "Streamer Propagation in Liquids". in ICDL '96. 12th International Conference on Conduction and Breakdown in Dielectric Liquids. 1996. Roma, Italy: IEEE.p. 375-8.

105. Kelly, E.F. and Hebner, R.E., The electric field distribution associated with prebreakdown phenomena in nitrobenzene. Journal of Applied Physics, 1981. 52(1): p. 191-195.

106. Kattan, R., Denat, A. and Bonifaci, N., Formation of vapour bubbles in non-polar liquids initiated by current pulses. IEEE Transactions on Electrical Insulation, 1991. 26(4): p. 656-62.

107. Qureshi, M.I., Chadband, W.D. and Watson, P.K. Prebreakdown cavities in viscous silicone fliuds and their relationship to initiating current pulses. in IEEE conference on dielectric materials. 1992.p. 89-93.

108. Aitken, F., McCluskey, F. and Denat, A., An Energy Model for Artificially Generated Bubbles in Liquids. Journal of Fluid Mechanics, 1996. 327: p. 373-392.

109. Watson, P.K., Qureshi, M.I. and Chadband, W.D., The Growth of Prebreakdown Cavities in Silicone Fliuds and the Frequency of the Accompanying Discharge Pulses. IEEE Transactions on Dielectrics and Electrical Insulation, 1998. 5(3): p. 344-350.

110. Halpern, B. and Gomer, R., Field Emission in Liquids. Journal of Chemical Physics, 1969. 51: p. 1031-1047.

111. Dotoku, K., Yamada, H., Sakamoto, S., Noda, S. and Yoshida, H., Field emission into non-polar organic liquids. Journal of Chemical Physics, 1978. 69: p. 1121-1125.

112. Denat, A., Grosse, J.P. and Grosse, B., Electrical conduction in purified cyclohexane in a divergent electric field. IEEE Transactions on Electrical Insulation, 1988. 23(4): p. 545-554.

113. Holroyd, R.A. and Allen, M., Energy of excess electrons in non-polar liquids by photoelectric work function measurements. The journal of chemical physics, 1971. 54(12): p. 5014-21.

114. Tauchert, W., Jungblut, H. and Schmidt, W.F., Photoelectric determination of Vo values and electron ranges in some cryogenic liquids. Canadian Journal of Chemistry, 1977. 55: p. 1860-1866.

115. Sakai, Y., Schmidt, W.F. and Khrapak, A.G., Self-trapping of Electrons in Liquid Nitrogen. IEEE Transactions on Dielectrics and Electrical Insulation, 1994. 1(4): p. 724-727.

116. Gee, N., Floriano, M.A., Wada, T., Huang, S.S.-S. and Freeman, G., Ion and electron mobilities in cryogenic liquids: Argon, Nitrogen, Methane and Ethane. Journal of Applied Physics, 1985. 57: p. 1097-1101.

117. Schmidt, W.F., Electrons in Non-polar Dielectric Liquids. IEEE Transactions on Electrical Insulation, 1991. 26(4): p. 560-567.

118. Wada, T. and Freeman, G., Electron localization in dense nitrogen vapour. Journal of Chemical Physics, 1980. 72(12): p. 6726-30.

119. Lias, S.G., Levin, R.D. and Kafafi, S.A., "Gas phase ion energetics data" in NIST Standard Reference Database Number 69, (http://webbook.nist.gov/chemistry/). Number 69, June 2005 ed, ed. Linstrom, P.J. and Mallard, W.G. June 2005: NIST, National Institute of Standards and Technology.

120. Born, M., Volumen und Hydrastationswarme der Ionnen. Zurnal Physik, 1920. 1: p. 45-48.

121. Schottky, W., The expulsion of electrons from heated wires under retarding potentials. Annalen der Physik, 1914. 44: p. 1011-32.

122. Fowler, R.H. and Nordheim, L., Electron emission in intense electric fields. Proc. Roy. Soc., 1928. A119: p. 173-81.

123. Sommerfield, A., Electrodynamics. 1952: Academic Press.

124. Bonifaci, N., Denat, A. and Atrazhev, V.M., Work functions for a HV cathode in nonpolar liquids. IEEE Transactions on Dielectrics and Electrical Insulation, 1994. 1(4): p. 657-662.

125. Hernandez-Avila, J.L., Bonifaci, N. and Denat, A., Hot electron phenomena in liquid and gaseous Ar and N2 in divergent electric fields. IEEE Transactions on Dielectrics and Electrical Insulation, 1994. 1(3): p. 412-418.

126. Townsend, J.S., Electricity in gases. 1914: Oxford Press.

127. Lewis, T.J., A new model for the primary process of electrical breakdown in liquids. IEEE Transactions on Dielectrics and Electrical Insulation, 1998. 5(3): p. 306-15.

128. Lewis, T.J., Breakdown mechanisms at electrode interfaces in liquids. IEEE Transactions on Dielectrics and Electrical Insulation, 2003. 10(6): p. 948-955.

129. Tobazeon, R. Prebreakdown phenomena in dielectric liquids. in Proceedings of 1993 IEEE 11th International Conference on Conduction and Breakdown in Dielectric Liquids (ICDL '93), 19-23 July 1993. 1993. Baden-Dattwil, Switzerland: IEEE.p. 172-83.

130. Haidara, M. and Denat, A., Electron multiplication in liquid cyclohexane and propane (an estimation of the ionization coefficient). IEEE Transactions on Electrical Insulation, 1991. 26(4): p. 592-597.

131. Dumitrescu, L., Lesaint, O., Bonifaci, N., Denat, A. and Notingher, P., Study of streamer inception in cyclohexane with a sensitive charge measurement technique under impulse voltage. Journal of Electrostatics, 2001. 53(2): p. 135-46.

132. Lesaint, O. and Gournay, P., Initiation and propagation thresholds of positive prebreakdown phenomena in hydrocarbon liquids. IEEE Transactions on Dielectrics and Electrical Insulation, 1994. 1(4): p. 702-8.

133. Forster, E.O., Partial discharges and streamers in liquid dielctrics: the significance of the inception voltage. IEEE Transactions on Electrical Insulation, 1993. 28(6): p. 941-946.

134. Fleszynski, J., Zelek, A. and Skowronski, J.I., Development of discharges in liquid nitrogen in non-uniform electrical field. Journal of Electrostatics, 1979. 7: p. 39-46.

135. Lesaint, O. and Massala, G., Positive streamer propagation in large oil gaps: experimental characterization of propagation modes. IEEE Transactions on Dielectrics and Electrical Insulation, 1998. 5(3): p. 360-70.

136. Lesaint, O. and Gournay, P., On the gaseous nature of positive filamentary streamers in hydrocarbon liquids. I: Influence of the hydrostatic pressure on the propagation. Journal of Physics D: Applied Physics, 1994. 27(10): p. 2111-2116.

137. Devins, J.C., Rzad, S.J. and Schwabe, R.J., Breakdown and prebreakdown phenomena in liquids. Journal of Applied Physics, 1981. 52(7): p. 4531-4545.

138. Barmann, P., Kroll, S. and Sunesson, A., Spatially and temporally resolved electron density measurements in streamers in dielectric liquids. Journal of Applied Physics, 1997. 30: p. 856-863.

139. Swaffield, D.J., Lewin, P.L., Chen, G. and Swingler, S.G., Variable Pressure and Temperature Liquid Nitrogen Cryostat for Optical Measurements with Applied Electric Fields. Journal of Measurement Science and Technology, 2004. 15(11): p. 2325-2332.

140. Mason, J.H., Breakdown of Solid Dielectrics in Divergent Fields. Proceedings of the Institute of Electrical Engineers, 1955. 102 C: p. 254.

141. Coelho, R. and Debeau, J., Properties of the tip-plane configuration. Journal of Physics D (Applied Physics), 1971. 4: p. 1266-1280.

142. Chen, G. and Davies, A.E., Electric stress computation - a needle-plane electrode system with space charge effects. COMPEL - The International Journal for Computation and Mathematics in Electrical and Electronic Engineering, 1996. 15(1): p. 40-56.

143. Hayakawa, N., Maeda, H., Chigusa, S. and Okubo, H., Partial discharge inception characteristics of LN2/expoxy composite insulation system under thermal bubble condition. cryogenics, 2000. 40: p. 167-171.

144. Tsuru, S., Nakamura, M., Mine, T., Suehiro, J. and Hara, M. Partial discharge inception characteristics in artificial air-filled voids at room and liquid nitrogen temperatures. in Conference Record of the 1998 IEEE International Symposium on Electrical Insulation, 7-10 June 1998. 1998. Arlington, VA, USA: IEEE.p. 153-6.

145. Tsuru, S.-i., Nakamura, M., Funaki, K., Iwakuma, M., Suehiro, J. and Hara, M. Partial discharge characteristics in artificial air-filled voids immersed in liquid nitrogen. in Proceedings of the 1997 5th IEEE International Conference on Properties and Applications of Dielectric Materials. Part 1 (of 2), May 25-30 1997. 1997. Seoul, South Korea: IEEE, Piscataway, NJ, USA.p. 228-231.

146. Takahashi, Y. and Ohtsuka, K., Corona discharges and bubbling in liquid nitrogen. Journal of Physics D (Applied Physics), 1974. 8: p. 165-169.

147. Sumereder, C., Muhr, M. and Woschitz, R. Dielectric properties of liquid nitrogen. in 13th International Symposium on High Voltage Engineering. 2003. Delft, Netherlands: Millpress.

148. Suehiro, J., Matsumoto, Y., Imasaka, K. and Hara, M. Partial discharge induced bubbles generated in subcooled liquid nitrogen at atmospheric pressure. in 13th International Symposium on High Voltage Engineering (ISH). 2003. Delft.p. 153.

149. Kosaki, M., Hane, Y., Isaka, S. and Horii, K., Partial discharge in liquid nitrogen. Transactions of the Institute of Electrical Engineers of Japan, 1976. 96(14): p. 317-24.

150. Pompili, M., Mazzetti, C., Libotte, M. and Forster, E.O., The effect of the definition used in measuring partial discharge inception voltages. IEEE Transactions on Electrical Insulation, 1993. 28(6): p. 1002-06.

151. Patrissi, S., Pompili, M., Yamashita, H. and Forster, E.O. Study of the effect of electrical breakdown in dielectric liquids on the needle point structure. in Proceedings of the IEEE 11th International Conference on Conduction and Breakdown in Dielectric Liquids (ICDL), Jul 19-23 93. 1993. Baden-Dattwil, Switz: Publ by IEEE, Piscataway, NJ, USA.p. 376-382.

152. Bossard AG Schrauben; A guide to VDI2230, Bolt strength and torque. 2000, Bossard AG Schrauben.